



저작자표시-비영리-변경금지 2.0 대한민국

이용자는 아래의 조건을 따르는 경우에 한하여 자유롭게

- 이 저작물을 복제, 배포, 전송, 전시, 공연 및 방송할 수 있습니다.

다음과 같은 조건을 따라야 합니다:



저작자표시. 귀하는 원저작자를 표시하여야 합니다.



비영리. 귀하는 이 저작물을 영리 목적으로 이용할 수 없습니다.



변경금지. 귀하는 이 저작물을 개작, 변형 또는 가공할 수 없습니다.

- 귀하는, 이 저작물의 재이용이나 배포의 경우, 이 저작물에 적용된 이용허락조건을 명확하게 나타내어야 합니다.
- 저작권자로부터 별도의 허가를 받으면 이러한 조건들은 적용되지 않습니다.

저작권법에 따른 이용자의 권리는 위의 내용에 의하여 영향을 받지 않습니다.

이것은 [이용허락규약\(Legal Code\)](#)을 이해하기 쉽게 요약한 것입니다.

[Disclaimer](#)

공학박사학위논문

# Spray Characteristics of Particle-laden Type Injector Using Powder Fuel

분말 연료를 이용한 입자 부상 분사기의 분무특성

2016년 2월

서울대학교 대학원

기계항공공학부

윤정수

# Spray Characteristics of Particle-laden Type Injector Using Powder Fuel

분말 연료를 이용한 입자 부상 분사기의 분무특성

지도교수 윤 영 빈

이 논문을 공학박사 학위논문으로 제출함

2015 년 11 월

서울대학교 대학원

기계항공공학부

윤 정 수

윤정수의 공학박사 학위논문을 인준함

2015 년 12 월

위 원 장 : \_\_\_\_\_

부위원장 : \_\_\_\_\_

위 원 : \_\_\_\_\_

위 원 : \_\_\_\_\_

위 원 : \_\_\_\_\_

## ABSTRACT

Spray characteristics of particle-laden injector were experimentally investigated for the particle (aluminum, magnesium) as a fuel. Spray characteristics of gas centered gas-liquid shear coaxial injector were investigated varying injection condition under seawater injected as a liquid phase. Similarity characteristics of particle and carrier gas were investigated in particle-laden jet, and mixing characteristics between particle and coaxial gas also investigated using shear and swirl coaxial injector.

Mass flow rate and direct photograph were used to investigate the spray characteristics such as breakup process of liquid sheet in gas centered gas-liquid shear coaxial injector. Self-pulsation occurs in that injector and it is accompanied by an intensive noise. Self-pulsation generate the pressure and flow rate oscillation in gas and liquid phase. Because of this oscillation can argument combustion instabilities, self-pulsation should be suppressed. Effect of recess and Reynolds number of liquid and gas phase on self-pulsation characteristics were studied by measured frequency of liquid sheet under self-pulsating condition. It was found that the different self-pulsation occurred by the recess number of injector. Self-pulsation occurred by the liquid bubble collapse process under low recess case, however liquid sheet and central gas interaction in nozzle inside dominate the oscillation of liquid sheet.

Small particle of  $1\mu\text{m}$  represent a fluid characteristics and large particle with 42.5 mean diameter used as a fuel were simultaneously injected for investigate effect of particle on a carrier gas and particle characteristics in particle-laden jet. Particle mass loading ratio effects on a velocity and turbulence intensity of carrier gas, and carrier gas and particle can agreed with similarity. Effect of particle mass loading ratio on carrier gas in jet developing region differs from fully developed region. Accordingly, centerline velocity decay of carrier gas were formulated in jet developing region and fully developed region, respectively, and were compared with the previous results. Centerline velocity decay of particle were formulated with particle Reynolds number, because particle drag force determined by the

particle Reynolds number. Previously study, change in turbulence intensity can determined by the ratio of particle diameter and turbulence length scale. The present experimental data suggests that, consideration of the characteristic length scales (particle diameter and turbulence length scale) is insufficient to predict gas-phase turbulence modulation in particle-laden flow, because as slip velocity between gas and particle increases turbulence intensity also increased. Therefore, slip velocity also considered to predict gas-phase turbulence modulation.

In addition, Mie scattering and acetone PLIF technique were used for particle and coaxial gas, respectively, to investigate mixing characteristics between particle and coaxial gas. Mixing efficiency of shear coaxial was higher than swirl coaxial under injector without recess, and mixing efficiency was sensitive to the change of velocity ratio between coaxial and central jet. As for the swirl coaxial injector with recess, mixing efficiency was higher than shear coaxial and less sensitive the change of velocity ratio, so swirl coaxial injector can be used for solid particle propulsion system with large operating range.

**Keywords:** Recess, Spray Characteristics, Mixing characteristics, Particle-laden Jet, PIV/Acetone PLIF, Scailing

**Student Number:** 2011-30204

# LIST

ABSTRACT	i
LIST	iii
LIST OF FIGURES	vi
LIST OF TABLES	x
NOMENCLATURE	xi
CHAPTER 1	
INTRODUCTION .....	1
CHAPTER 2	
EXPERIMENT AND MEASUREMENT SYSTEMS.....	6
2.1 Automated Particle Feeder .....	6
2.2 Two-phase Jet Measurement Technique .....	8
2.2.1 Phase Discrimination Using Image Processing .....	8
2.2.2 Validation of the Image Processing Technique .....	17
2.3 Simultaneous PIV and Acetone PLIF Diagnostics .....	20
2.3.1 Particle Image Velocimetry .....	20
2.3.2 Acetone PLIF .....	24
2.3.3 Simultaneous Measurement System .....	29
CHAPTER 3	
SPRAY CHARACTERISTICS OF GAS/LIQUID SHEAR COAXIAL INJECTOR WITH ANNULAR LIQUID SHEETS .....	32
3.1 Background and Objectives.....	32
3.2 Experimental Apparatus and Methods.....	34
3.3 Self-pulsation Characteristics .....	38
3.3.1 Spray Patterns .....	38
3.3.2 Low Recess Ratio ( $RR \leq 1.67$ ) .....	42

3.3.3 High recess ratio (RR=3.34) .....	46
---	----

## CHAPTER 4

SPRAY CHARACTERISTICS OF CARRIER GAS AND PARTICLES IN PARTICLE-LADEN SIMPLE JETS .....	50
4.1 Background and Objectives.....	50
4.2 Experimental Conditions .....	52
4.3 Fluidic Characteristics of Particle and Carrier Gas .....	56
4.3.1 Mean Velocity Characteristics .....	56
4.3.2 Similarity Characteristics of Particle and Carrier Gas .....	61
4.3.3 Similarity of Particle Number Density .....	66
4.4 Scaling of the Centerline Velocity Decay .....	69
4.4.1 Centerline Velocity Decay of Gas Phase.....	69
4.4.2 Centerline Velocity Decay of Particle .....	74
4.5 Turbulence Modulation .....	77

## CHAPTER 5

SPRAY CHARACTERISTICS OF PARTICLE-LADEN COAXIAL JETS .....	85
5.1 Background and Objectives.....	85
5.2 Experimental Conditions .....	88
5.3 Effect of Particle Loading Ratio on Gas Phase Velocity .....	92
5.4 Particle Distribution Characteristics .....	95
5.5 Mixing Characteristics.....	100
5.5.1 Fuel and Oxidizer Distributions.....	100
5.5.2 Mixing Process .....	103
5.5.3 Mixing Efficiency .....	107
5.5.4 Recess ratio effects on mixing efficiency .....	111

CHAPTER 6	
CONCLUSION.....	115
REFERENCES .....	118
ABSTRACT IN KOREAN.....	124

## LIST OF FIGURES

Fig. 1.1	Schematic of the particle – steam coaxial jet.	2
Fig. 2.1	Automated particle feeder.	7
Fig. 2.2	Particle feeding rate test	8
Fig. 2.3	FFT cross-correlation map.	10
Fig. 2.4	FFT filtering method showing the interrogation spots before and after filtering.	11
Fig. 2.5	The intensity distribution of original, cutoff and remained pixels (mean of 600 images).	12
Fig. 2.6	Particle distribution contour map of the average of all the particle obtained from 300 PIV images taken in single and two-phase particle-laden jet.	15
Fig.2.7	Image filtering and separation sequence a. original image; b. image after fft filtering; c. image after fft filtering and relative intensity filtering; d. image after fft filtering, relative intensity and local max filtering; e. separated small particles; f. separated large particles.	16
Fig. 2.8	Representative images showing the image processing for the tracer only particle images; a. tracer only image; b. particle only image; c. two-phase flow image created by overlapping Fig. 4a and Fig. 4b; d. tracer only image separated by the image processing technique.	18
Fig. 2.9	Instantaneous streamwise velocity component obtained from a the original tracer only images, b the processed tracer only images.	18
Fig. 2.10	Comparison of (a) mean velocity and (b) turbulent intensity profiles obtained from real and processed tracer only images.	19
Fig. 2.11	Typical procedure of PIV.	21
Fig. 2.12	Transmittance of BG 25.	25
Fig. 2.13	Shot by shot normalized laser intensity.	27
Fig. 2.14	Laser sheet profile.	28
Fig. 2.15	An image at four stages of the correction procedure: (a) the original image, (b) after median filtered, (c) after background subtraction and laser energy fluctuation correction, and (d) after	29

	laser sheet profile and absorption corrections.	
Fig. 2.16	Experimental setup for PIV and Acetone PLIF simultaneous measurements.	31
Fig. 3.1	He-Ne laser and photo detector system to measure the frequency of spray oscillation.	34
Fig. 3.2	Result of FFT process.	35
Fig. 3.3	Schematic of geometric parameters.	36
Fig. 3.4	Schematic of a swirl coaxial injector (in millimeters).	37
Fig. 3.5	Spray angle at $Re_L=17,279$ .	38
Fig. 3.6	Spray patterns with the gas Reynolds number at $Re_L=17,279$ and no recess with self-pulsation and no pulsation case: (a) self-pulsation, $Re_g=23,148$ ( $J=0.083$ ); (b) self-pulsation, $Re_g=32,737$ ( $J=0.167$ ); (c) self-pulsation, $Re_g=40,094$ ( $J=0.25$ ); (d) no pulsation, $Re_g=51,762$ ( $J=0.417$ ).	39
Fig. 3.7	Spray patterns with the recess ratio at $Re_L=17,279$ , $Re_g=23,148$ and $J=0.083$ with self-pulsation and no pulsation case: (a) self-pulsation, $RR=0$ ; (b) self-pulsation, $RR=1.67$ ; (c) no pulsation, $RR=3.34$ .	40
Fig. 3.8	Strouhal number comparing with recess ratio.	42
Fig. 3.9	Spray patterns with the gas Reynolds number at $Re_L= 4981$ , $\dot{Q}_L=15.13\text{cm}^3/\text{s}$ and $RR=0$ :	43
Fig. 3.10	Characteristic frequency of self-pulsation.	45
Fig. 3.11	Self-Pulsation Boundary with RR at various momentum flux.	46
Fig. 3.12	Inner injector jet width	47
Fig. 3.13	Internal Collision in the high recess,	47
Fig. 3.14	Characteristic frequency of self-pulsation.	49
Fig. 3.15	Self-Pulsation Boundary with various momentum flux.	49
Fig. 4.1	Experimental apparatus.	52
Fig. 4.2	Cumulative particle diameter. (a) Mean diameter $1\mu\text{m}$ , (b) Mean diameter $42\mu\text{m}$	53
Fig. 4.3	Mean axial velocity distribution of single- and two-phase flows.	57
Fig. 4.4	Axial profiles of mean velocities of single-phase, two-phase, and	58

	solid particles.	
Fig. 4.5	Radial profiles of axial mean velocities effect of exit Reynolds number, effect of particle loading ratio in $Re_0=20400$ (a) $x/D=0.2$ , (b) $x/D=2$ , (c) $x/D=16$	60
Fig. 4.6	Structure of jet.	61
Fig. 4.7	Mean velocity distribution ( $U_0=152.8$ m/s, $L_0=30$ mm).	64
Fig. 4.8	Particle mean velocity profile across the jet ( $L_0=20$ mm, $D=3.5$ mm).	65
Fig. 4.9	Velocity and turbulence intensity distribution at $x/D=10$ .	67
Fig. 4.10	Particle number density profile.	67
Fig. 4.11	Particle number density profile according to orifice length.	68
Fig. 4.12	Gas phase centerline velocity, as reported by (a) Foreman et al., (b) this study.	72
Fig. 4.13	Gas phase centerline velocity as a function of $StT$ and $\phi$ .	73
Fig. 4.14	The comparison between the single- and two-phase centerline velocities.	73
Fig. 4.15	Centerline velocity decay profile.	75
Fig. 4.16	Velocity decay coefficient.	76
Fig. 4.17	Virtual origin of particle-laden flow.	76
Fig. 4.18	Turbulence modulation with respect to the ratio of particle size to turbulence length scale.	78
Fig. 4.19	Turbulence modulation (a), mean slip velocity profiles (b) at $x/D = 2$ .	80
Fig. 4.20	Turbulence modulation at initial jet region as a function of mean slip velocity at different measurement location from the nozzle exit (case 2)	81
Fig. 4.21	Turbulence modulation at initial jet region as a function of mean slip velocity at different particle loading ratio.	83
Fig. 4.22	Turbulence modulation at initial jet region as a function of mean slip velocity at different Reynolds number.	83
Fig. 4.23	Correlation coefficient as a function of axial distance from nozzle exit.	84
Fig.	Correlation coefficient as a function of particle volume loading	84

4.24	ratio	
Fig. 5.1	Schematic of Coaxial Injector.	89
Fig. 5.2	Axial profiles of mean velocities of single phase, two phase, and solid particles.	93
Fig. 5.3	Radial profiles of axial mean velocities.	94
Fig. 5.4	Mean particle distribution of two-phase particle-laden jet.	96
Fig. 5.5	Spatially resolved deviation parameter D of particle number density fluctuations. ( $U_o/U_i=0.57$ , $\Phi=0.48$ ).	98
Fig. 5.6	Influence of velocity ratio on deviation parameter at lateral position.	98
Fig. 5.7	Influence of vorticity on deviation parameter at lateral position.	99
Fig. 5.8	Averaged concentration fields of fuel and oxidizer in shear coaxial injector as a function of velocity ratio. The white contours correspond to the dilution levels $\frac{\theta}{\theta_o} = 0.2$ (RR=0).	101
Fig. 5.9	Averaged concentration fields of fuel and oxidizer in swirl coaxial injector as a function of velocity ratio. The white contours correspond to the dilution levels $\frac{\theta}{\theta_o} = 0.2$ (RR=0).	102
Fig. 5.10	Deviation Index of fuel and oxidizer of shear coaxial injector as a function of the $U_o/U_i$ ; the line and flood contours indicate the fuel rich and oxidizer rich regions, respectively.	105
Fig. 5.11	Deviation Index of fuel and oxidizer of swirl coaxial injector as a function of the $U_o/U_i$ ; the line and flood contours indicate the fuel rich and oxidizer rich regions, respectively.	106
Fig. 5.12	Mixing efficiency of swirl and shear coaxial injectors as a function of measurement location ( $U_o/U_i=0.88$ , particle size (42.5 $\mu\text{m}$ )).	108
Fig. 5.13	The axial evolution of the concentration half-width ( $U_o/U_i=0.88$ , particle size (42.5 $\mu\text{m}$ )).	108
Fig. 5.14	Deviation Index of shear and swirl coaxial injectors as a function of velocity ratio of oxidizer and fuel at $x/D=15$ .	110
Fig. 5.15	Mixing efficiencies of shear and swirl coaxial injectors as a function of velocity ratio ( $x/D=15$ ).	111
Fig. 5.16	The axial evolution of the concentration half-width as a function of recess ratio ( $U_o/U_i=0.57$ ).	112
Fig. 5.17	The axial evolution of the concentration half-width as a function of velocity ratio (RR=2.25).	113
Fig.	Deviation Index of fuel (42.5 $\mu\text{m}$ ) and oxidizer of swirl coaxial	113

- 5.18 injector at  $U_0/U_i=1.23$  and  $RR=2.25$ ; the line and flood contours indicate the fuel rich and oxidizer rich regions, respectively.
- Fig. 5.19 Mixing efficiencies of shear and swirl coaxial injectors as a function of recess ratio ( $x/D=15$ ). *114*

## LIST OF TABLES

Table 1.1	Experimental conditions of previous works.	4
Table 2.1	Loading ratios.	7
Table 3.1	Experimental conditions.	36
Table 4.1	Properties of the particles.	53
Table 4.2	Experimental conditions.	55
Table 4.3	Experimental conditions.	62
Table 5.1	Properties of the particles.	88
Table 5.2	Experimental conditions.	91

# NOMENCLATURE

## *Alphabet*

$B_u$	velocity decay coefficient
$C_d$	drag coefficient acting on a particle, $\frac{24}{Re_p}(1 + 0.15Re_p^{0.687})$
CTI	change in turbulence intensity, $(\sigma_{TP} - \sigma_{SP})/\sigma_{TP}$
D	diameter of central nozzle
$D$	deviation parameter
$D.I.$	index of deviation from injection concentration.
$d_p$	diameter of particle
$E_m$	mixing efficiency (%)
$f$	frequency of liquid sheet oscillation
$g$	gravitational acceleration
$h$	thickness of liquid sheet
J	momentum flux ratio, $\rho_g U_g^2 / \rho_L U_L^2$
$K_u$	self-similarity coefficient
$L_R$	recess length
$l_e$	integral length scale
$M_f$	injection mixture fraction of fuel and oxidizer
$m_f$	local mixture fraction of fuel and oxidizer
$\dot{m}$	mass flow rate
$N$	particle number density
$n$	number of pixel where $(m_f \geq M_f)$
$\bar{n}$	number of pixel where $(m_f < M_f)$
$\dot{Q}$	volume flow rate
$R^2$	correlation coefficient
Re	Reynolds number, $UD/\nu$
$Re_p$	particle Reynolds number, $\rho_f  u_f - u_p  d_p / \mu$
RR	recess ratio, $L_R/D$

$r$	radial distance
$S_{CB}$	swirl number proposed by Sheen et al., $\frac{\int_0^R vu r^2 dr}{R \int_0^R u^2 r dr}$
$S_m$	swirl number proposed by Zhou et al., $\frac{\int_0^R vu r dr}{\int_0^R uu r dr}$
$St$	Strouhal number, $f\sqrt{hr_g}/U_g$
$Stk_0$	Stokes number, $\frac{\rho_p d_p^2 U}{18\mu D}$
$U$	axial velocity
$u'$	axial velocity fluctuation
$u_t$	terminal velocity of particle
$V$	radial velocity
$x$	axial distance
$x_p$	virtual origin

### ***Greek***

$\Theta$	normalized concentration
$\mu_a$	viscosity
$\nu_a$	kinematic viscosity
$\rho_a$	air density
$\sigma$	turbulence intensity
$\tau_p$	time constant of particle
$\tau_f$	time constant of fluid
$\tau_s$	relaxation time of particle
$\phi$	particle mass loading ratio
$\phi_v$	particle volume loading ratio

### ***Subscript***

0	nozzle exit
c	center of the jet

<i>f</i>	gas
<i>l</i>	liquid
<i>o</i>	oxidizer simulant
<i>p</i>	particle
<i>sp</i>	single phase
<i>tp</i>	two phase

# CHAPTER 1

## INTRODUCTION

Metal particles such as Al or Mg and water have been proposed as propellant both for space (Foote and Litchford, 2005, Goroshin et al., 1999) and for underwater propulsion (Miller and Herr, 2004, Foote et al., 1996), due to its high volumetric heat release associated with combustion. Power generation using metal powder fuel propulsion systems includes many processes: pyrolysis, gas-phase diffusion, mixing and combustion. These metal particles difficult to obtaining complete combustion within the combustor length (Pang et al., 2009).The supercavitation underwater vehicle one of the background of the study, uses rocket propulsion system with combustion of hydro-reactive metal fuel unlike other conventional underwater vehicles using the propeller propulsion. When the vehicle proceeds under the water, cavitation occurs on the body surface due to velocity difference between the body and the water. The cavitation on the surface develops rapidly with increasing velocity, and if the cavitation becomes the supercavitation enough to wrap the whole body, the underwater subsequently vehicle escapes from the high drag force of the water, and can potentially reach high speeds over 400 km/h. Moreover, the supercavitation underwater vehicle using the rocket propulsion has a higher propulsive efficiency per unit volume as compared to conventional underwater vehicles because the surrounding water can directly serves as the oxidizer. Aluminum ( $\text{Al}_2\text{O}_3$ ) and Magnesium ( $\text{MgO}_2$ ) are mostly used as the hydro-reactive metal fuels. The combustion mechanism differs from other conventional particles (e.g. coal or gunpowder). Indeed, the oxide film covering the metal surface under the normal state should be melted prior to the reaction with the  $\text{H}_2\text{O}$ . A uniform distribution of the metal particles in the jet helps their total surface to be larger, so the oxide films are able to melt easier. In the combustion reaction of water and hydro-reactive particles, Foote et al. (1996) reported that uniform mixing performance of the water and the hydro-reactive particles causes the decrease of the

ignition temperature and the increase of the flame propagation speed which indicate an increase in the specific impulse. Therefore, in order to design the shear coaxial injector which is able to spray uniformly water and particles as shown in Fig. 1.2, basic experiments on spray characteristics of the solid particles with the fluidization medium are required.

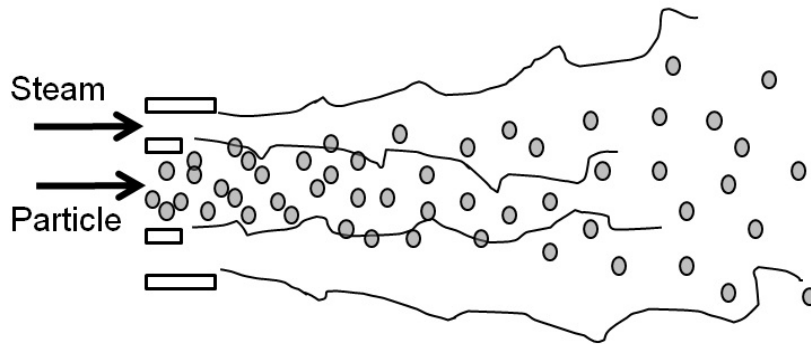


Figure 1.2 Schematic of the particle – steam coaxial jet.

In order to understanding the way particles and fluid interact, a classification can be made, based on their volume or mass loading ratio (Elghobashi, 1994).

**One-way coupling:** in these flows, the effect of the particles on the fluid phase is negligible. It suffices to calculate the fluid phase behavior and subsequently integrate the particle equations of motion. This regime end at a volume loading ratio of  $10^{-6}$  (Elghobashi, 1994). Due to the fact that particle may not follow all fluid motions, so-called preferential concentration can occur. This is especially when the Stokes number equal to unity (Eaton and Fessler, 1994).

**Two-way coupling:** with higher load or with heavier particles, the particle phase starts to influence the fluid phase. This regime, the turbulence level of fluid can be attenuated or augmented, depending on the particle characteristics. Boundaries for the two-way coupling region are between volume loading ratios of  $10^{-5}$  to  $10^{-2}$ .

**Four-way coupling:** if the particle load is increased even future, particle-particle interactions should be taken into account. In this regime, the particle

distribution can become significantly non-random, with large regions of devoid of particles. These structure can be observed in fluidized bed reactors.

In this study, the focus will be on the two-way coupling regime, to ignore the particle-particle interaction.

Investigations about particle injection have been actively carried out to develop coal combustors which are parts of the integrated gasification combined cycle plants (IGCC) since 1980. Modarress et al. (1984) investigated the effect of particle size, jet exit velocity, and loading ratio for an axisymmetric turbulent jet by measuring mean velocities, turbulent intensities, and shear stress. With increase of a particle loading ratio, a linear increase of jet center velocity at  $x/D = 20$ , a reduction of particle spreading angle, and a decrease of turbulent intensity are observed. Fleckhaus et al. (1987) examined the effect of the particle primary diameter on a particle-laden jet. Also they fitted their experimental results with a set of analytical function for improving the basic understanding of a two phase flow phenomena. They concluded that the decrease of the particle primary diameter causes the reduction of the air velocity decay rate and the particle spreading angle due to the decrease of the turbulent intensity. Gillandt et al. (2001) investigated the effects influencing turbulence modulation by analyzing the one-dimensional energy spectra of the axial velocity fluctuations for single and two phase jet flows.

The addition of the particles to the jet causes turbulence damping because turbulence energy in the jet is dissipated by friction with particle surface (Gillandt et al., 2001). Thus, it was found that the turbulent intensity is decreased with increasing total particle surface in the jet. Decreasing the turbulent intensity is related with diminishing the momentum exchange between the jet and the surrounding gas. So, the decrease of the turbulent intensity causes the change in the jet velocity profile. The centerline velocity decay of the two phase jet is slower than that of a single phase jet, and the radial velocity profile of the two phase jet is steeper than that of the single phase jet (Laats, 1966). Besides, the slip velocity is lessened by lowering decay rate of the gas phase due to diminishing the momentum exchange (Modarress et al., 1984). Experiment conditions of all previous works

surveyed are listed in Table 1.1. As shown in Table 1.1, all the researches adopted long orifice lengths from 600 mm to 2025 mm, and large orifice diameters from 10 mm to 25 mm. Due to the limitation of space in the underwater vehicle, the orifice length and diameter should be downsized as compared with others investigations. In this study, with PIV measurement, the profiles of particles velocity, turbulent intensity, and number density are investigated to know the effect of the particle injection conditions on the particle developing region and the particle spreading rate of the two phase jet using the plain orifice type injector.

Table 1.1 Experimental conditions of previous works.

Author	Diameter (mm)	Length (mm)	Reynolds number	Particle diameter ( $\mu\text{m}$ )	Particle density ( $\text{kg/m}^3$ )	Loading ratio
<b>Popper (1974)</b>	25	-	16450~49450	< 50	oil	0.001
<b>Levy (1981)</b>	15	600	20000	180~1200	sand	1.14~3.5
<b>Modarress (1984)</b>	20	1800	13300, 14100	50, 200	2990 glass beads	0.8, 0.85
<b>Shuen (1983)</b>	10.9	981	19000	79~207	2620 sand	0.2, 0.66
<b>Fleckhaus (1987)</b>	13	1000	20000	64, 132	2590 glass beads	0.3
<b>Tsuji (1988)</b>	20	2058	14500~34300	170~1400	1020 polystyrene	0.39~1.85
<b>Barlow (1990)</b>	10	-	780	163	2825 glass beads	6.5~54
<b>Biing-Hwang Jou (1993)</b>	15	2025	20000	210, 780	1020 polystyrene	0.49~3.06
<b>Gillandt (2000)</b>	12	1080	5700	110	glass beads	1
<b>Present Study</b>	2.5~4	15~30	23665~66264	35~50	3970 aluminum oxide	0.116~0.405

In present study, the simple round jet, shear coaxial and swirl coaxial injectors were investigated. The present research covers three topics. The effect of velocity

ratio and recess of spray breakup characteristics in shear coaxial gas-liquid injector with annular liquid to investigate oxidizer characteristics in Chapter 3. Also, the spray characteristics of simple round jets, such as velocity, turbulence intensity and particle distribution, were measured based on the similarity hypothesis in Chapter 4. Since these characteristics are strongly affected by the particle loading ratio and Reynolds number, the effect of these properties on gas-phase properties (velocity and turbulence intensity) were also studied. Finally, the experimental studies on spray characteristics, especially mixing characteristics of particle-laden shear and swirl coaxial injector with the central particle and the annular shear or swirling gas were performed in Chapter 5. This chapter, the spray mixing characteristics of the shear coaxial were investigated as compared with those of the swirl coaxial injector.

## **CHAPTER 2**

### **EXPERIMENT AND MEASUREMENT SYSTEMS**

Flow characteristics of particle-laden jets include the particles number density distribution, velocity fields and turbulent intensity and so forth. The particle number density and half-width of particles were measured from instantaneous images obtained by Mie scattering using CCD camera. A PIV (Particle Image Velocimetry), PTV (Particle Tracking Velocimetry) and a PLLIF (Planar Liquid Laser Induced Fluorescence) technique were used for measuring the concentration distribution. In order to investigate the effect of particle mass loading ratio and injection velocity on the flow characteristics, the automated particle feeder was used.

#### **2.1 Automated Particle Feeder**

Fig. 2.1 shows An automated particle feeder designed to supply constant particle mass flow rates. The particles are contained in a cone type particle feeder inside, and the inside sealed by a polycarbonate cover is pressurized to the same pressure with a tube which the air passes. A screw which passes through the particle feeder inside is rotated by an AC variable speed motor. When the screw spins, particles loaded between the screw's pitch are transported to an airline, and then the particles fluidized by the air are sprayed through the injector orifice.

Fig. 2.2 is a result of particle flow rates test of the particle feeder. In order to get particle flow rates for each feeding condition, particles sprayed through the orifice were collected into a flask of sticky syrup for a certain period of time, and then mass changes were measured by a load cell. Comparing "Direct" with other particle mass flow rates measured from the orifice exit, all feeding conditions are well supplied without any accumulation in the line except for the condition of air flow rate 1.184 g/s and the highest rpm condition. In the condition of air flow rate 1.184 g/s, the air velocity was not enough to carry the particles, so particles are believed to

deposit in the damping chamber. The particle mass loading ratio is the ratio of particle mass flow rate to the gas mass flow rate. The mass loading ratios obtained from the experimental conditions are shown in Table 2.1.

Table 2.1 Loading ratios.

Air flow rate (g/s)	Rpm Levels			
	1	2	3	4
<b>1.184</b>	0.116	0.139	0.195	0.227
<b>1.579</b>	0.216	0.287	0.340	0.386
<b>1.973</b>	0.178	0.227	0.248	0.275
<b>2.368</b>	0.138	0.179	0.232	0.280

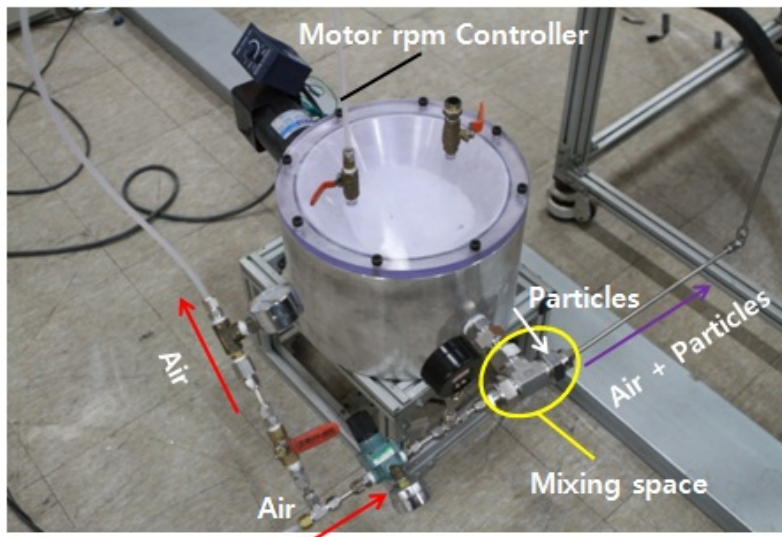


Fig. 2.1 Automated particle feeder.

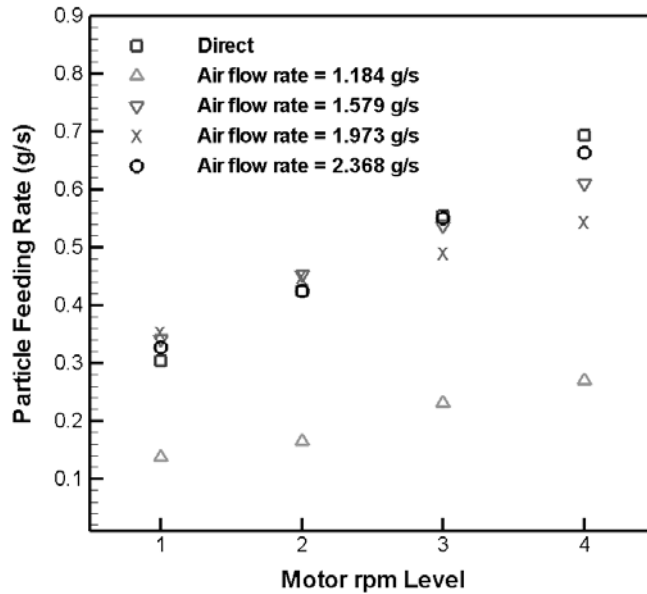


Fig. 2.2 Particle feeding rate test

(Data points represents an average of 10 runs; Direct: particle collected at the feeder exit, other symbols: particle collected at the orifice exit)

## 2.2 Two-phase Jet Measurement Technique

### 2.2.1. Phase Discrimination Using Image Processing

Investigations regarding particle-laden flows have been actively conducted to understand the physical mechanisms and dynamics of such flows. Among many different kinds of measurement techniques, PIV is the most effective measurement in that PIV makes it possible to obtain information regarding an instantaneous whole field measured. Information about particle spray characteristics, such as dispersed particle sizes and number density, can be acquired from the PIV images, as well as data about the flow structures, such as velocity vector fields and turbulent intensity. Farmer (1972) measured the particle size, the number density, and the velocity using a laser interferometer. He determined the particle flow information by means of the signal visibility, as well as by the ratio of AC to DC in the signal

from the interference fringes; however, there is a limitation in that interpreting the data into a meaningful physical mechanism governing the dynamics between the phases is arduous. Yasuda and Sohn (1995) examined the number density in the two-phase flow by counting the peak points in a horizontal profiling of the luminance intensity profile. Although such a method is reasonable, as each peak corresponds to the location of a particle, it may be difficult to represent the concentration of the particles if the particle sizes are varied.

In order to analyze the turbulent structure in the two-phase flow, simultaneous measurements of tracers (1  $\mu\text{m}$ ) and particles (42  $\mu\text{m}$ ) have been carried out with the experimental setup of the particle-laden jet. Tracer particles represent the carrier gas characteristics. In this study, the phase discrimination technique was applied to get images of the tracers and particles separately as same as Cheng et al. (2010) After the phase discrimination process tracer only images and particle only images obtained. Tracer only image analyzed using Particle Image Velocimetry (PIV) technique, and particle only image analyzed by Particle Tracking Velocimetry (PTV) technique. Figure 2.7 demonstrate the image processing of separating raw particle images into images of tracer and large particles.

The first step (Fig. 2.7b) in the phase discrimination process requires preconditioning the raw images in order to remove the background and image noise from the particle-candidates by applying Fourier transform (FFT) filter. FFT cross-correlation function that is widely used for statistical PIV evaluation for determining velocity fields. However, this study this filter here is not to determine the velocity but to remove the background noise in the images. Simply, cross-correlation algorithms calculate particle displacement between interrogation sub-windows (i.e. 32 x 32 pixels) from two frames, frame A and B and separated by a short time, by extracting the maximum peak of the maximum peak (fig. 2.3).

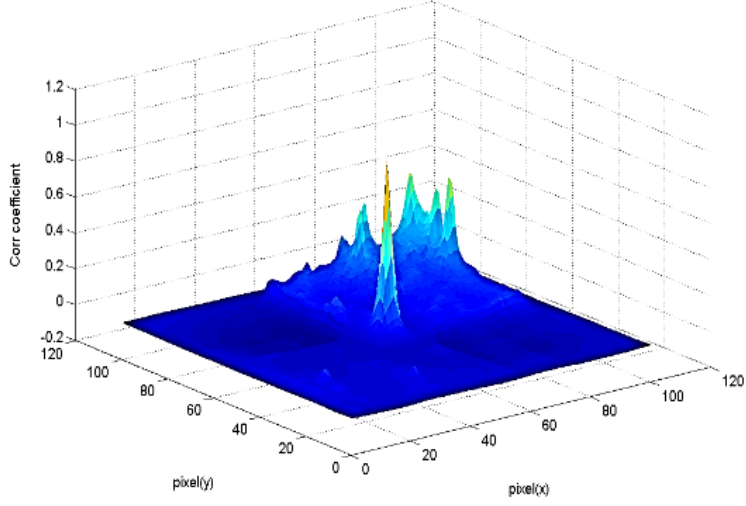


Fig. 2.3 FFT cross-correlation map.

Then the position of the maximum peak  $dx_{\max}$  and  $dy_{\max}$  was obtained that represents the pixel offset from frame A to B during the time difference between these frames. The filter proposed here uses the displacement measured between the two sub-windows to shift the sub-window in frame A so it best overlaps with the interrogated sub-window in frame B. After this operation has been performed the two image intensity fields from both sub-windows should overlap. By multiplying the intensity field of both sub-windows, one would expect the intensity peaks from the overlapped particles to become amplified when compared to other background pixels. Therefore, background noise can be easily removed by this technique. Mathematically, the cross-correlation map function is described by

$$\phi_{g_A g_B}(m, n) = \sum_{i=0}^{M-1} \sum_{j=0}^{N-1} g_A(i, j) g_B(i + m, j + n) \quad (2.1)$$

where  $m$  and  $n$  are the shift in the correlation map,  $g_A$  and  $g_B$  represent the grayscale intensity images of frame A and frame B, respectively, and  $M$  and  $N$

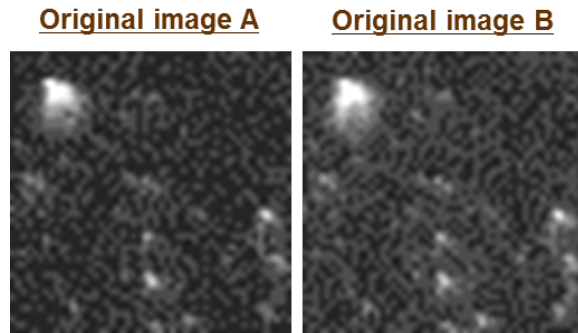
describe the size of the sub-window (i.e., 32 9 32 pixels). The correlation peak position is given by

$$\Phi_{g_A g_B}(dx_{max}, dy_{max}) = \max(\Phi_{g_A g_B}(m, n)) \quad (2.2)$$

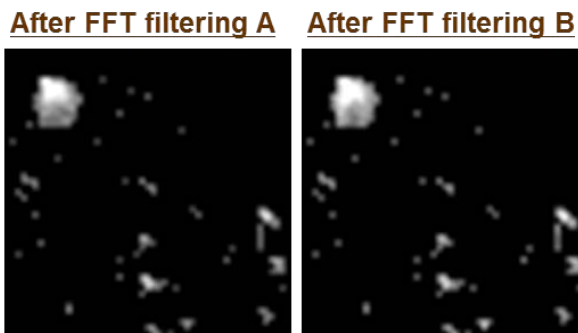
The final FFT filtered frame A image is given by

$$g_A(i, j) = \begin{cases} g_A(i, j), & \text{if } g_a(i + dx_{max}, j + dy_{max})g_B > T \\ 0, & \text{otherwise} \end{cases} \quad (2.3)$$

where T, corresponding to half a standard deviation was chosen like Cheng et al. (2010) Figure 2.4 shows the valid particles are automatically recognized from the original images after filtering.



(a) Original image



(b) After FFT filtering

Fig. 2.4 FFT filtering method showing the interrogation spots before and after filtering

Comparing the images before and after FFT filtering, it can be seen that most of the pixels set to zero intensity by the FFT filter which is below a certain threshold intensity value. Figure 2.5 shows the original pixel intensity distribution of a 600 PIV images, filtered out images and the remaining pixels after FFT filtering. From this figure most of the pixels of intensity lower than 12 were considered as background or noise by FFT algorithm.

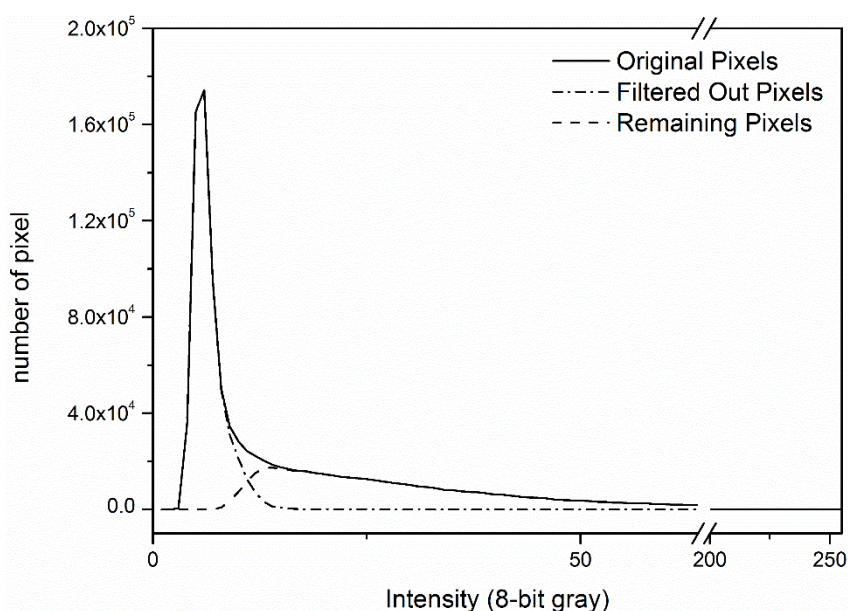


Fig. 2.5 The intensity distribution of original, cutoff and remained pixels (mean of 600 images)

The next step in the phase discrimination process involves applying a relative intensity variation threshold algorithm that helps separate pixels corresponding to particles and their surrounding background pixels (Fig. 2.4c). The relative intensity variation. Refers to the intensity change from a given pixel to its neighboring pixels, Here, a thresholding is used to “erode” the low-intensity edges of the particles leaving the high-intensity particle cores. This is done by comparing each pixel

intensity in the image to its surrounding four connected pixels and if the intensity is lower than a given percentage of any adjacent one, it is considered to be a background pixel and is set to zero intensity. The operator can be expressed as follows:

$$g(i,j) = \begin{cases} g(i,j) & \text{if } g(i,j) > g(i-1,j) * c \\ & g(i,j) > g(i+1,j) * c \\ & g(i,j) > g(i,j-1) * c \\ & g(i,j) > g(i-1,j+1) * c \\ 0 & \text{otherwise} \end{cases} \quad (2.4)$$

Where  $c$  is the intensity variation threshold percentage, this value range from 0 to 1 and varies depending on the image parameters such as the particle size, shape and orientation. Generally, the core can be identified using a threshold based on a gradient drop in intensity between adjacent pixels proportional to one standard deviation of the peak intensity (50-70% of the peak intensity depending on the core size). This study, values of  $c=0.5-0.7$  were tested with  $c=0.6$  giving the best result. This algorithm works best for separating high-intensity large particles (8-20 pixels) from the surrounding background noise by emphasize the high-intensity core of large particles.

This is followed by local maximum algorithm proposed by Khalitov and Longmire (2002) that isolating small particles with lower intensities from the surrounding background noise (Fig. 2d). The operator can be expressed as follows:

$$g(i,j) = \begin{cases} g(i,j), & \text{if } g(i,j) > g_{satu} \\ & g(i,j)^2 > g(i,j-1)g(i,j+1) \\ & g(i,j)^2 > g(i-1,j)g(i+1,j) \\ & g(i,j)^2 > g(i-1,j+1)g(i+1,j-1) \\ & g(i,j)^2 > g(i-1,j-1)g(i+1,j+1) \\ 0, & \text{otherwise} \end{cases} \quad (2.5)$$

The next step identified each particle that involves defining each particle through examining all the pixels in the post-processed particle image. The principle of the particle detection code used a bwlabel function in MATLAB that the 8-pixel neighbor algorithm. After detecting, each of particles are labeled as a number to count the number of particles in the post-processed particle image, and then the number of pixels within each closed curve of the particle is determined, so each cross-sectional area of the particles can be calculated with the number of pixels inside the closed circle. From the area, each particle diameter can also be obtained. From this technique particle volume concentration ( $\nu$ ) can be easily obtained. Particle intensity  $I$ , is the mean intensity of each identified pixels, and is calculated by

$$I = \frac{\sum_i^n I_i}{n} \quad (2.6)$$

The final step in the phase discrimination process is obtain probability distribution of all the identified particles by their pixel size and average particles intensity (Fig. 2.6). Figure 2.6 shows a 2D contour map of the single (Fig. 2.6a) and two-phase (Fig. 2.6b) particle concentration distribution for an average of 600 images. Compared tracer only single-phase result (Fig. 2.6a) and two-phase result (Fig. 2.6b) large particle images ranged from 5 to 25 pixels and average intensity ranged from more than 200 (denoted in Fig. 2.6b by particles enclosed in the red dash line). After particle identification process small and large particle only images was obtained separately (Fig. 2.7e, f). These phase discrimination techniques has been described in great detail by Cheng et al. (2010).

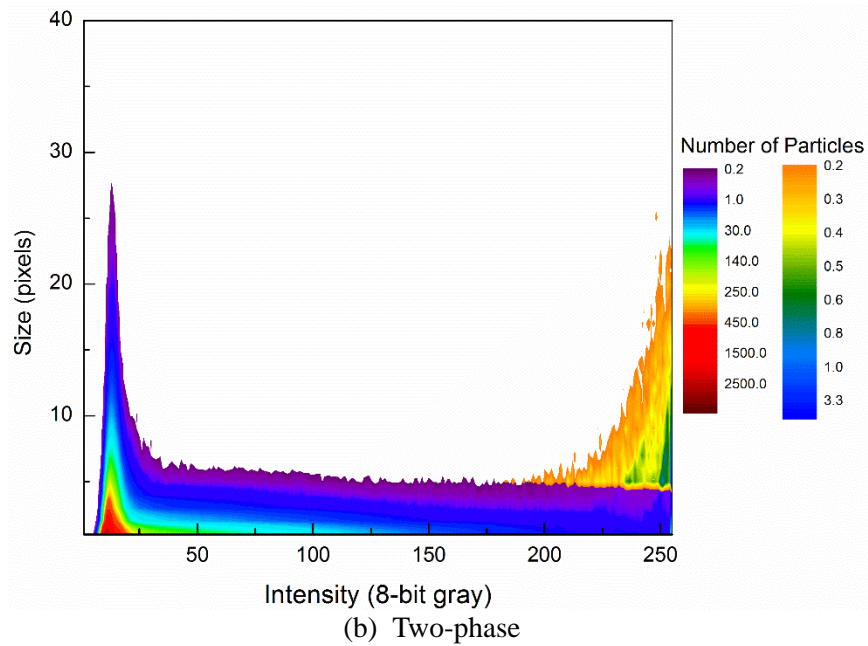
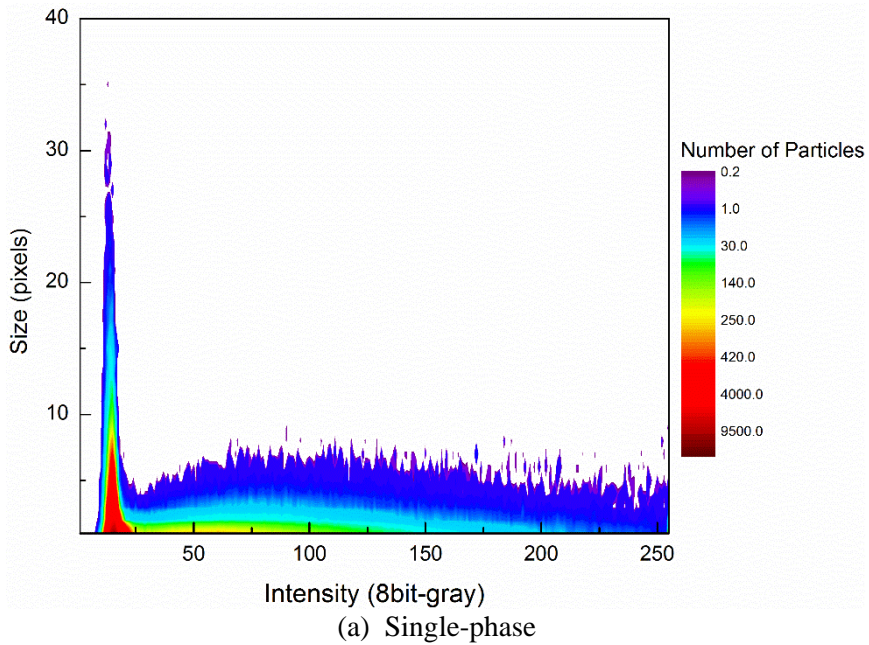


Fig. 2.6 Particle distribution contour map of the average of all the particle obtained from 300 PIV images taken in single and two-phase particle-laden jet.

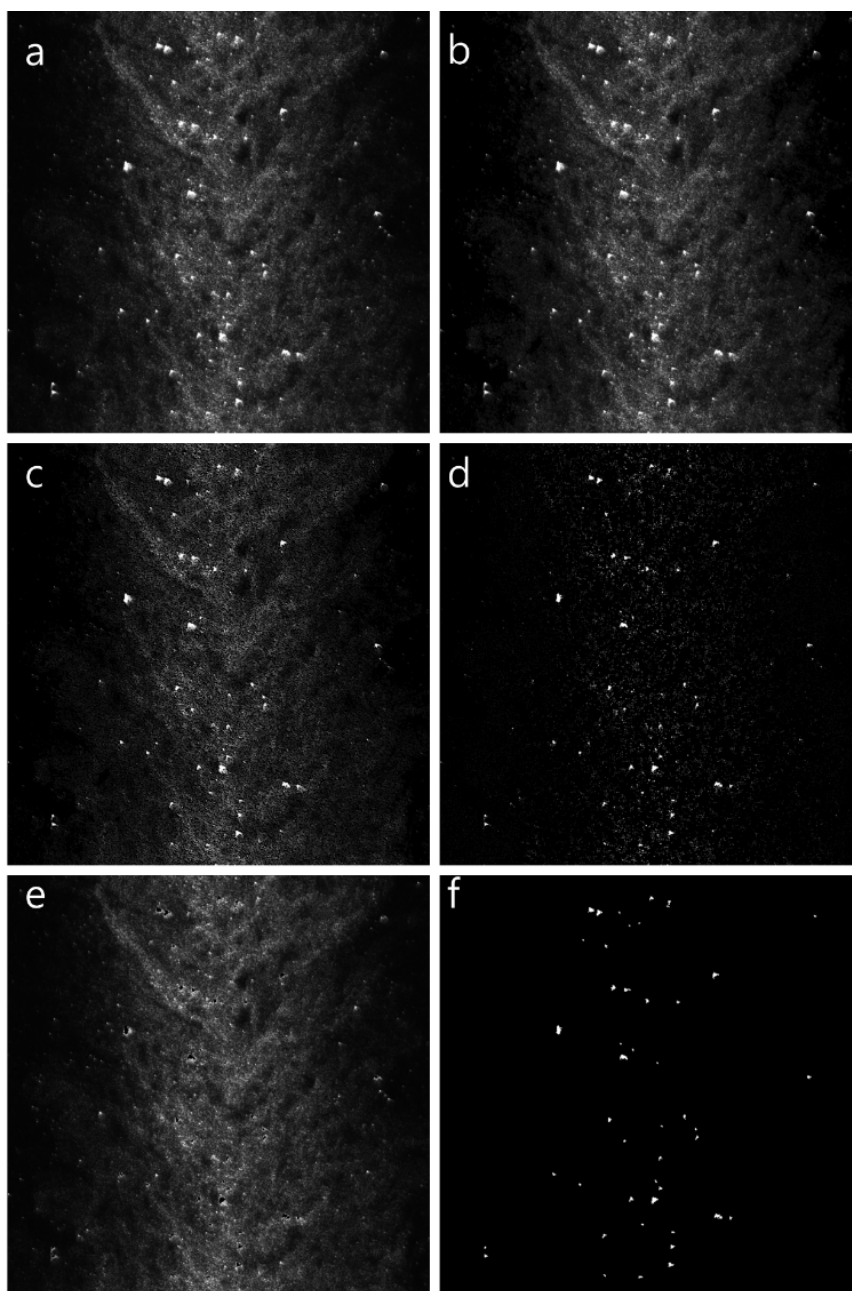


Fig.2.7 Image filtering and separation sequence a. original image; b. image after fft filtering; c. image after fft filtering and relative intensity filtering; d. image after fft filtering, relative intensity and local max filtering; e. separated small particles; f. separated large particles

### 2.2.2. Validation of the Image Processing Technique

To validate the image processing technique adopted in this study, artificial two-phase flow images were generated by combining tracer only images (Fig. 2.8a) and particle only images (Fig. 2.8b). Because accurate velocity field information can be obtained from tracer only images, and flow velocity field obtained from the separated tracer only images. Then compared each original tracer only image and separated tracer only image to give a measure of the cross-talk error. This procedure is nearly same as Kiger and Pan (2000) and Zhang et al. (2008) to validate their image processing technique. Figure 2.8c shows the artificial two-phase image that overlapping original tracer only image without large particle (Fig. 2.8a) and large particle only image (Fig. 2.8b). Then the tracer only image (Fig. 2.8d) was obtained by separating the large particle images from the artificial two-phase image with image processing technique. Using these technique 600 instantaneous flow velocity field obtained from separated tracer only images were ensemble-averaged to get the mean velocity and velocity fluctuation profiles and compared with result of the real tracer only images. Figure 2.9 represents the magnitude contours of the streamwise fluid velocity component obtained from tracer only original images (Fig. 2.9a) and the processed tracer only images (Fig. 2.9b), respectively. From these images the influence of phase discrimination method on fluid velocity is quite small. Figure 2.10a and b shows mean velocity and axial velocity fluctuation profiles obtained from real and processed tracer only images. Both results look nearly similar and the mean difference in entire flow field is about less than 1% in the streamwise and less than 2% in the streamwise velocity fluctuation. This result shows that the effect of the phase discrimination of tracers and large particles from the two-phase images is sufficiently small.

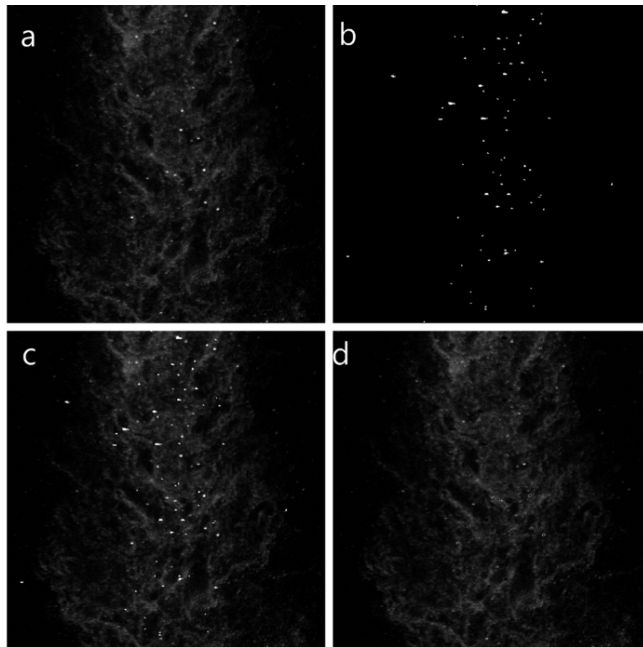


Fig. 2.8 Representative images showing the image processing for the tracer only particle images; **a**. tracer only image; **b**. particle only image; **c**. two-phase flow image created by overlapping Fig. 4a and Fig. 4b; **d**. tracer only image separated by the image processing technique

### Instantaneous velocity field

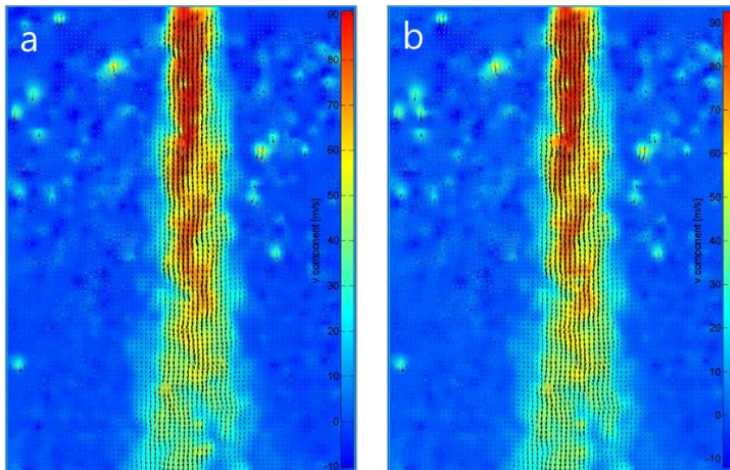
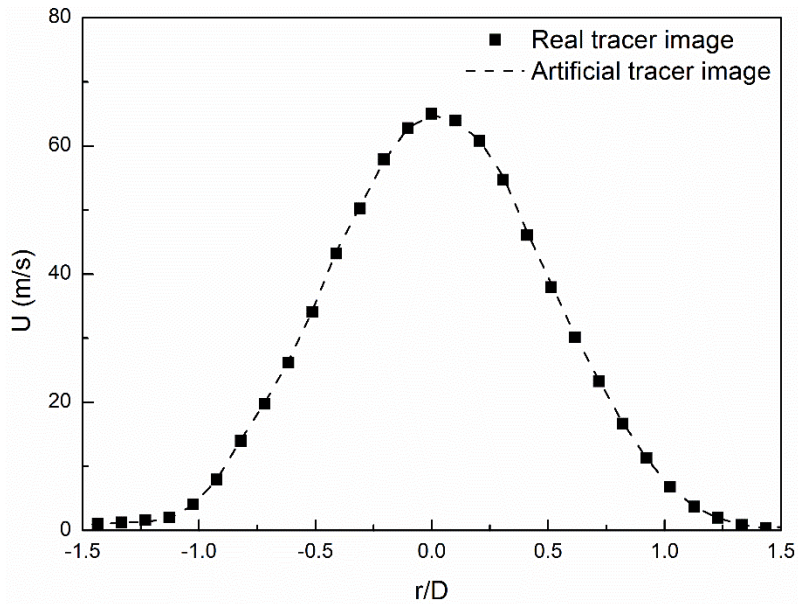
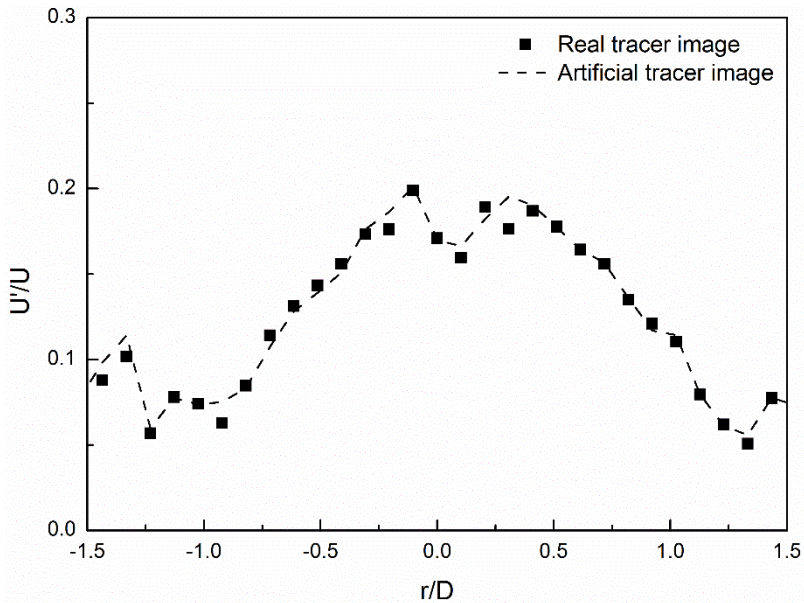


Fig. 2.9 Instantaneous streamwise velocity component obtained from **a** the original tracer only images, **b** the processed tracer only images.



(a) axial mean velocity profile



(b) axial velocity fluctuation profile

Fig. 2.10 Comparison of (a) mean velocity and (b) turbulent intensity profiles obtained from real and processed tracer only images

## 2.3 Simultaneous PIV and Acetone PLIF Diagnostics

### 2.3.1 Particle Image Velocimetry

In this study, gas flow structures have been measured using Particle Image Velocimetry (PIV). PIV is an attractive and useful technique for capturing instantaneous flow field. PIV is the simultaneous measurement of fluid or particulate velocity vectors at many (e.g., thousands) points, using optical imaging techniques. The measurements are usually made in planar “slices” of the flow field. The technique can be extended for three-dimensional measurements. Accuracy and spatial resolution are comparable to LDV or thermal anemometry. PIV measurement does not disturb the fluid flow and has high accuracy and resolution. It is a qualitative visualization method that can capture instantaneous 2 dimensional velocity fields and additional information such as turbulent intensity, strain rate, and vorticity. Several processes are required to get useful information: Tracing particles added to the steam, the laser illumination with periodic time delay, the recording of Mie scattering images, and the post process evolution of recorded images.

Fig. 2.11 shows typical procedures of PIV measurements. First, seeding particles those have proper properties are added to the flow. Second, a laser sheet beam illuminates those particles twice with a short time interval. Third, Mie scattering signals from seeding particles surface due to the laser illumination are captured by a CCD camera. Fourth, with the information of the laser illumination interval and the distance particles moved during the interval, vector fields can be reconstructed.

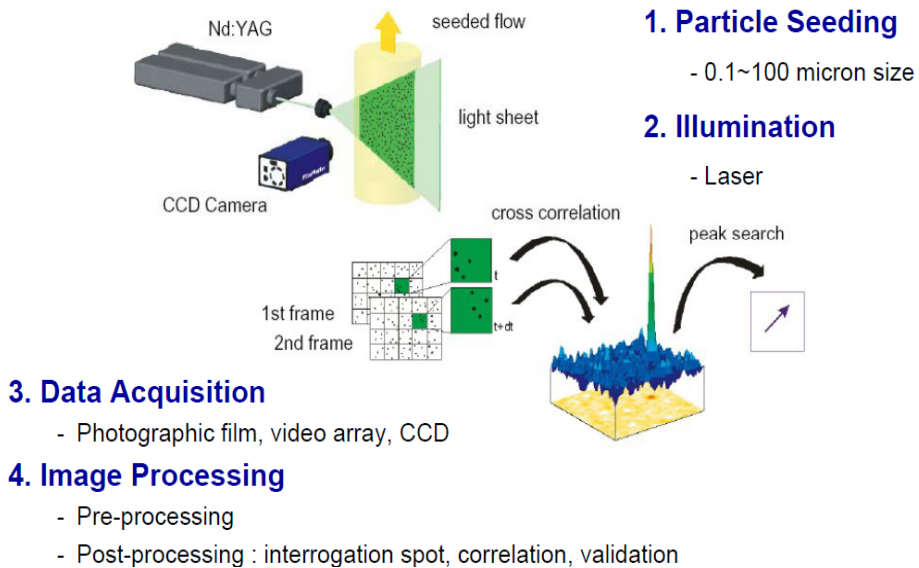


Fig. 2.11 Typical procedure of PIV

Generally, a double pulsed Nd-YAG laser is used as a light source and a high speed CCD camera is employed to obtain instantaneous particle images at a measurement plane. There are no specific rules for particle seeding system; however, the size of particle should be determined by considering whether particles can follow the flow well or not (Ahn et al., 2003). In most cases, it is necessary to add tracer particles into the flow. These particles are illuminated at the measurement plane of the flow at least twice times within a short interval. The light scattered or fluoresced by particle is recorded either on a single frame or on sequential frames. The displacement of the particle images recorded by the light pulses is calculated through evaluation of the PIV.

To calculate the displacement of the particles grabbed by a CCD camera, it is necessary to divide the image into a grid. The grid is called as an interrogation spot. After setting the interrogation spot size, one interrogation spot of the first images is picked and compared with all the interrogation spot of the second images. The displacement between the interrogation spot of the first image and the interrogation

spot of the second image represents one vector of flow field. By conducting this work in all the interrogation spots, whole vectors of flow-field are obtained. This process is called as a correlation.

The correlation function is expressed as follows:

$$h(s_x, s_y) = \int_0^{\infty} \int_0^{\infty} f(x, y)g(x + s_x, y + s_y)dx dy \quad (2.7)$$

The expression can become simple as conducting Fourier transformation for a convenience's sake in calculating. Here,  $F$  and  $G$  are Fourier transformed function of each  $f$  and  $g$ , and they mean Fourier transform operator.

$$F(h) = F^*(f) \times F(g) = F^* \times G \quad (2.8)$$

$$h = F^{-1}(F^* \times G) \quad (2.9)$$

Equation 2.7 is the same expression of spatial masking in an image processing technique. Thus, it means that a correlation is a kind of masking concepts. According to this concept, the correlation can be called as a process to figure out distribution of the similarity by signal distribution in an image plane. Equation 2.9 makes us use fast Fourier transform (FFT) algorithm which reduces the calculation time drastically. The interrogation spot size of  $2n \times 2n$  should be chosen to use FFT algorithm because FFT algorithm is a method by dividing even and odd terms. However, the calculation time becomes short by  $\log_2 N/N$  times comparing with direct Fourier transform (DFT) algorithm.

A correlation method is separated into auto-correlation and cross-correlation by the number of functions. Mathematically, auto-correlation is the case;  $f(x; y) = g(x; y)$  in Eq. 2.7 and cross-correlation is the case;  $f(x; y) \neq g(x; y)$ . Experimentally, an auto-correlation is used for the case where the first image at  $t = t_1$  and the second

image at  $t = t_2$  are recorded in one frame (called as a single frame/double exposure mode) and cross-correlation is used for the case where the first image at  $t = t_1$  and the second image at  $t = t_2$  are recorded in separated frames (called as a double frame/single exposure mode). Comparing with an auto-correlation method, a cross-correlation method has some merits as follows:

1. Directional ambiguity problem can be avoided easily.
2. The algorithm is simple because there is only one peak as a result of correlation.
3. Dynamic range is relatively large.

The biggest challenge in applying the PIV technique to velocity measurements in particle-laden flows is finding proper time interval between lasers pulsed due to large velocity difference of the jet. Therefore, trial and error method was used to obtain valid velocity vectors. To reduce erroneous vector and get valid results, the additional process for the detection of correct vectors has to be performed during the cross correlation process.

The dispersed phase (large particle) velocity fields were computed using open source particle tracking algorithm (Brevis et al., 2011) due to number density of large particle was lower for using PIV technique. This particle tracking algorithm consist of several steps. In the first step, particles corresponding to the dispersed phase are identified by Gaussian mask technique and their centroids are stored. In second step, the algorithm operates on a group of particles already identified in sub-windows. Each particle in a group is shifted according to local flow field, and the distance to its nearest neighbor in the second frame is calculated. A particle pair is matched if its deviation is less than the tolerance times the median deviation of the group. The velocity of each matched particle is checked by a median filter using the velocity of its matched neighbors.

### 2.3.2 Acetone PLIF

#### PLIF System

Acetone vapor luminescence has been studied for many years.(Ambrose et al., 1974, Lozano et al., 1992, Thurber et al., 1998, Ritchie, 2006, Filatyev et al., 2007, Shelar et al., 2013, Cai et al., 2011) The research has continued to improve as the available equipment has improved, but the work has focused on fluorescence more than phosphorescence. The range of testing conditions, from near vacuum to atmospheric pressure and near to mid-UV excitation, has also lead to multiple studies of acetone's properties.

Acetone has many advantages over other fluorescing alternatives. Most importantly, acetone fluorescence in isobaric, isothermal flows is known to scale linearly with concentration (and laser power under most conditions), which is not true for many fluorescing molecules. In the absence of O<sub>2</sub>, the integrated phosphorescence emission for acetone vapor is stronger than its fluorescence; the phosphorescence yield is 1.8% to just 0.2% for the fluorescence yield.(Lozano, 1992) Phosphorescence also has a much longer lifetime in vapor (200  $\mu$ s versus 4 ns for fluorescence).(Lozano, 1992) While the two emissions can be separated temporally, spectral separation is difficult due to significant overlap of the spectra. Because acetone fluorescence is so short-lived, it is not significantly quenched by oxygen unlike many other fluorescing molecules. However, the phosphorescence is strongly quenched by oxygen,(Lozano, 1992) leaving just a strong fluorescence signal in the conditions in these experiments. Also, acetone absorbs ultraviolet light (225 - 320 nm) but fluoresces in the blue (350 - 550 nm). Elastically scattered light is easily filtered out by simple glass optics since the absorption and emission spectra do not overlap. For the current work, fluorescence signal were collected with UV-Nikkor 105mm/f 4.5 objective. Because UV light can't penetrate the common glass. Spectral bandpass filter (Schott BG 25) limit the 532 nm laser light that reaches the camera array (PI-MAX 1K) while passing fluorescence emission in the blue range. Transmittance of BG 25 filter is shown in Fig. 2.12. Excitation using a frequency-

quadrupled Nd:YAG laser (Quanta-Ray GCR 150 delivering  $\approx 40 \text{ mJ pulse}^{-1}$ ) at 266nm, is very near the peak in the absorption spectrum.

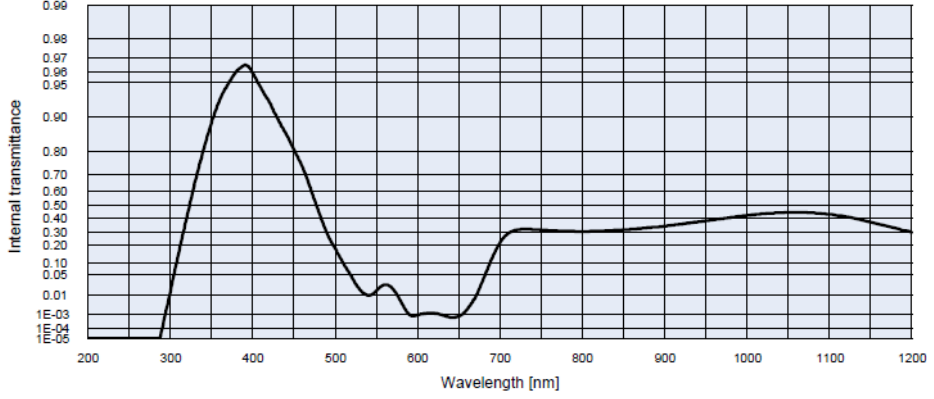


Fig. 2.12 Transmittance of BG 25

#### PLIF data reduction

As with any optical experiments, there were several issues that had to be considered when examining the acquired images for quantitative information. As seen in Equation 2.10, the signal from the camera,  $S(x,r,t)$ , is a combination of light from various sources such as background light from the room,  $B_{room}(x,r,t)$ , background light generated by the laser pulse,  $B_{laser}(x,r,t)$ , the fluorescence signal from the acetone,  $F(x,r,t)$  and varies with downstream location ( $x$ ), radial position ( $r$ ) and time ( $t$ ).

$$S(x,r,t) = B_{room}(x,r,t) + B_{laser}(x,r,t) + F(x,r,t) \quad (2.10)$$

The laser-generated background light of 266 nm laser (for acetone PLIF) and 532 nm light (for PIV and PTV) are largely filtered out by the bandpass filter (BG 25), so laser-generated background light can be ignored. Therefore,  $S(x,r,t)$  to be redefined using Equation 2.11.

$$S(x, r, t) = B_{room}(x, r, t) + F(x, r, t) \quad (2.11)$$

The details of the fluorescence signal shown as below equation 2.12. (Ritchie, 2006)

$$F(x, r, t) = CE_0E'(x)E'(t)E'(r)\chi(x, r, t) \quad (2.12)$$

Where C is a constant based on the efficiency of the generation and collection of the fluorescence.  $E_0$  is the nominal initial laser energy.  $E'(x)$  is the correction factor for the relative strength of the laser sheet at distance x downstream from the jet exit (corrected by laser sheet profile).  $E'(t)$  is the correction factor for the relative strength of the given laser shot based on the shot-by-shot fluctuation in the laser energy (corrected by laser intensity monitoring).  $E'(r)$  is the correction factor for the relative strength of the laser sheet due to losses from laser absorption by acetone at the given radial position in the flow (corrected by Beer's law). The local mole fraction of acetone ( $\chi(x, r, t)$ ) is the final factor in determining the fluorescence signal and is the desired result from the measurements.

As just described, several pieces of data are needed to convert raw images into quantitative measurements of acetone concentration. The camera has an array of 1024 x 1024 pixels; pixels were binned 2 x 2 before readout to further reduced noise in the original signal. Just before correct original image, acetone fluorescence results are processed with a 3 x 3 median filter to reduce noise levels with the least compromise in spatial resolution (Fig. 2.15b), (Ghandhi, 2006) Background images was acquired with no acetone present and no laser running. This provided a measure of the light generated by other sources in the room, such as computer monitor. Figure 2.13 shows the variation in energy from one laser shot to the next was specified as less than  $\pm 10\%$  for the laser.

Shot by shot laser sheet is directed by a fused silica flat to a beam sampler for sheet intensity and profile monitoring. The cross-sheet profile of the 266nm sheet is monitored by measuring the fluorescence signal from the beam sampler, resulting in images of the form shown in figure 2.14. Averaged sheet profile fitted with curve line to smoothing sheet profile.

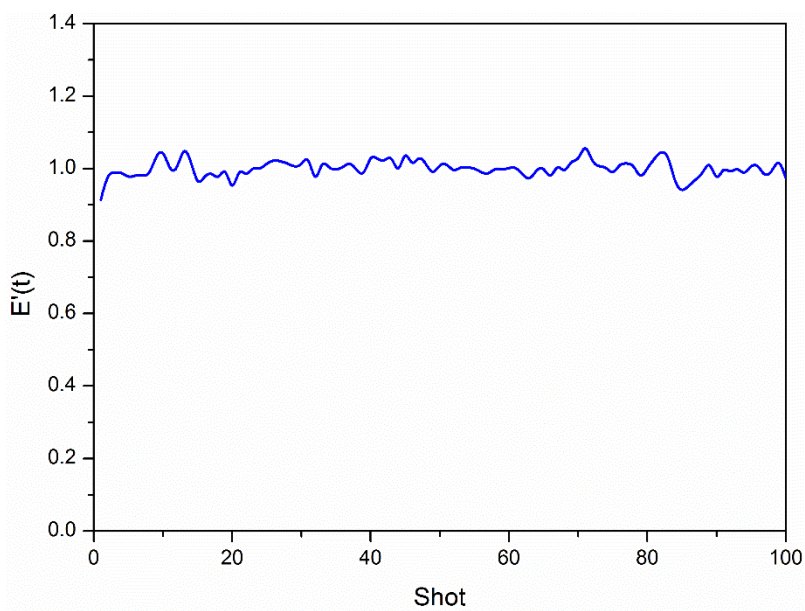


Fig. 2.13 Shot by shot normalized laser intensity

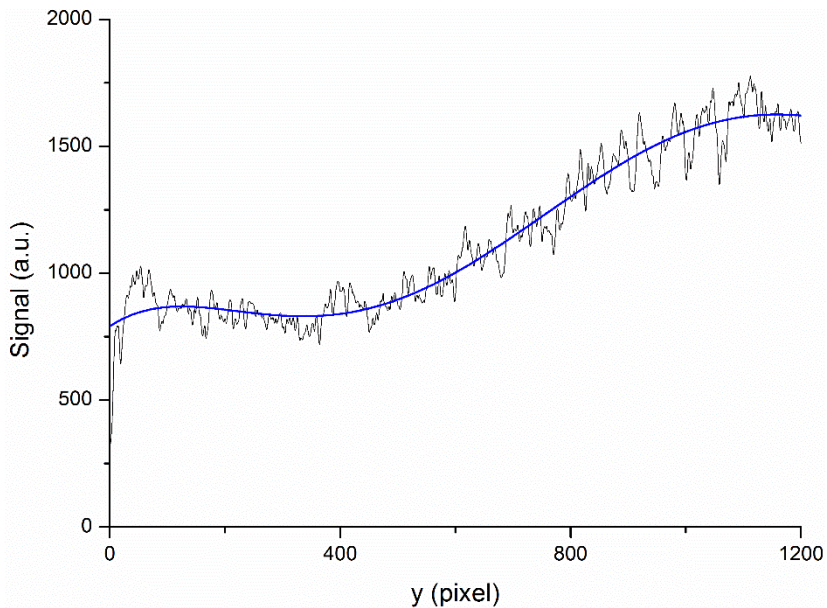


Fig. 2.14 Laser sheet profile

Having described the corrections applied to the images, a step-by-step description of the correction procedure is in order. Before correcting images of the flow field, several steps were taken. First, the average background images were created from the acquired background images. Second, a laser sheet profile and shot-by-shot intensity variation was created from the reflected images of the beam sampler. Finally, the constant that relates signal intensity to acetone concentration is calculated. From these values, correction of the data images has begun.

Image correction started by processed original images with 3 x 3 median filter to reduce noise level (Fig. 2.15b). The average background signal subtracted from after median filtered image and shot-by-shot laser energy fluctuation of the laser power was calculated for each frame in the image set after background subtraction (Fig. 2.15c). The laser sheet profile correction was applied to the all the images by acquired lase sheet from beam sampler and laser sheet attenuation to the sheet propagation direction was corrected by Beer's Law (Equation. 2.13).

$$I = I_0 e^{-\alpha s} \quad (2.13)$$

Where  $I$  is the local laser intensity  $I_0$  is the initial intensity and  $s$  is the path length. The estimated attenuation coefficient for the scattering of the 266 nm sheet is 16 times this  $\alpha$ , reflecting the known  $\lambda^{-4}$ .

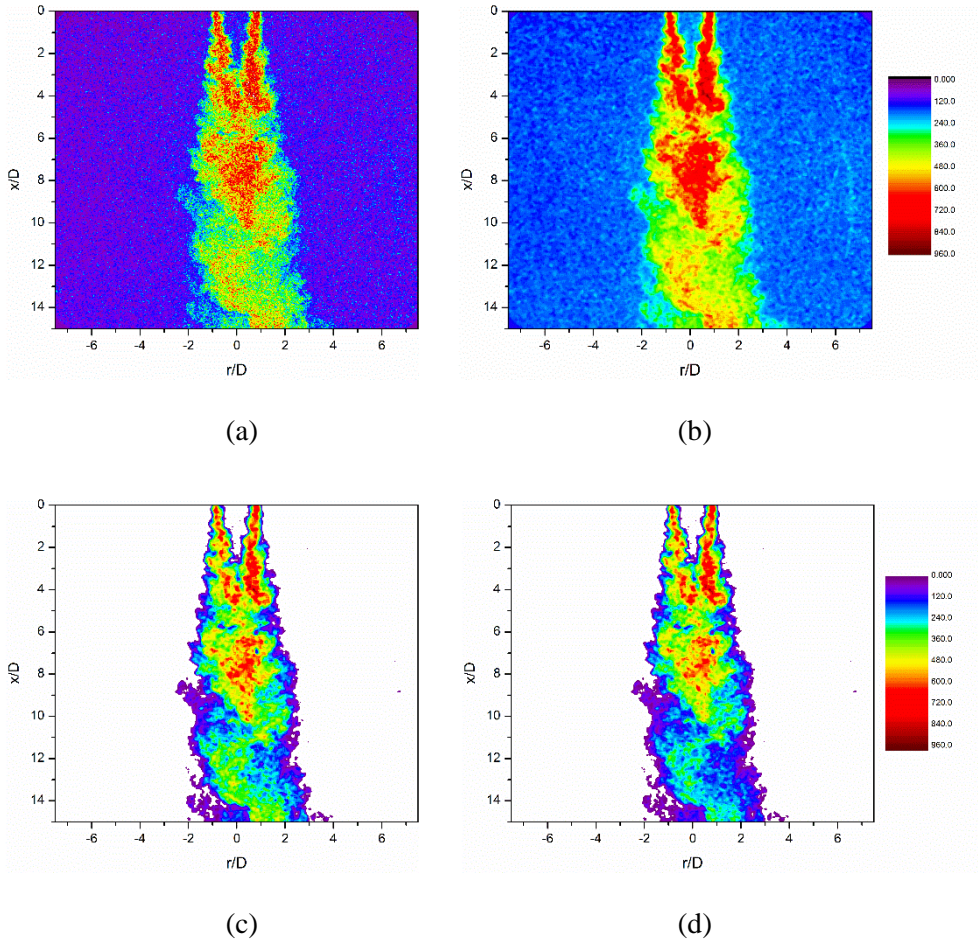


Fig. 2.15 An image at four stages of the correction procedure: (a) the original image, (b) after median filtered, (c) after background subtraction and laser energy fluctuation correction, and (d) after laser sheet profile and absorption corrections.

### 2.4.3 Simultaneous Measurements System

Figure 2.16 shows the experimental setup for PIV and Acetone PLIF measurements. The velocity field and the acetone concentrations were measured simultaneously from the test section and the mixing between the outer jet and central particles was examined. As a laser system for the simultaneous measurements of the flow field, double pulsed Nd:YAG laser (Continuum Surelite II PIV) and a fourth-harmonic Nd:YAG laser system (Quanta Ray GCR 150) were used.

For PIV measurement, two second-harmonic beams ( $\lambda = 532$  nm) were used. The two beams of the dual head Nd:YAG laser (Continuum Surelite II PIV) were provided at intervals depend on flow conditions. The other beam of the fourth-harmonic beam ( $\lambda = 266$  nm) Nd:YAG laser (Quanta Ray GCR 150) was used for acetone PLIF. 266 nm beam produced through the fourth-harmonic ND:YAG was combined with the 532 nm beams from PIV laser at dichroic mirror which allow 532 nm beam to be transmitted and UV beam (266 nm) to be reflected. The combined beams were changed to sheet beams through the set of cylindrical lenses. A delay generator controlled the time separation among three laser beams, CCD camera, and ICCD camera. The pulse separation was confirmed using a photo-diode. Scattering signals from seeding particles were recorded on a high resolution (1600×1200) CCD camera (Viewworks, VH-2MC-M) equipped with f/2.8 AF Micro Nikkor 105 mm lens. Velocity vectors were calculated by means of FFT-based cross-correlation technique. The delay generator controlled the opening time of the camera shutter for the synchronization with the laser pulse.

For Acetone PLIF measurements, the 532 nm beam from the Nd:YAG laser (Quanta Ray GCR 150) was changed to 266 nm with after it passes the fourth-harmonic generator. The acetone fluorescence bands ( $\lambda = 350 \sim 550$  nm) was collected with a UV-Nikkor 105 mm f/4.5 lens. The image was focused onto ICCD camera (Princeton Instrument, PI-MAX 1K, 1024×1024 pixels) with pixels binned 2 x 2 before readout. This camera was fitted with BG 25 color glass filters to block

scattering signal and the incident light of laser. Immediately before entering the flow facility, a portion of the fourth-harmonic laser sheet (266 nm) is directed by a fused silica flat to beam sampler for laser sheet monitoring.

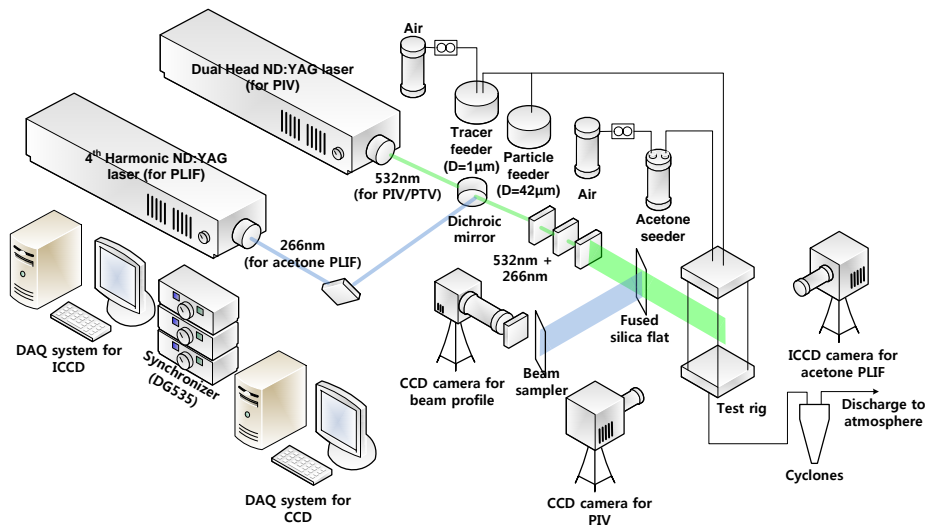


Fig. 2.16 Experimental setup for PIV and Acetone PLIF simultaneous measurements.

## CHAPTER 3

# SPRAY CHARACTERISTICS OF GAS/LIQUID SHEAR COAXIAL INJECTOR WITH ANNULAR LIQUID SHEETS

### 3.1 Background and Objectives

In order to design a shear coaxial injector for supercavitating underwater vehicle, propellant of that system is hydro-reactive solid particle with sea water. When the vehicle proceeds under the water, cavitation occurs on the surface develops rapidly with increasing velocity, and if the cavitation becomes the supercavitation enough to wrap the whole body, the underwater subsequently vehicle escapes from the high drag force of the water, and can potentially reach high speed over 400 km/h. Supercavitation underwater vehicle using the hydro-reactive solid particle as a propellant has a higher propulsive efficiency per unit volume as compared to conventional underwater vehicles because the surrounding water can directly use as an oxidizer. In the combustion reaction of water and hydro-reactive particles, Foote et al. (1996) reported that uniform mixing performance of the water and the hydro-reactive particles causes the decrease of the ignition temperature and the increase of the flame propagation speed which indicate an increase in the specific impulse. Aluminum oxide ( $Al_2O_3$ ) and Magnesium oxide ( $MgO_2$ ) are commonly used as the hydro-reactive propellant, these solid particles do not move themselves without other liquid or gas phase matters. Therefore basic experiments were conducted in gas-liquid shear coaxial injector, instead of solid-liquid coaxial injector. Coaxial injector and impinging injector is widely used, coaxial injector classified by swirl coaxial injector and shear coaxial injector. Among these injector shear coaxial injector characteristics is low pressure drop, high reliability and easy to design (Bayvel, 1993).

The interaction between the gas and liquid phase at specific condition, self-pulsation occurs with intensive scream and strong mass flow rate oscillation. Self-

pulsation can cause harmful disturbance on the acoustic field and make a heat release oscillation. Thus that affects unstable combustion, so this phenomenon must be controlled. In the mid-1970s Russia, self-pulsation phenomenon was discovered during a test of reduced rating conditions in a LOX-hydrogen engine (Bazarov and Lul'ka, 1978, Bazarov, 1995). Bazarov and Yang (1998) conducted experimental study on the influence of operation condition and design parameters such as ambient pressure, pressure drop and recess length. According to his results, the LOX post recess length was most important parameter to determine self-pulsation characteristics, and he suggests some idea to suppress self-pulsation phenomena. The study of liquid annular sheet with different geometric configuration has been conducted with the effect of gravity, gas/liquid velocity ratios and inner and outer gas regions. Shen et al. carried out a linear analysis on the annular viscous liquid jet moving in an inviscid gas medium. The gas medium always enhances the annular jet instability. It is found that the surface tension effect suppresses the instability of the annular viscous liquid jet. The inner gas is revealed to be more effective to breakup up the annular liquid jet than outer gas (Shen and Li, 1996a, Shen and Li, 1996b). Li and Shen (1999) investigated the spray characteristics parameter such as Sauter mean diameter, mean velocity, velocity fluctuation and droplet number density on the same injector. The result indicated that the droplet axial velocity has a jet-like self-similarity.

The main object of this study is to understand characteristics of self-pulsation and reveal the mechanism of this phenomenon. To achieve this purpose injection condition such as gas and liquid momentum, and geometric parameter like recess ratio were used in this study. Laser diagnostics used to measure the spray oscillation frequency. And compared to this result high speed image was also used. From these experimental techniques self-pulsation frequency, spray shape, break-up process and self-pulsation boundary were obtained.

### 3.2. Experimental Apparatus and Methods

The spray patterns were analyzed using instantaneous spray profiles imaged with an indirect photographic technique. The stroboscopic light was illuminated through a translucent paper. A digital camera was used and synchronized with a stroboscopic light that light freeze the spray images. High speed camera was used for capture the change of spray patterns with time. Frame rate of high speed camera is 8000 fps and resolution 256\*512. Using the He-Ne laser (GLG 5350) and photo detector (DET36 A/M), the frequency of spray oscillation were obtained. As shown in Fig. 3.1 laser beam passed through the center of oscillating spray, the laser signal was attenuated until it reached the photo detector. This attenuated signal is linearly proportional to the amount of liquid volume, that signal varied with time. Then using this signal FFT analysis with sampling rate 5000, was applied (see Fig. 3.2) to calculate the frequency of spray oscillation.

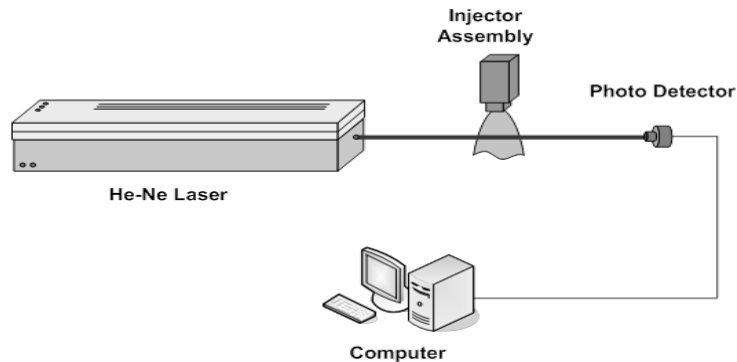


Fig. 3.1 He-Ne laser and photo detector system to measure the frequency of spray oscillation.

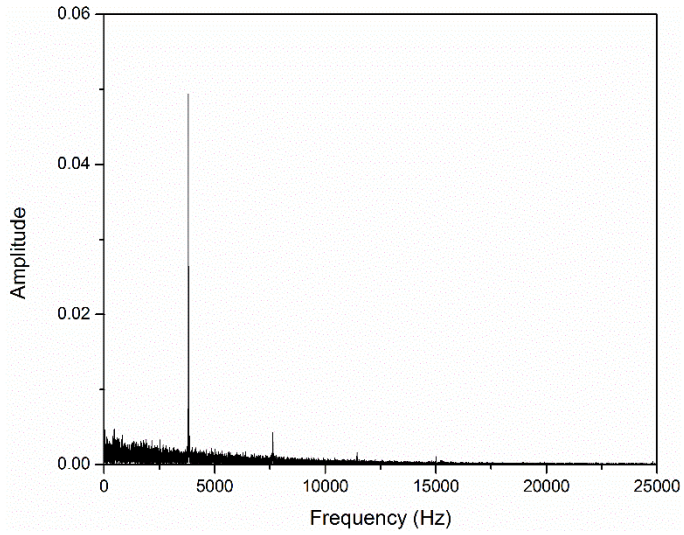


Fig. 3.2. Result of FFT process.

As shown in Fig. 4 gas centered shear coaxial injector was used in this study. It consisted of two parts: the outer oxidizer injector (liquid phase), and the inner fuel injector (gas phase). The inner orifice diameter of gas injector was 3.0 mm. And inner orifice diameter of liquid injector was 4.5 mm. Four entries were located every 90° to produce a uniform liquid supply. Fig. 3 shows the geometric parameters used in this study. Recess is geometrical configuration where the length of inner injector orifice is located from the outer injector face, definition in Eq. (3.1).

$$RR = \frac{L_R}{D} \quad (3.1)$$

The experimental conditions are summarized in Table 3.1 Water and air was used to simulate the sea water (oxidizer) and particle carrier gas (fuel side). The mass flow rate of water was between 15.1~78.4g/s, and a mass flow rate of air was 0.79~3.16g/s, air gas controlled by a mass flow controller. Momentum flux ratio and Reynolds number were experimental parameter of this study. The momentum flux

ratio is the momentum transfer from gas to liquid vice versa, defined Eq. (3.2), that is known to be one of the most important parameters in liquid atomization process (Rehab et al., 1997).

$$J = \frac{\rho_g U_g^2}{\rho_L U_L^2} \quad (3.2)$$

Table 3.1 Experimental conditions.

	Water	Air
$\Delta P$ (MPa)	0.05~1.0	0.008~0.3
Mass flow rate (g/s)	15.1~78.4	0.79~3.16
Reynolds number	4981~22307	18086~55195.2
Momentum flux ratio (J)	0.03~1.5	
Recess ratio (RR)	0, 1.67, 3.34	

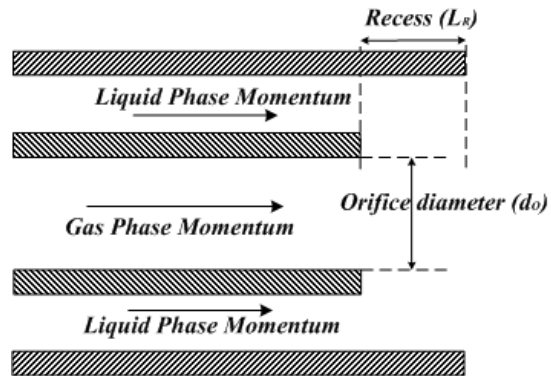


Fig. 3.3 Schematic of geometric parameters.

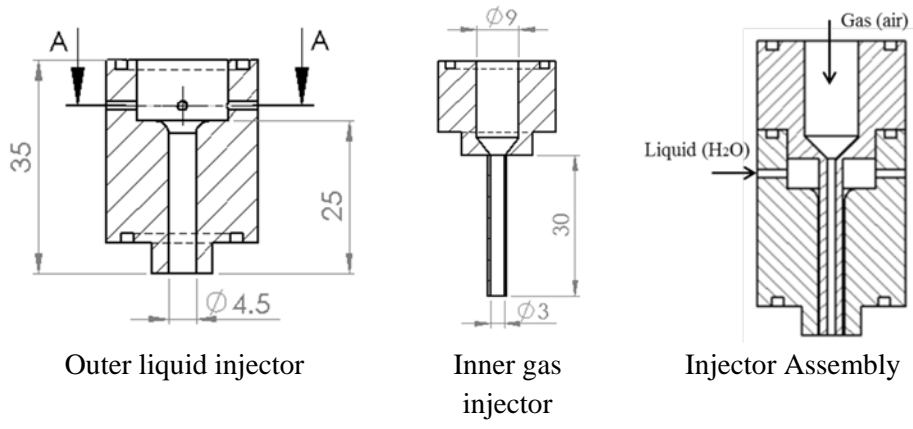


Fig. 3.4 Schematic of a swirl coaxial injector (in millimeters).

### 3.3. Self-pulsation Characteristics

#### 3.3.1 Spray Patterns

Normally self-pulsation phenomenon can effect on the combustion instability, because pressure oscillation by self-pulsation match the pressure oscillation in the combustion chamber, by this process spray oscillation may initiate combustion instabilities. In case of liquid annular jet with self-pulsation region, that effects on spray angle increased than stationary state (Fig. 3.5).

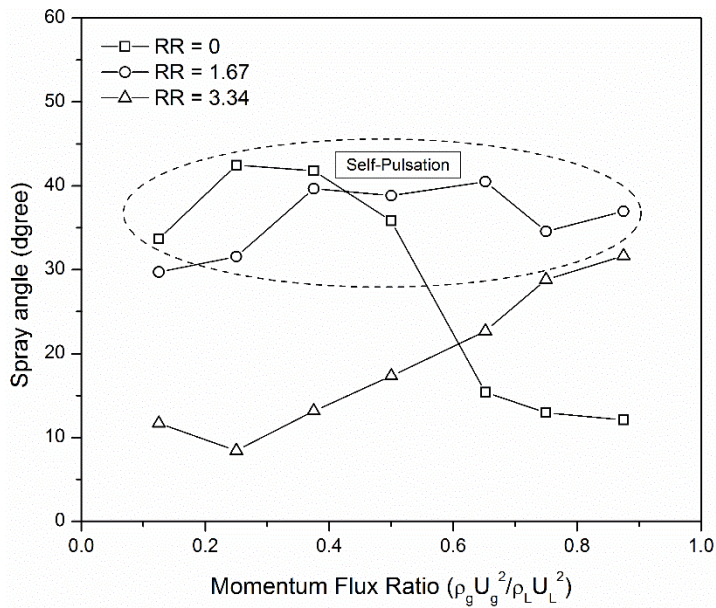


Fig. 3.5 Spray angle at  $Re_L=17,279$ .



(a)



(b)



(c)



(d)

Fig. 3.6 Spray patterns with the gas Reynolds number at  $Re_L=17,279$  and no recess with self-pulsation and no pulsation case: (a) self-pulsation,  $Re_g=23,148$  ( $J = 0.083$ ); (b) self-pulsation,  $Re_g=32,737$  ( $J = 0.167$ ); (c) self-pulsation,  $Re_g=40,094$  ( $J = 0.25$ ); (d) no pulsation,  $Re_g=51,762$  ( $J=0.417$ ).

Figure 3.6 shows that the self-pulsation phenomena at fixed liquid Reynolds number of 17,279 by taking indirect photography and fixed recess ratio of 0. That are suppressed as gas velocity increased. At low gas Reynolds number (Fig. 3.6a~c), strong self-pulsation phenomena were observed but at high Reynolds number Fig. 3.6d), self-pulsation disappeared. When self-pulsation phenomena occurred (Fig. 3.6a~c), observed mass oscillation of the spray and spray angle become larger than stationary spray (Fig. 3.6d).

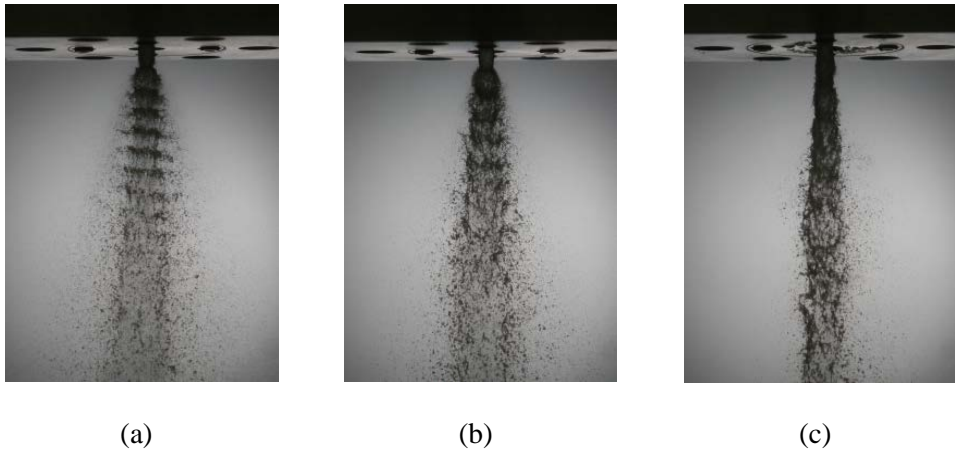


Fig. 3.7 Spray patterns with the recess ratio at  $Re_L=17,279$ ,  $Re_g=23,148$  and  $J=0.083$  with self-pulsation and no pulsation case: (a) self-pulsation,  $RR=0$ ; (b) self-pulsation,  $RR=1.67$ ; (c) no pulsation,  $RR=3.34$ .

To investigate effect of the recess ratio, recess ratio changed from  $RR=0$  to  $RR=3.34$  at the fixed gas and liquid Reynolds number condition. Figure 3.7 shows spray shape according to recess ratio, as you know in Fig. 3.7 as increased recess ratio as decreased self-pulsation frequency. In addition self-pulsation eliminated at recess ratio 3.34. If the inner injector is recessed, then liquid and gas has severe interaction between gas and liquid phased by the outer injector wall.

In this study self-pulsation spray oscillation frequency measured by laser signal

attenuation and FFT analysis. From the measured frequency, there exist two different range, in recess ratio 0 and 1.67 spray oscillation frequency within 2.6~5.0 kHz and at recess ratio 3.34 spray oscillation frequency between 0.6 to 0.8 kHz. To normalize these oscillation frequency, Strouhal number was used. Strouhal number is a dimensionless number describing oscillation flow mechanisms that can be obtained by multiplying geometric average of liquid sheet thickness and center gas radius and dividing gas velocity. It can be presented as eq. 3.3.

$$St = \frac{f\sqrt{hr_g}}{U_g} \quad (3.3)$$

Figure 3.8 shows the Strouhal number which obtained from this study with momentum flux ratio. The order of the Strouhal number at RR=0, 1.67 obtained is in the range of 0.001 to 0.002 and this is the typical value of the liquid sheet instability that is well matched with Lozano's result (Lozano et al., 2005). However at RR=3.34 Strouhal number has almost constant value with momentum flux ratio. These result means spray oscillation of the above two different cases (RR=0 or 1.67, RR=3.34) occurs with different mechanism. From now on recess ratio of injector that used in this experiments, divided by low recess ratio ( $RR \leq 1.67$ ) and high recess ratio ( $RR=3.34$ ). Furthermore investigated spray oscillation characteristics with respect to recess ratio.

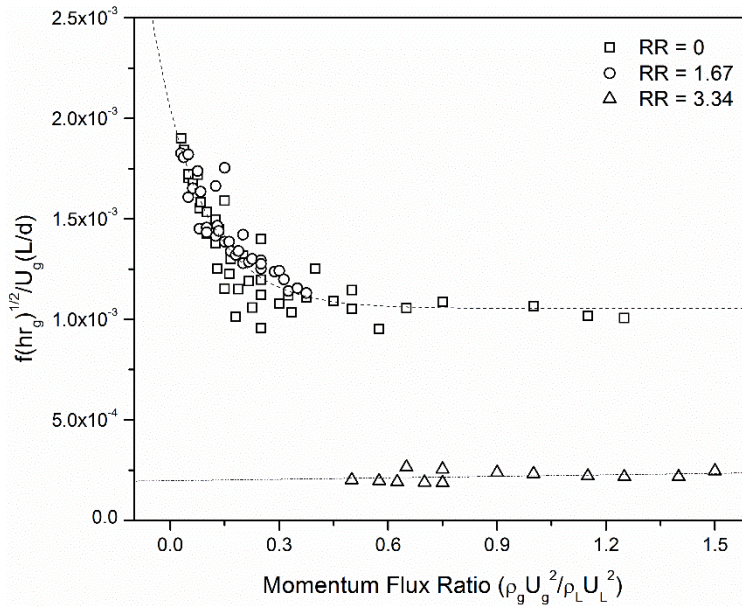


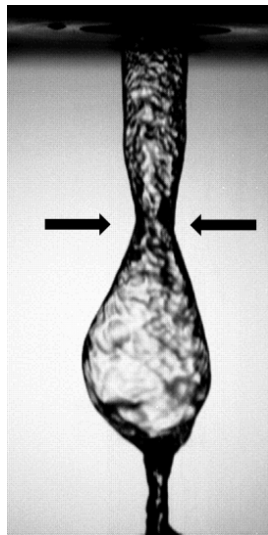
Fig. 3.8 Strouhal number comparing with recess ratio.

### 3.3.2 Low Recess Ratio ( $RR \leq 1.67$ )

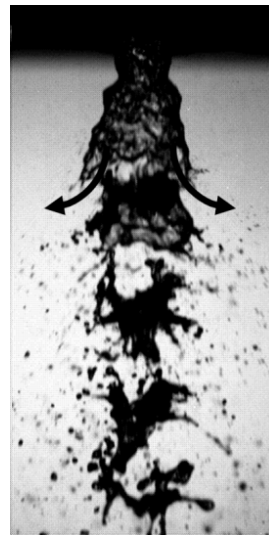
In order to investigate instantaneous image of spray at the orifice exit, high speed camera with the frame rate of camera was 8000fps. The dynamics of pulsation sprays discharging from gas centered shear coaxial injectors in low Reynolds number have been investigated by Kendall (1986) and Wahono et al. (2008). Kendall (1986) reported that a liquid shell formation mechanism, shell formation frequency and shell volume in gas centered shear coaxial injector at low Reynolds number. Kendall argued liquid shell formation frequency increased with gas volume flow rate increased.

As shown in Fig. 9, from the outer injector, liquid ejected from the outside of injector was generated within the hollow core by the downward flow of liquid. Because of surface tension, downward flow of liquid will be decreased gap of the liquid sheet, after that the liquid sheet get together and creates a neck. Accordingly that liquid neck blocked gas flow ejected from the centered orifice, when the gas

flow blocked by the annular liquid column, at momentum of the gas lower than surface tension force of liquid sheets, a radial displacement of the cylindrical surface of the liquid (Fig. 3.9a). After that bulbous liquid feature were made like liquid balloons with gas inside. As the gas Reynolds number increased (Fig. 3.9b), surface tension force of liquid bubble does not resist the pressure of gas, so liquid bubble ruptured, thereby creating spreading liquid ligaments were made (see Fig 3.6a~c). The rupturing process of liquid bubble is the main mechanism of self-pulsation phenomenon of gas centered shear coaxial injector in low recessed case, and that makes a severe noise of the injector.



(a)  $Re_g = 18086,$   
 $\dot{Q}_g = 655.6 \text{ cm}^3/\text{s}$



(b)  $Re_g = 22878,$   
 $\dot{Q}_g = 688.8 \text{ cm}^3/\text{s}$

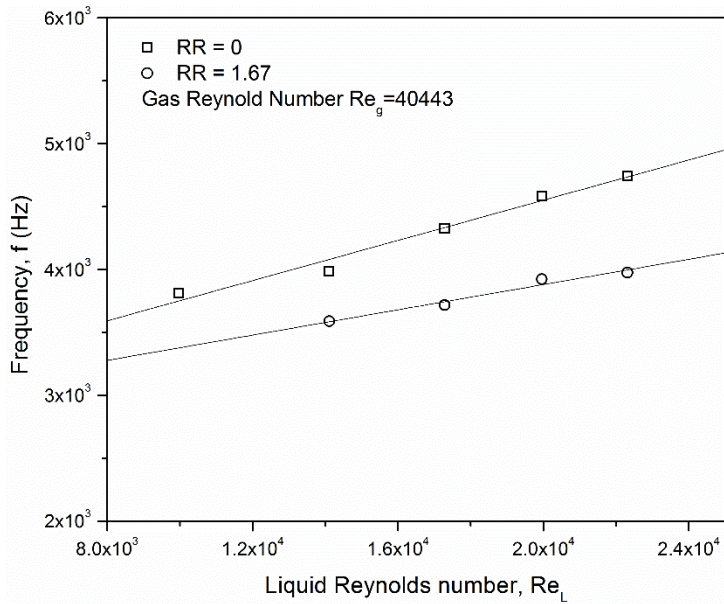
Fig. 3.9 Spray patterns with the gas Reynolds number at  $Re_L=4981,$   
 $\dot{Q}_L=15.13\text{cm}^3/\text{s}$  and  $RR=0$ :

Figure 3.10 shows the characteristics frequencies according to the liquid and gas Reynolds number. Figure 3.10(a) shows a self-pulsation frequency at a constant gas Reynolds number of 40443, as liquid Reynolds number increase as spray

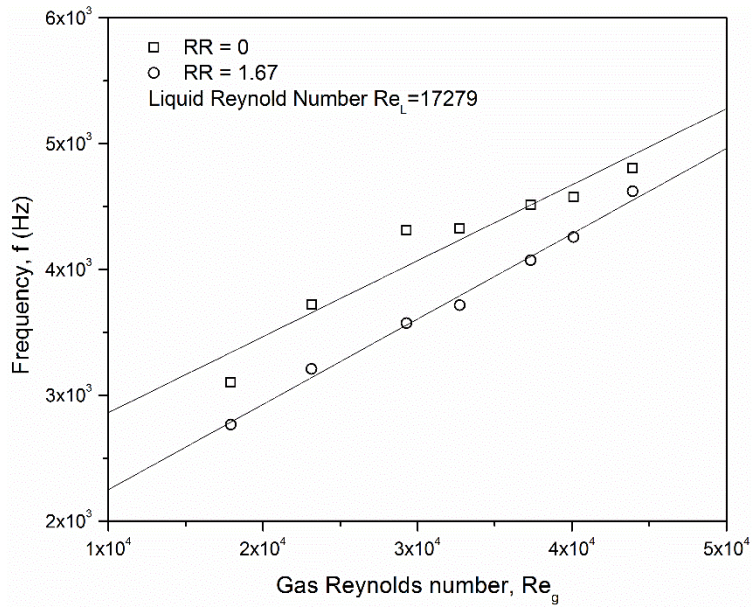
oscillation frequency also increase. However recess number increase 0 to 1.67 self-pulsation frequencies decreased in all experiments case was conducted in this study. Furthermore, Fig. 3.10(b) shows a self-pulsation at a constant liquid Reynolds number of 17279, in this case self-pulsation frequencies linearly proportional to the gas Reynolds number, and also recess number increased, then self-pulsation frequencies decreased.

Kendall (1986) was reported frequencies of produced liquid bubble were linearly proportional to the gas and liquid volume flow rate. Volume flow rate is proportional to the Reynolds number at the same injector geometry. In the previous section of self-pulsation mechanism, this liquid bubble produced process is occur self-pulsation. Therefore result of self-pulsation frequencies from in this study agree with the Kendall's result. Im et al. (2009) studied the pulsation characteristics of sprays from gas-liquid swirl coaxial injector discharging central swirling liquid sheets. The authors observed that the self-pulsation spray frequency is exactly the same as acoustic frequency at the same injection condition. Zhou et al. (1996) observed instability in LOX/H<sub>2</sub> engine may be related to the acoustic oscillation from self-pulsation in coaxial injector from the comparison with some instability tests of liquid rocket engine. From these results, self-pulsation of gas centered shear coaxial injector may be induced combustion instability in underwater propulsion system.

Result from previous section (by indirect photography and laser attenuation method); the onset of self-pulsation associated with the gas and liquid momentum is plotted in Fig. 3.11. As you see in Fig. 3.11 self-pulsation boundary lines plotted inversely with respect of with or without recess. Injector with recess, severe interaction occurred between liquid and gas phase, so in recessed case, the growth of liquid bubble will be limited. Because of this self-pulsation boundary increased with at high liquid momentum flux in recess ratio 1.67 than without recess.



(a) Gas Reynolds number fixed ( $Re_g = 40443$ )



(b) Liquid Reynolds number fixed ( $Re_l = 17279$ )

Fig. 3.10 Characteristic frequency of self-pulsation.

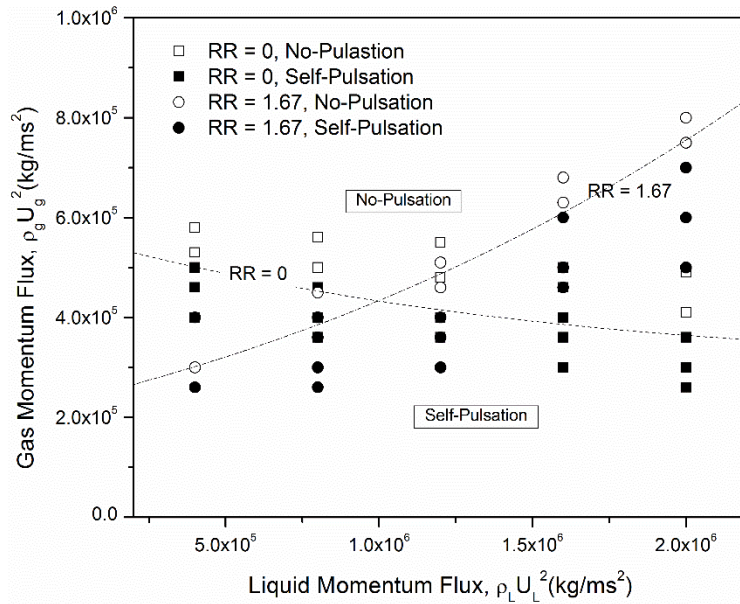


Fig. 3.11 Self-Pulsation Boundary with RR at various momentum flux.

### 3.3.2 High recess ratio (RR=3.34)

In order to investigate spray oscillation mechanism in high recess ratio, inner injector jet width was measured by scattering image from small particle. The Laser sheet (Dual head PIV Nd-YAG Laser, Surelite II-PIV) pass through the center of the injector and scattering signal captured by CCD camera (MegaPlus ES2020) with a 1200 x 1600 size, aluminum oxide (average diameter  $1\mu\text{m}$ ) used as a tracer of gas. In each case, 600 CCD images were acquired to obtain averaged jet width. By this scattering image, measured jet width of the inner injector. Figure 3.12 shows the jet width of the inner injector with respect to the gas Reynolds number according to the downstream from the orifice exit. Inner injector diameter is 3mm and outer injector diameter is 4.5mm used in this study, so as you shown in fig. 3.12, recess ratio greater than 2, inner injector jet width bigger than outer injector diameter. Therefore, in high recess ratio case (RR=3.34) inner gas jet definitely collision to wall of the outer injector (see fig. 3.13), which means gas and liquid phase mixing inside of the outer injector wall. That internal collision and mixing makes a difference spray

oscillation mechanism between low and high recessed case.

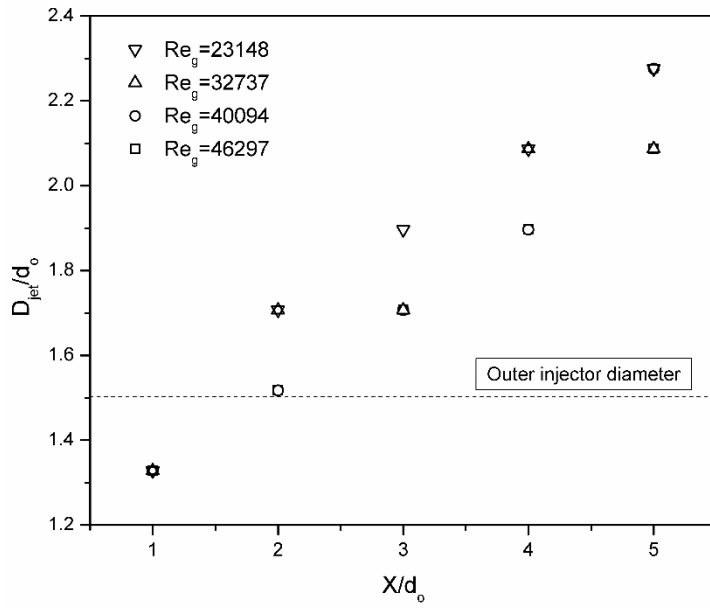


Fig. 3.12 Inner injector jet width

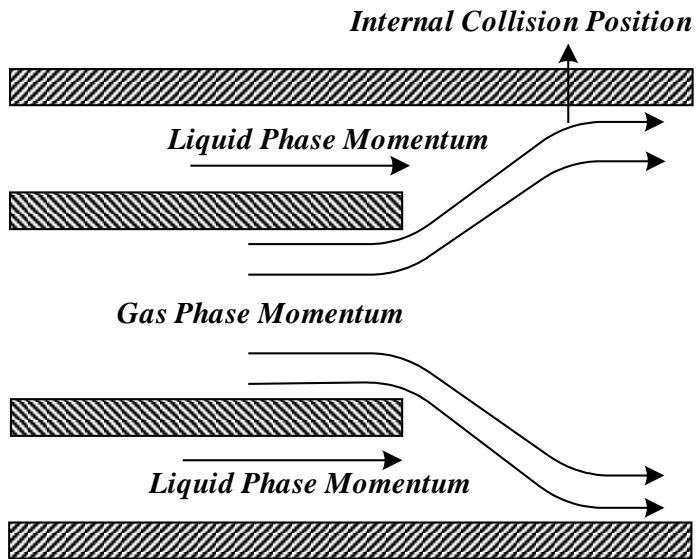


Fig. 3.13 Internal Collision in the high recess,

Figure 3.14 shows the characteristic spray oscillation frequency according to the liquid and gas Reynolds number. As same as low recess ratio, characteristic spray oscillation frequency of high recessed case also increased with respect to the gas Reynolds number increased. However, the mechanism of spray oscillation is different from low recess ratio, because in high recess ratio inner gas collision with outer injector wall, so that gas disturbed movement of liquid sheets and that disturbance makes pulsation of the spray. Therefore, the characteristic spray oscillation frequency increased with the increase of gas Reynolds number. Contrary to the low recessed case, the high recessed case the characteristic spray oscillation frequency decreased with the increase of liquid Reynolds number, since as increase as liquid Reynolds number liquid momentum increased enough to overcome disturbance of the gas momentum.

Result from previous section (by indirect photography and laser attenuation method); the onset of self-pulsation associated with the gas and liquid momentum is plotted in Fig. 3.15. As you see in Fig. 3.15 self-pulsation boundary lines plotted with gas and liquid momentum flux. Contrary to the low recessed case, in the high recessed case, self-pulsation occurs in relatively high momentum flux ratio than low recessed case.

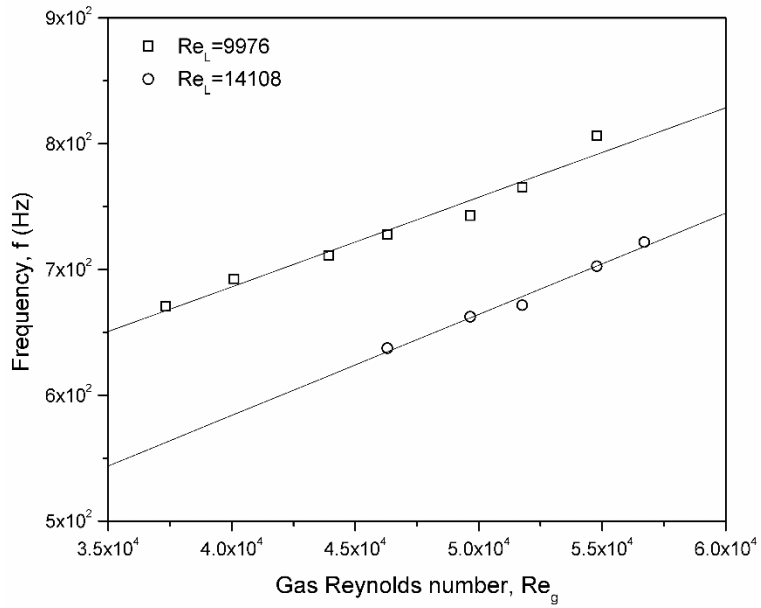


Fig. 3.14 Characteristic frequency of self-pulsation.

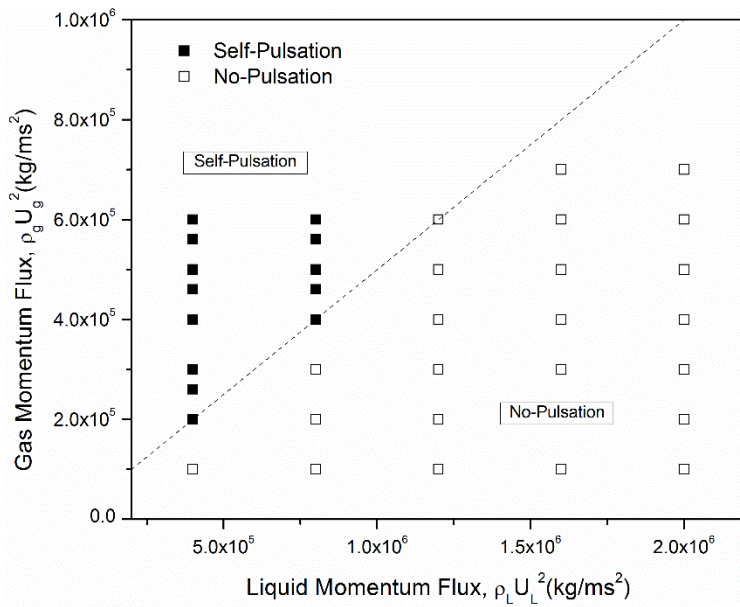


Fig. 3.15 Self-Pulsation Boundary with various momentum flux.

## CHAPTER 4

# SPRAY CHARACTERISTICS OF CARRIER GAS AND PARTICLES IN PARTICLE-LADEN SIMPLE JETS

### 4.1 Background and Objectives

A turbulent gas-particle two-phase flow occurs in many industrial applications, such as pulverized coal combustors, coal gasifiers, chemical reactors, hydro-reactive fuel injectors, and spray injectors. The knowledge of the particle concentration and interaction between a particle and the gas in the multi-phase jets is an important topic, due to its relevance to so many industrial applications. For instance, particle-fluid interaction leads to changes in the level of turbulence intensity.

Various experimental studies have been conducted on fluid characteristics in particle-laden flows. Hardalupas and Horender (2003) measured the mean and rms of fluctuations in particle velocities and the concentration in a turbulent two-phase shear layer. Longmire and Eaton (1992) experimentally investigated the non-evaporating droplet dispersion in a round jet. Their results clearly showed that the particles at the Stokes numbers near unity are largely concentrated in the high-strain rate and low-vorticity regions. An investigation of the fluid-particle interaction has been actively carried out. Modarress et al. (1984) investigated the effect of laden solid particles on the turbulent flow structure with varying particle sizes, jet exit velocities and particle-loading ratios. Gillandt et al. (2001) studied the effects of turbulence modulation by laden solid particles in air flow. Hadinoto and Curtis (2004) examined the mean velocity and turbulence intensity near the nozzle region, as analyzed by the LDV/PDPA system; they then investigated the effect of the particle size and gas-phase Reynolds number. Paik et al. (2011) experimentally investigated the effect of particle-loading and orifice exit velocity on particle dispersion characteristics. Mergheni et al. (2009) studied the effect of solid particles

on the flow characteristics of axisymmetric turbulent coaxial jets. They suggested that a gas characteristic-length scale is insufficient to predict gas-phase turbulence modulation in gas-particle flows.

From the above previous studies, the turbulent modulations of the particle-laden jets have been the subject of many studies but, until very recently, it has been difficult to find in the literature a well-documented study of these scaling properties, including the gas-phase velocity of a particle-laden jet. Melville and Bray (1979) originally conducted the scaling of the centerline velocity  $u_c$  and the half-width  $r_{1/2}$ . They suggested the gas-phase velocity distribution was the function of a dimensionless parameter, such as axial distance ( $x/D$ ), radial distance ( $r/D$ ), Reynolds number ( $Re$ ), particle-loading ratio ( $\phi$ ), and Stokes number ( $Stk$ ). Moreover, they proposed centerline velocity and half-width scales with an exponential factor. After that, Foreman and Nathan (2009) suggested the velocity and half-width scales with a power-law factor. However, these results are applicable only in the fully developed region. Particle-laden flow under the convergent nozzle or short  $L/D$  and high Stokes number particles, gas phase velocity was found to be lower than that of the single-phase flow (Hardalupas et al., 1989, Mergheni et al., 2009, Li et al., 2010). Therefore, for an improved understanding of the scaling properties of a carrier gas in particle-laden jet in the initial jet region and particle itself are necessary.

The experimental study reported here is measuring some basic flow properties such as the particle concentration, mean velocity and fluctuating velocity distribution of turbulent shear jets under varying particle loading ratio and Reynolds number. Than gas phase turbulence modulation and velocity scaling was conducted in the presence of particles. Particle and carrier gas self-similarity characteristics was conducted. In order to achieve this object, turbulent gas-particle flow is studied at a various range of particle loading ratio. PIV/PTV measurements are obtained and analyzed for two size class aluminum oxide particles (1, 42  $\mu m$ ) were added simultaneously to the nozzle. A small particle (1  $\mu m$ ) represented the fluid characteristics of a carrier fluid. Therefore, both particles were captured in the same

frame, so an image processing technique was used for phase separation. For particle detection, images of both the particles and the tracers are separated from the artificial two-phase image by means of the technique employed by Kiger and Pan (2000), Cheng et al. (2010), and Zhang et al. (2008) The results from this study are also used to expand the scaling factor proposed by Foreman and Nathan (2009) through the initial jet region

## 4.2 Experimental Conditions

The experiment setup is shown in Fig. 4.1. Air is used as the carrier gas, and the airflow rate is measured and controlled by a mass flow controller (C100H-DD-4-OV1-V2-V1-S0-C0; Sierra Instruments, USA). Particles of primary size 35–50  $\mu\text{m}$  (Fig. 4.2b) are supplied to the pipeline via a particle feeder using an automated feeding screw. To determine the orifice exit velocity, tracer particles with a primary size of 0.5–2  $\mu\text{m}$  (Fig. 4.2a) are respectively provided to the pipeline by a tracer feeder. The terminal velocity and relaxation time are calculated from respectively (Rhodes, 2008),

$$u_t = \left[ \frac{4gd_s(\rho_s - \rho_f)}{3\rho_f C_{D0}} \right]^{0.5} \quad (4.1)$$

$$\tau_s = \frac{\rho_s d_s^2}{18\mu} \quad (4.2)$$

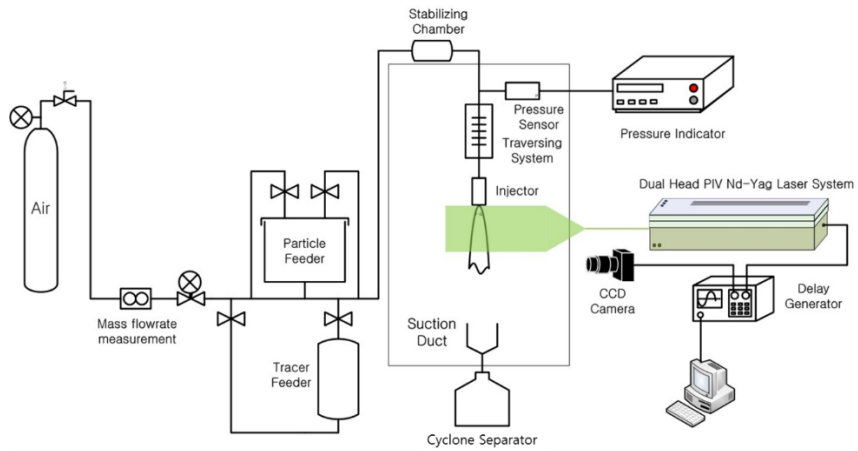


Fig. 4.1 Experimental apparatus.

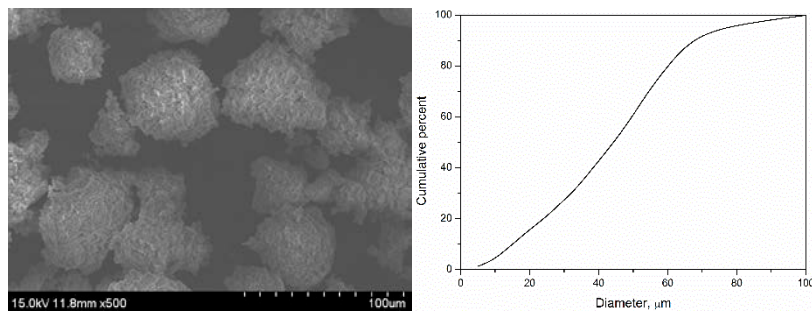
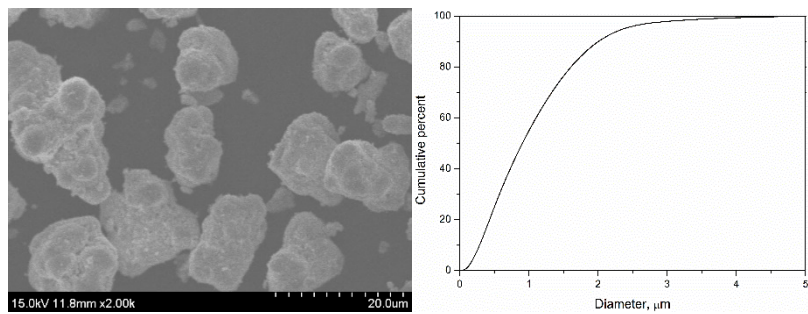


Fig. 4.2 Cumulative particle diameter. (a) Mean diameter 1  $\mu\text{m}$ , (b) Mean diameter 42  $\mu\text{m}$

Table 4.2. Properties of the particles.

	Tracer	Particle
Mean diameter, $d$ ( $\mu\text{m}$ )	1	42.5
Standard deviation for the diameter, $\sigma$ ( $\mu\text{m}$ )	0.75	19.9
Density, $\rho$ ( $\text{g}/\text{cm}^3$ )	3.97	3.97
Terminal velocity, $u_t$ ( $\text{ms}^{-1}$ )	0.00012	1.25
Relaxation time $\tau_s$ (ms)	0.012	20.9

Table 4.1 summarizes the properties of the tracer and particle. The terminal velocity and relaxation time for tracer particle is very small, showing good ability in the air suspension and in following the airflows. The experimental chamber is sealed with transparent polycarbonate covers with the ceiling open, and the chamber has a  $1,000 \text{ mm} \times 1,000 \text{ mm} \times 1,500 \text{ mm}$ . The axial distance from the jet exit to the downstream end of the chamber was 1000 mm, while the distance from the center of the jet to the sidewalls of chamber was 500 mm. The maximum full width of the jet was approximately 25 mm at the end of measurement section that makes the free from wall effects within the working region. A PIV measurement is used to measure the air and particle velocities. The particle laden flow transitions from a horizontal section of pipe through a  $90^\circ$  bend to the vertical nozzle with a length to diameter ratio of 150. This long pipe in order to redistribute the particles after the bend and 150 nozzle diameters are found to be adequate to obtain fully developed flow. The convergent nozzle has a contraction ratio of 5.06 with an exit diameter of 4 mm. A honeycomb straightener is located at the top of the test chamber to allow for the free entrainment of air from the surroundings by the expanding jet. Fans are placed at the cyclone separator to create a favorable pressure drop at a maximum velocity of

0.2 m/s that drives the particles out of the test rig to a cyclone separator.

The laser system used in the experiment is a dual head PIV Nd-YAG laser (Surelite II-PIV). A pulsed laser sheet beam with a 10 Hz pulse frequency, made by a digital pulse generator (DG535; Stanford Research Systems, Sunnyvale, California, USA) and optical lenses, is passed vertically through the jet center, and particle scattering images are captured by a CCD camera (VH-2MC-M42; Vieworks, Korea) with a  $1,200 \times 1,600$  pixel. . Each case, 300 pairs of CCD images are acquired to obtain the averaged velocity vector fields. For the CCD image processing, a commercial PIV code is used (TSI: insight 3G). Field of view of this experiments is 31.5 mm (width)  $\times$  42 mm (height). This study PIV images was captured from two different position, region I axial imaging extent 0 mm – 42 mm, region II axial imaging extent 38 mm – 80 mm. The axial imaging extent was measured from the jet exit.

The particle feeder is designed to supply constant particle mass flow rates. A cone structure inside the particle feeder is sealed with a polycarbonate cover and pressurized to the same pressure using a tube where the air passes through to prevent a backward flow of particles. A screw, which is put inside the particle feeder, is rotated by an AC variable speed motor attached to an end of the screw. When the screw spins, the particles loaded between the screw's pitch are transported to an airline. The particles fluidized by the air are then sprayed through the injector orifice.

The particle-loading ratio  $\phi$ , is defined as the ratio of the total solid mass flow rate to the mass flow rate of the air jet at the nozzle exit ( $\frac{\dot{m}_p}{\dot{m}_f}$ ). In the present work, the particle-laden flow experiment is conducted in the two-way coupling region. The exit Stokes number  $Stk_0$ , which is defined as the ratio of the particle response time to the fluid response time, characterizes the responsiveness of the particles to the fluid-phase turbulent fluctuations (Hardalupas et al., 1989).

$$Stk_0 = \frac{\tau_p}{\tau_f} = \frac{\rho_p d_p^2 U}{18\mu D} \quad (4.3)$$

Table 4.2 Experimental conditions.

Case	$d_s$ ( $\mu\text{m}$ )	$St_T$	$Re_0$ ( $\times 10^4$ )	$\phi$
Case 1	42.5	423.3	2.04	0.135
Case 2	42.5	423.3	2.04	0.188
Case 3	42.5	423.3	2.04	0.288
Case 4	42.5	515.7	2.49	0.096
Case 5	42.5	515.7	2.49	0.134
Case 6	42.5	515.7	2.49	0.205
Case 7	42.5	683.2	3.29	0.075
Case 8	42.5	683.2	3.29	0.104
Case 9	42.5	683.2	3.29	0.159

Particles are usually classified into three regimes:  $Stk_0 > 1$  ('unresponsive'),  $Stk_0 \sim 1$  ('partially responsive'), and  $Stk_0 < 1$  ('responsive'). The  $Stk_0$  values for the 42- $\mu\text{m}$  aluminum oxide are between 423.3 and 683.2, which indicates that the particles are unresponsive to the fluid motion and these particles are governed by particle–particle collisions. Moreover, the  $Re_p$  of the obtained data is significantly less than 400; therefore, the vortex shedding phenomenon does not affect the turbulence modulation (Hetsroni, 1989).

$$Re_p = \frac{\rho_f |u_f - u_p| d_p}{\mu} \quad (4.4)$$

Where  $u_f$  is the fluid velocity,  $u_p$  is the particle velocity, and the  $\rho_f$  is the fluid density. A summary of the experimental data is provided in Table 4.2.

## 4.3 Fluidic Characteristics of Particle and Carrier Gas

### 4.3.1 Mean Velocity Characteristics

In this section, measurements of the mean velocities and velocity fluctuation of the gas and particle phase, normalized by the single-phase centerline velocity  $U_0$ , are reported and analysed. Figure 4.3 shows the normalized mean axial velocity distribution along the axial distance from the nozzle exit to  $x/D = 10$  in single- and two-phase flows for the  $\Phi=0.288$ . The radial distribution of the two-phase gas velocity was lower than the single-phase in the initial jet region ( $x/D < 5$ ). However, in the fully developed region, the two-phase gas velocity was slightly greater than the single-phase. Figure 8 shows the axial profiles of the central jet mean velocity  $U_c$  normalized by the jet exit velocity  $U_0$  for the single-phase, two-phase, and particle-phase jets. In this experiment, the particle-laden jet showed the particle-developing region ( $x/d < 5$ ), which is defined as a zone from the orifice exit to the point where the particle velocity reaches the maximum, as shown in Fig. 4.4. If the Stokes number is much greater than one and acceleration length of the nozzle was short, the particles are unable to reach the fluid phase exit velocity due to their inertia, so the particle-developing region appears. Past the particle-developing region ( $x/D > 5$ ), the particle velocity dwindles, and the region particle velocity is greater than that of the gas phase. This region the centerline decay rate of the particle was observed lower than the fluid phase velocity decay rate.

As shown in Fig. 4.4, the gas-phase velocity in the developing region is lower than the single-phase velocity with increase of particle loading ratio. This is due to the particles entering inside the injector nozzle at a velocity lower than the local gas flow. In order to create a momentum exchange between the particle and local gas flow, particles were accelerated through the injector section and the gas phase was decelerated, resulting in a lower velocity at the injector exit. This velocity was decreased with increases in the particle-loading ratio. Beyond the developing region, due to the momentum exchange from particle to fluid, the gas-phase velocity decay rate is less than the case of a single-phase flow and that decreased with increases in the particle-loading ratio.

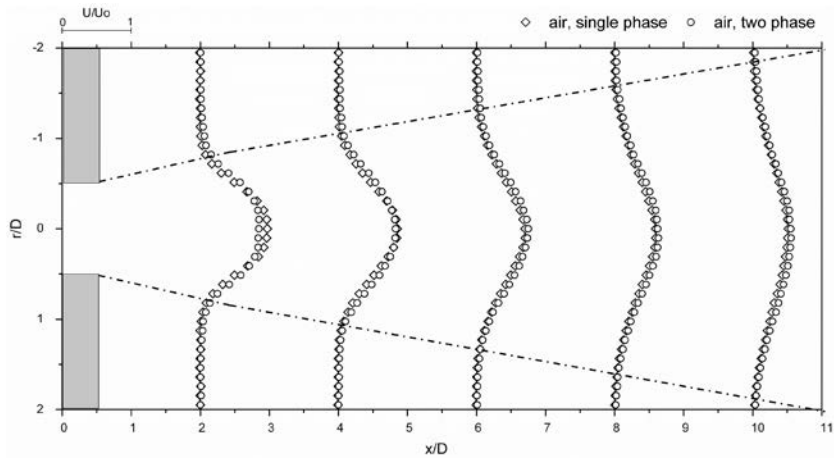


Fig. 4.3 Mean axial velocity distribution of single- and two-phase flows.

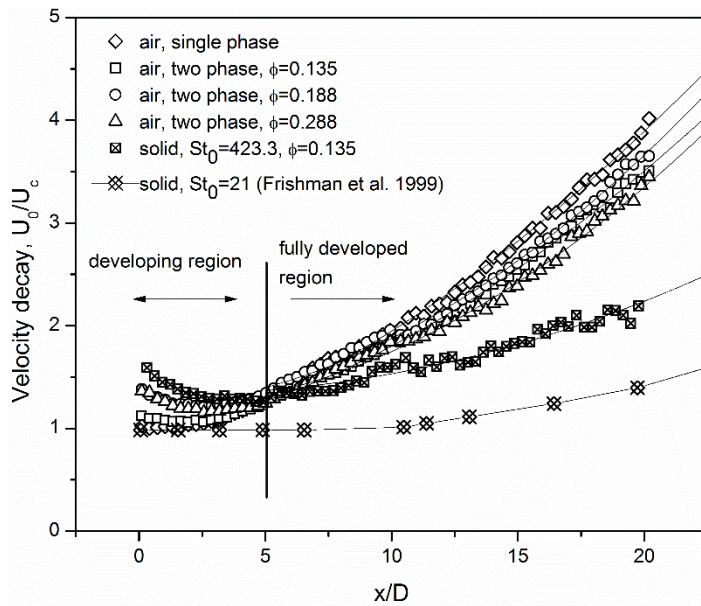
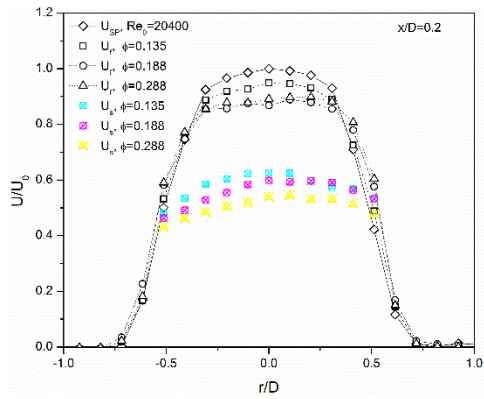


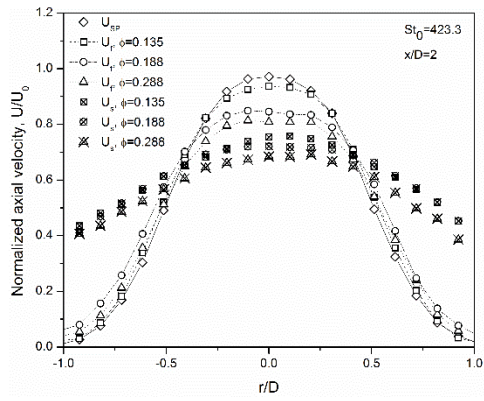
Fig. 4.4 Axial profiles of mean velocities of single-phase, two-phase, and solid particles.

Figure 4.5 shows the radial velocity profiles before and after the developing region. Fig. 4.5(a) show the effect of exit Reynolds number on gas phase and particle at nozzle exit  $x/D=0.2$ . The nozzle exit region particle velocity decreases as

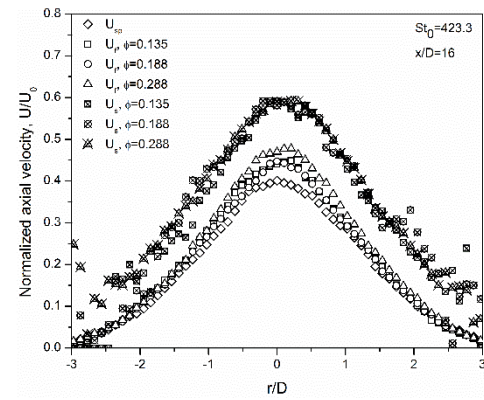
Reynolds number increased. This was due to the particle was less responses to the change of gas velocity with increase Reynolds number. Therefore, particles were less accelerated than low Reynolds number case trough the injector section. Fig. 4.5 (b) show a radial velocity profile of the developing region. As described in the previous section, in the center of the jet ( $r/D < 0.4$ ), the single-phase velocity is greater compared to the two-phase velocity with increases in the particle-loading ratio. In that region, the particle velocity was also greater than the gas-phase velocity, and it was lower than the gas-phase velocity at  $r/D > 0.4$ . Further downstream (e.g.,  $x/D > 5$ ) (Fig. 4.5[c]), as shown in Fig. 4.4, the velocity of the two-phase jet is larger than that of the single-phase with increases in the particle-loading ratio. Due to the momentum exchange from the particles to the fluid, the velocity of the gas phase in two-phase jet is higher than that of the single-phase jet. Regarding the velocities of the particles in all areas, it can be seen that they are larger than the velocity of the gas phase, due to the mass inertia of the particles.



(a)



(b)



(c)

Fig. 4.5 Radial profiles of axial mean velocities effect of exit Reynolds number, effect of particle loading ratio in  $Re_0=20400$  (a)  $x/D=0.2$ , (b)  $x/D=2$ , (c)  $x/D=16$

### 4.3.2 Similarity Characteristics of Particle and Carrier Gas

A Jet is a high velocity flow of steam, liquid or gas expelled from a small hole such as a nozzle into quiescent surroundings. Because a jet grows and develops, interacting with environmental fluid, it gradually loses its initial characteristics, such as nozzle shape, nozzle diameter and exit velocity profile, except for its momentum. A jet is composed of three parts, categorized by their rate of development, as represented in figure 4.6. That are the initial development region, the transition region and the fully development region. The initial development region consist of a potential core and a region of mixing, in the mixing region, expelled jet material interacts actively with the surroundings and loses its initial characteristics. In the potential core, on the other hand, the initial characteristics of the jet are maintained. Turbulence intensity in the mixing region is relatively higher than that in the potential core. The center axis of the jet in the potential core is the highest velocity parts of the jet because interaction between the jet and surrounding medium begins from the jet boundary. From the downstream edge of the potential core, the velocity of the center axis starts to decrease and the transition region begins. In the transition region, the jet is in preparatory stage before achieving a state of equilibrium. After sufficient development of the jet in the transition region, the get reaches the fully developed region in which many turbulent properties are stable. The fully developed region I also referred to as the self-similarity region because most properties of the jet can be expressed as similar profiles at different distances from the nozzle exit.

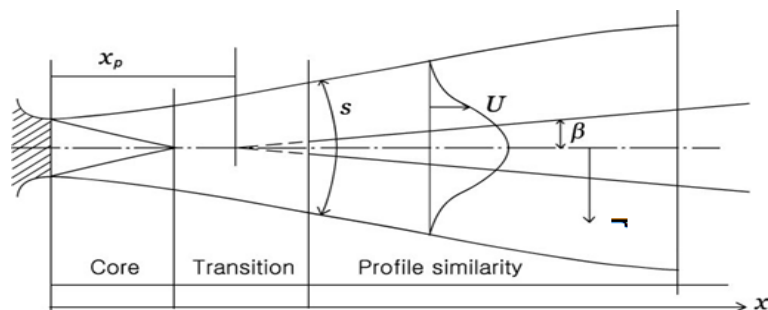


Fig. 4.6 Structure of jet.

Malmström et al. (1997) studied effect of exit velocity and nozzle diameter on centerline velocity decay. According to Malmström et al. (1997) average velocity to the radial direction and centerline velocity decay can be expressed as following Gaussian distribution function when maintained self-similarity.

$$\frac{U}{U_c} = \exp(-K_u n^2) \quad (4.5)$$

$$\frac{U_0}{U_c} = \frac{1}{B_u} \left( \frac{x}{d} - \frac{x_p}{d} \right) \quad (4.6)$$

( $U_c$  : centerline velocity,  $n : \frac{r}{x-x_p}$ ,  $x_p$  : virtual origin,  $K_u$  : self-similarity coefficient,  $B_u$  : velocity decay coefficient)

Table 4.3 Experimental conditions.

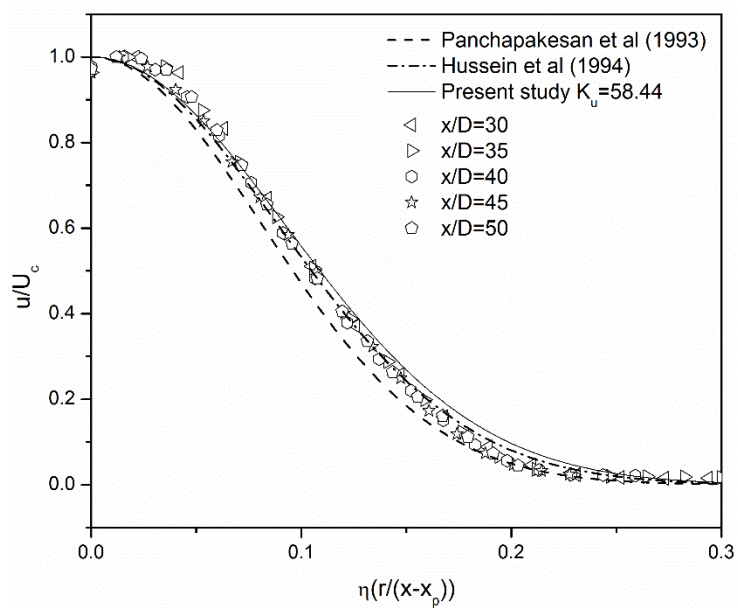
Air flow rate (g/s)	1.184, 1.579, 1.973, 2.368
Particle feeding rate (g/s)	0.137 ~ 0.664
Orifice diameter (mm)	2.5, 3.0, 3.5
Orifice length (mm)	10,20,30
Nd-YAG Laser pulse freq. (Hz)	10
Beam delay ( $\mu$ s)	4
Particle and Tracer density (g/cm <sup>3</sup> )	Al <sub>2</sub> O <sub>3</sub> , 3.97
Particle primary diameter ( $\mu$ m)	35 ~ 50
Tracer primary diameter ( $\mu$ m)	0.5 ~ 2

Therefore, if particle and flow has a self-similar condition characteristics such as velocity, turbulence intensity, Reynolds stress and particle number density distribution, these properties can be expressed as equation 4.5 and 4.6. Particle and flow characteristics at the specific point can be predicted when, self-similarity coefficient ( $K_u$ ) and velocity decay coefficient ( $B_u$ ) knows. Investigation of effect of particle on self-similarity in particle-laden flow was conducted. Table 4.3 shows

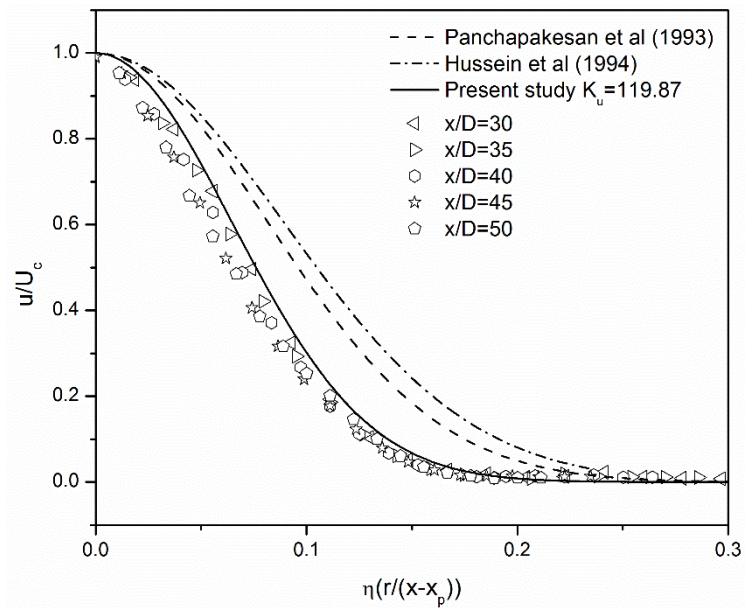
the experimental condition, as shown in table 4.3, air flow rate was changed with four different case, and particle loading rate was changed from 0.137 to 0.664. Aluminum oxide was used for fuel particle (42  $\mu\text{m}$ ) and tracers (1  $\mu\text{m}$ ).

Fig 4.7 shows the similarity of pure air jet and particle-laden jet at  $x/d$  30-50. In case of pure air jet has a good agreement with previous results after  $x/d=30$  (Panchapakesan and Lumley, 1993, Hussein et al., 1994). The half-width for the jet can be used to determine the representation of the mean velocity profile in the equation 4.5. This gives a value of  $K_u=58.44$  (Hussein  $K_u=63$ , Panchapakesan  $K_u=75$ ). And in case of particle-laden jet the all of experiments results of particle flows are collapsed a single line (Fig. 4.7), that also exist self-similarity but because of the inertia of particle, particle does not dispersed radial direction, so distribution of particle is narrow than pure air flow (particle :  $K_u=119.87$ , air :  $K_u=58.44$ ).

Fig 4.8 shows effect of particle loading ratio and orifice exit velocity on the similarity of particle-laden jet. Particle loading ratio influence interactions between the particles and the gas phase and the gas phase turbulence modulation in a particle-laden flow, that defined as the ratio of the particle mass flow rate to the gas mass flow rate ( $\Phi = \frac{m_p}{m_f}$ ). Fig 4.8 shows effect of particle loading ratio and effect of orifice exit velocity respectively, both case mean velocity profile of particle shows self-similarity. These results agreed with similarity hypothesis that suggested by Schilchiing in particle-laden flow regardless of initial condition particle loading ratio and orifice exit velocity.

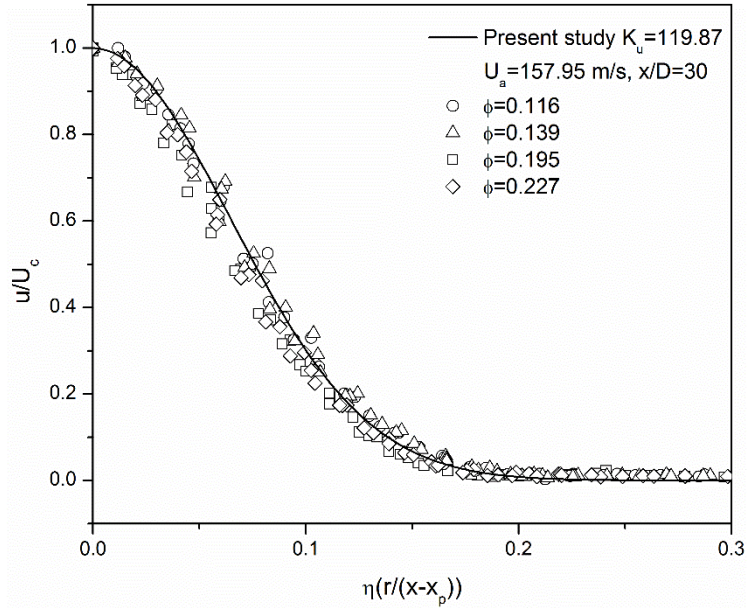


(a) Air mean velocity

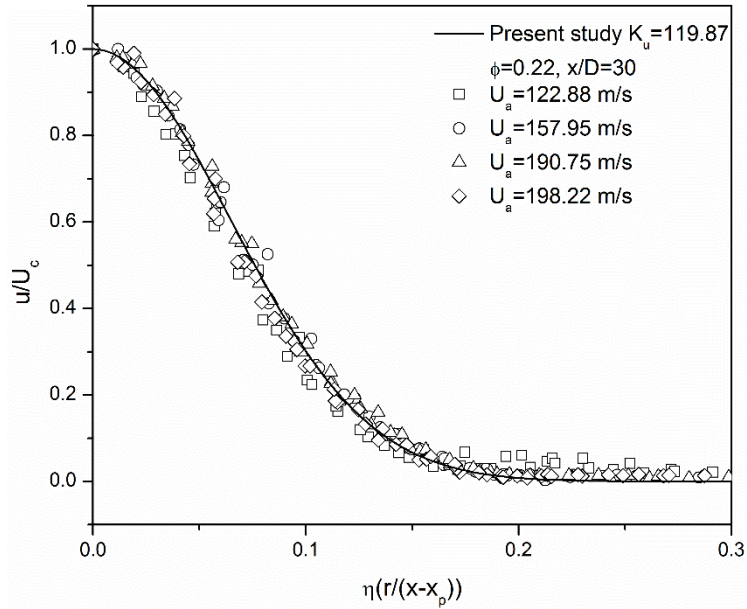


(b) Particle mean velocity

Fig. 4.7 Mean velocity distribution ( $U_0=152.8$  m/s,  $L_0=30$ mm).



(a) Effect of particle loading ratio



(b) Effect of orifice exit velocity

Fig. 4.8 Particle mean velocity profile across the jet ( $L_o=20\text{mm}$ ,  $D=3.5\text{mm}$ ).

### 4.3.3 Similarity of Particle Number Density

Particle number density greatly effect on the carrier gas turbulent structure. So investigation on the particle number density profile is needed (Gillandt et al., 2001). Therefore, spanwise distribution of particle number density was investigated. Particle number density measured from after phase discriminated image by counting its number in sub interrogation window (32 x 32 pixels) with 50% overlap. Particle number density similarity function was obtained by modify velocity similarity equation as below.

$$\frac{N}{N_c} = \exp(-K_u n^2) \quad (4.7)$$

( $N_c$  : centerline particle number density,  $n$  :  $\frac{r}{x-x_p}$ ,  $x_p$  : virtual origin,  $K_u$  : self-similarity coefficient)

Figure 4.10 shows the particle number density distribution with spanwise direction, it also shows self-similarity like velocity distribution. Unlike the velocity distribution it shows a self-similar distribution after  $x/d=10$ , because as shown in the fig. 4.9, in the potential core region mixing with particle and outer gas vigorously take place. The value of self-similarity coefficient  $K_u$  is 184.6 in this case, so it's narrower than gas velocity distribution and particle velocity distribution due to the particle motion dominate by inertial force. The  $St_0$  values for the 42- $\mu$ m aluminum oxide is 660, which indicates that the particles are unresponsive to the fluid motion and these particles are governed by inertia force.

$$St_0 = \frac{\tau_p}{\tau_f} = \frac{\rho_p d_p^2 U}{18\mu D} \quad (4.8)$$

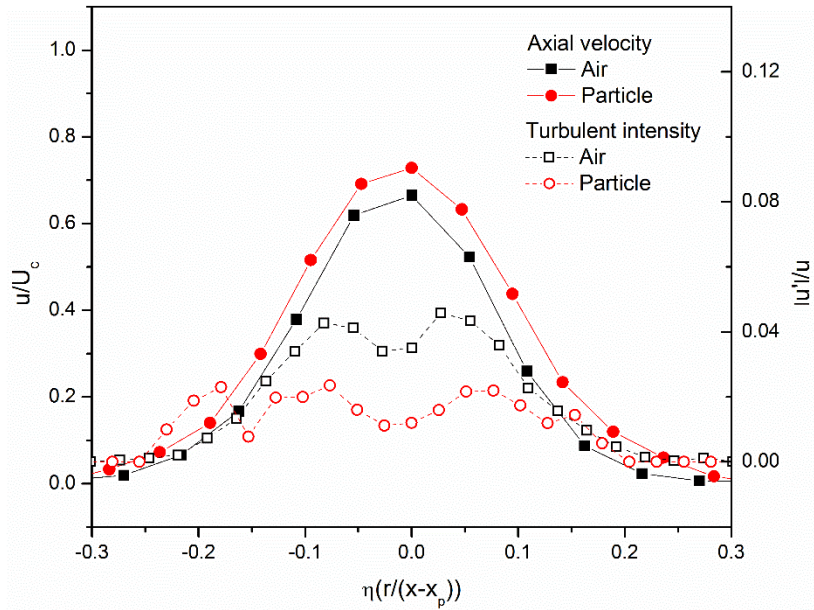


Fig. 4.9 Velocity and turbulence intensity distribution at  $x/D=10$ .

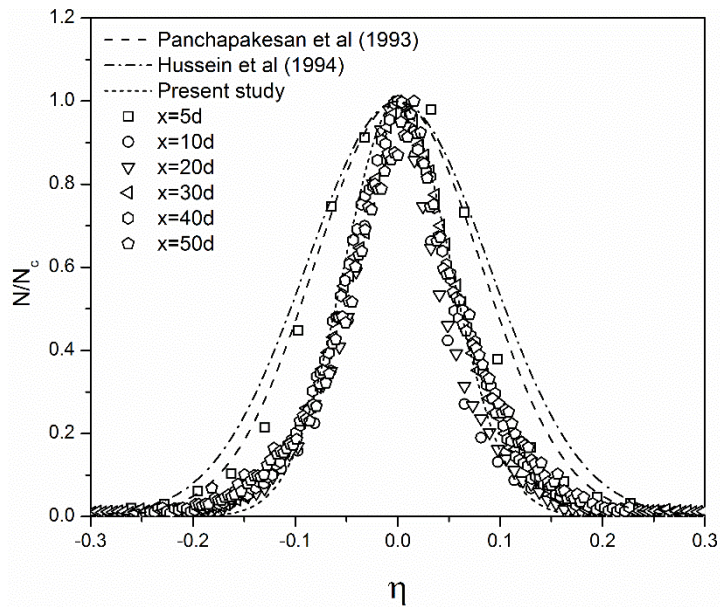


Fig. 4.10 Particle number density profile.

Figure 4.11 shows the effect of orifice length on the particle distribution. Gore and Crowe (1989) found that the particle motion governed by inertial force and particle-particle interaction when particle diameter is large ( $d_p/D > 0.1$  this study:  $d_p/D > 0.14$ ). In that condition, orifice length also effect on the particle distribution due to as orifice length increases particle-particle interaction more vigorous in the inside of orifice. However, particle number density agreed with self-similarity with respect to the orifice length variation.

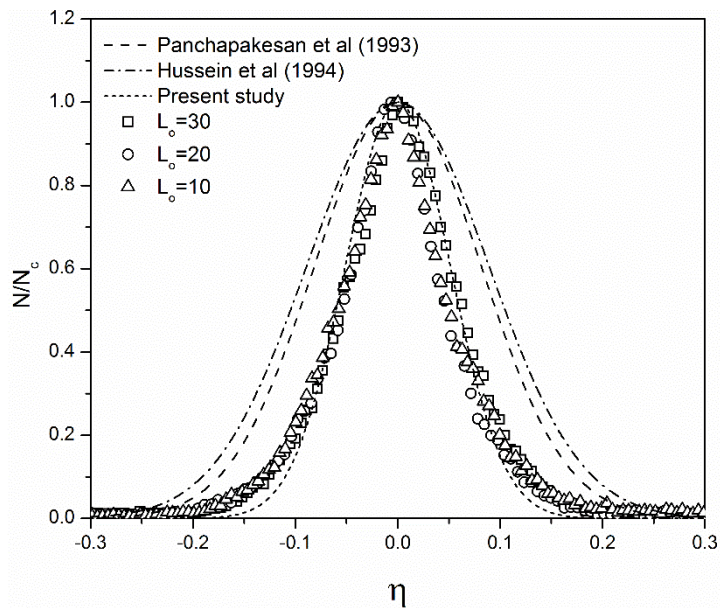


Fig. 4.11 Particle number density profile according to orifice length.

## 4.4 Scaling of the Centerline Velocity Decay

### 4.4.1 Centerline Velocity Decay of Gas Phase

From the previous section, particle loading ratio and Stokes number significantly effects on gas phase velocity and turbulence in initial jet region was studied. In the initial jet region, as particle loading ratio increases, the centerline velocity lower than the single phase flow and turbulence enhanced with increase of mean slip velocity.

Melville and Bray (1979) previously conducted scaling of the centerline velocity  $u_c$ ; they began their analysis of the gas-phase distribution in a particle-laden jet as a function of dimensionless parameter, like Eq. 4.9.

$$\frac{U}{U_0} = f\left(\frac{x}{D}, \frac{r}{D}, Re, \phi_0, Stk_o\right) \quad (4.9)$$

They neglect both the Reynolds and Stokes number effects, because the velocity field is sensibly independent of the Reynolds number; for a sufficiently large  $Re$ , they also expect that if  $\tau_p$  is small enough with respect to the time characteristics of the energetic turbulence scales  $\tau_f$ , the mean velocity field will be independent of the Stokes number. With these consumptions, the centerline velocity is written as

$$\frac{U_0}{U_c} = f\left(\frac{x}{D}, \phi\right) \quad (4.10)$$

They propose the above functions as an exponential correlation, giving

$$\frac{U_0}{U_c} = K_1 \frac{x}{D} e^{-0.69\phi_0} \quad (4.11)$$

In addition, Foreman and Nathan (2009) reported the centerline velocity may alternately be scaled with power-law functions, and they identified the centerline

velocity with three regimes (i.e.,  $St_0 \leq 20$ ,  $20 \leq St_0 \leq 200$ ,  $200 \leq St_0$ ). However, these results are only applicable in the fully developed region. From Melville and Bray (1979) hypothesis described above, the effect of the Stokes number is ignored when it is very small, but if the injection conditions of the Stokes number are high enough, it is no longer ignored at the end of the nozzle. This hypothesis can be confirmed from the result in Fig. 4.12(a), where the velocity difference between the two-phase jet and the single-phase jet, together with the momentum transfer, is significantly affected by the Stokes number variation. The result of the Stokes number effect in this paper is in agreement with Hadinoto et al. (2005), Mergheni et al. (2009), and Hardalupas et al. (1989). Therefore, in the initial jet region, the Stokes number effect has also been considered. The above result demonstrated that the gas-phase velocity is affected by the Stokes number, and we called these gas velocity changes, with respect to the single-phase flow, changes in gas-phase velocity (CGV). Then, centerline velocity is expressed as a function of the axial distance ( $x/D$ ), the initial particle-loading ratio ( $\phi_0$ ), and the CGV ( $\frac{U_{SP}-U_{TP}}{U_{SP}}$ ). With these hypotheses, the centerline velocity is expressed as follows:

$$\frac{U}{U_0} = f\left(\frac{x}{D}, \phi_0, \frac{U_{SP}-U_{TP}}{U_{SP}}\right) \quad (4.12)$$

With this, in the initial jet region ( $x / D < 5$ ),  $U_c$  may be scaled with the following function, where

$$\frac{U_0}{U_c} = \left(1 + \left(\frac{U_{SP}-U_{TP}}{U_{sp}}\right)\right)^{1+\phi} \left(1 + \frac{x}{D}\right)^{(-0.7 \times \phi)} f\left(\frac{x}{D}\right) \quad (4.13)$$

Consequently, in the initial region, applying Eq. 4.13, the axial velocities of the two-phase flow and the single-phase flow collapsed all experimental data into a single line, as shown in Fig. 4.12 (b). As shown in Fig 4.13, by using this equation,

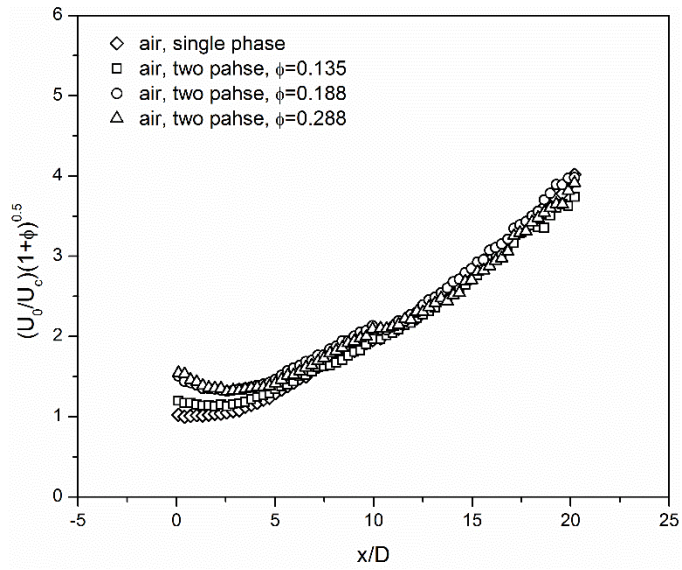
even when the Reynolds number of the nozzle exit is different, it shows an axial velocity of single- and two-phase flows, combined as three separate lines with respect to the Reynolds number. In addition, as can be seen from the results of Malmström et al. (1997), the velocity decay coefficient ( $K$ ) in the development area of the jet in each condition was different, which decreased with increases in the nozzle outlet velocity.

Finally, by using the correlation equation obtained in this paper, Fig. 4.14 shows the correlation between the axial velocity of the single-phase flow and the two-phase flow. The strength of this correlation equation between the single- and two-phase is assessed by the correlation coefficient, defined as

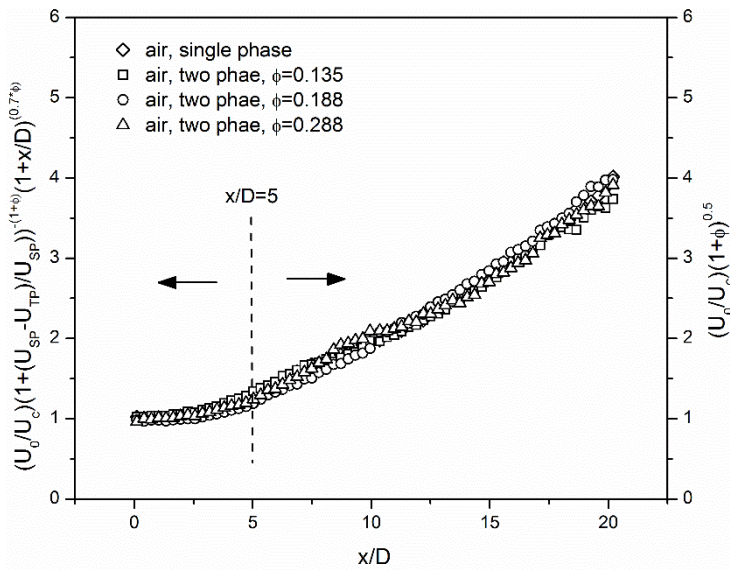
$$R^2 = 1 - \frac{SS_{res}}{SS_{tot}} = 1 - \frac{\sum_i (u_{SP,i} - u_{TP,i})^2}{\sum_i (u_{SP,i} - \bar{u}_{SP})^2} \quad (4.14)$$

Where  $SS_{tot}$  represents the total sum of the squares and  $SS_{res}$  represents the sum of the squares of the residuals.

Importantly, the correlation coefficient based on this study was 0.986 and it was 0.980 for Foreman et al. regarding of the correlation coefficients in the entire region, there are no significant differences among them. However, in the initial jet region ( $x/D < 0.5$ ), the correlation coefficient result of this paper ( $R^2 = 0.809$ ) is in good agreement with Foreman et al. ( $R^2 = 0.434$ ).



(a)



(b)

Fig. 4.12 Gas phase centerline velocity, as reported by (a) Foreman et al., (b) this study.

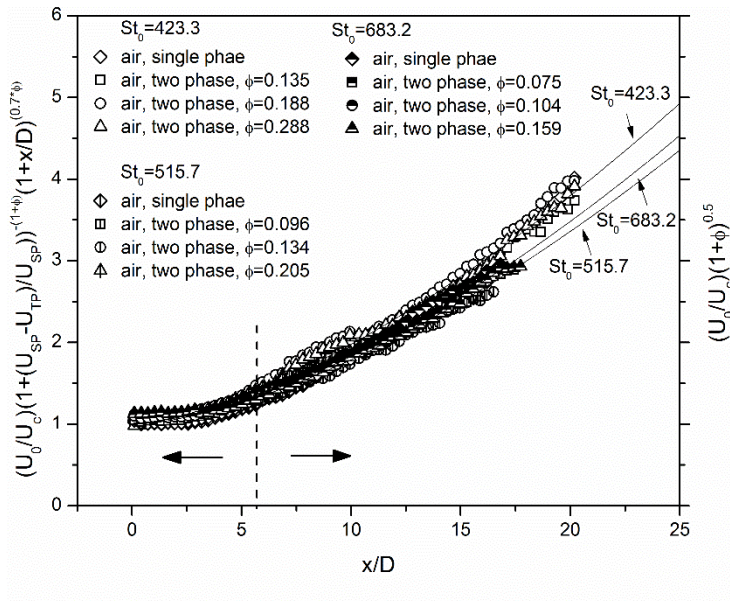


Fig. 4.13 Gas phase centerline velocity as a function of  $St_T$  and  $\phi$ .

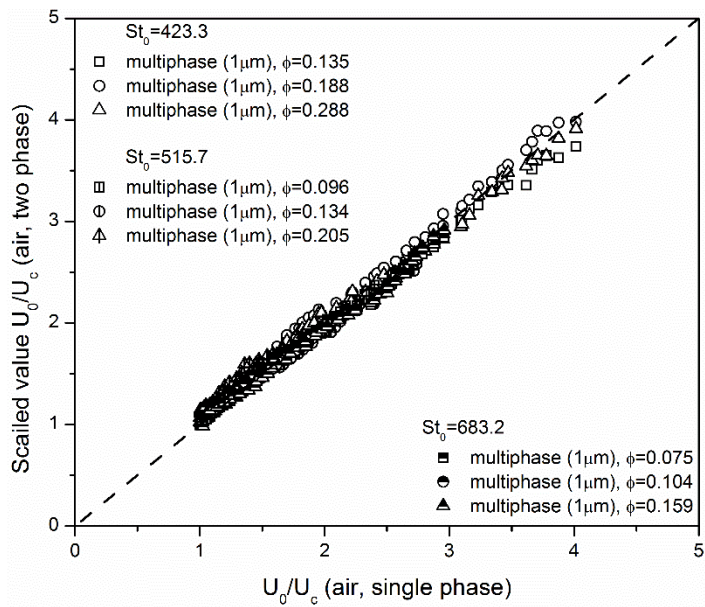


Fig. 4.14 The comparison between the single- and two-phase centerline velocities.

#### 4.4.2 Centerline Velocity Decay of Particle

The centerline velocity decay in the profile similarity zone of axisymmetric jet is typically modeled like Eq. 4.15.

$$\frac{U_o}{U_c} = \frac{1}{B_u} \left[ \frac{x}{D} - \frac{x_p}{D} \right] \quad (4.15)$$

Figure 4.15 shows the effects of particle loading ratio on particle centerline velocity decay rate. As you can see in fig. 4.15 as particle loading ratio increases centerline velocity decay rate of particle decreases. From equation 4.16 as particle loading ratio increases density of fluid increases, therefore particle Reynolds number increases.

$$Re_p = \frac{\rho_f d_p |U_f - U_p|}{\mu_f} \quad (4.16)$$

( $\mu_f$ : dynamic viscosity of fluid,  $\rho_f$ : density of fluid,  $d_p$ : diameter of particle)

From Eq. 4.16 particle Reynolds number increased when particle loading ratio increased at the time the other flow conditions are same. From Schiller and Naumann's equation of particle drag coefficient (see Eq. 4.17), as the particle Reynolds number increased drag coefficient acting on a particle is decreased (Rhodes, 2008).

$$C_d = \frac{24}{Re_p} (1 + 0.15 Re_p^{0.687}) \quad (4.17)$$

As you show in Fig 4.16 the velocity decay coefficient is linearly proportional to the particle Reynolds number measured at fully developed region in  $x/d=30$ , this result express as empirical formula like eq. 4.18. From eq. 4.17 particle drag coefficient decreased as particle Reynolds number increased, this relation explained

the experimental results conducted on present experiments.

$$B_u = 0.0815Re_{p,30} + 10.552 \quad (4.18)$$

Also, virtual origin of particle in particle-laden simple jet can be expressed as equation 4.19. This is linearly proportional to the centerline velocity decay coefficient.

$$\frac{x_p}{D} = -0.821B_u + 11.191 \quad (4.19)$$

Equation 4.18 and 4.19 is a solution for the centerline velocity decay coefficient and virtual origin of the particle in particle-laden jet. As you see in the fig. 4.17, these equations can be applied regardless of the nozzle diameter, length and carrier gas velocity.

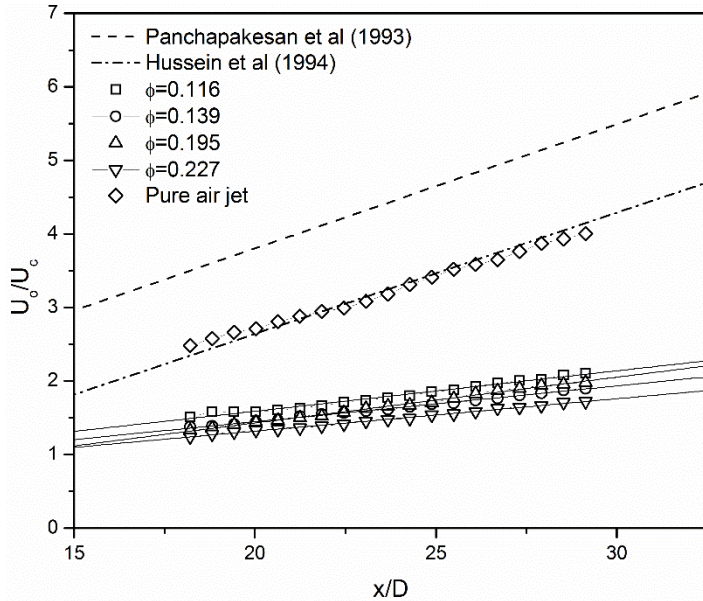


Fig. 4.15 Centerline velocity decay profile.

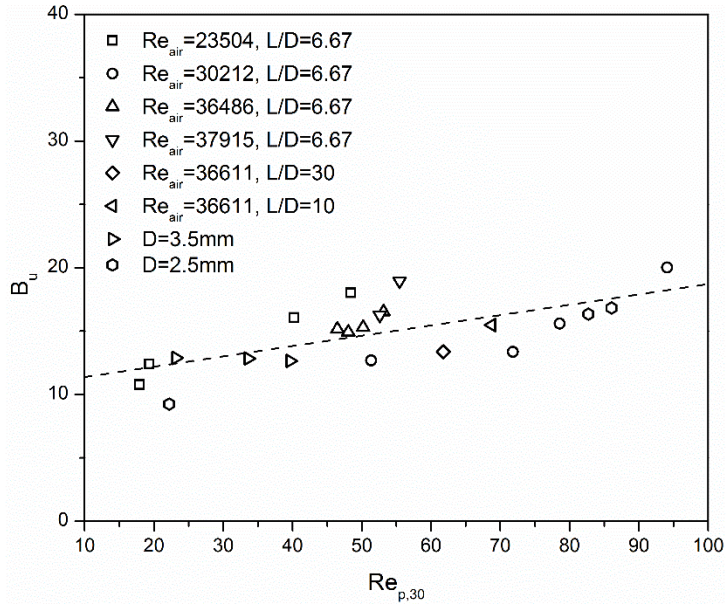


Fig. 4.16 Velocity decay coefficient.

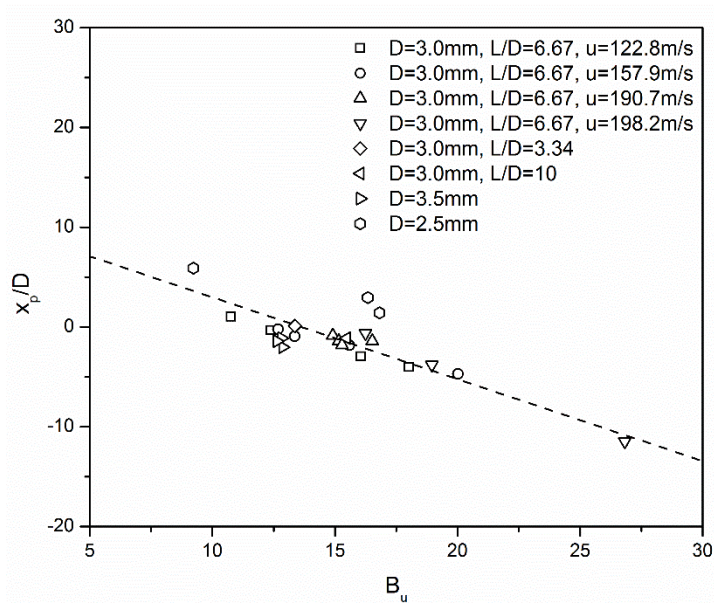


Fig. 4.17 Virtual origin of particle-laden flow.

## 4.5 Turbulence Modulation

In the two-phase flow, it is well known that particles may either attenuate or enhance the level of turbulence. The degree of change in turbulence intensity (CTI) is quantified by the difference between the turbulence intensities of the particle-laden two-phase flow and the single-phase flow (see Eq. 4.20).

$$CTI = \frac{\sigma_{TP} - \sigma_{SP}}{\sigma_{TP}} \quad (4.20)$$

Where  $\sigma_{TP}$  and  $\sigma_{SP}$  are the two- and single-phase turbulence intensities ( $u'/U_c$ ), respectively.

Gore and Crowe (1989) were able to demarcate turbulence measurements in a two-phase pipe and jets by the parameter  $d_p/l_e$  ( $l_e$  is the integral length scale or the characteristic length scale of the most energetic eddy), where the critical value of  $d_p/l_e$  is approximately 0.1, CTI is positive above this value and below this is negative, corresponding to the enhancement or attenuation of turbulence, respectively. Characteristic length scale  $l_e$  is equal to 0.1D and is independent of the Reynolds number, the ratio  $d_p/l_e$  for the  $d_p = 42.5 \mu m$  in the present work is approximately 0.106. Figure 4.18 shows turbulence modulation with respect to the ratio of particle size to turbulence length scale adopted from Mandø et al. (2009). This figure clearly agree with Gore and Crowe's criterion of turbulence modulation (Gore and Crowe, 1989). However, this study shows characteristic length scales alone, is not sufficient in predicting gas phase turbulence modulation. These results are also suggested by Hadinoto et al. (2005) and Mergheni et al. (2009). Therefore, another factor such as mean slip velocity, particle loading ratio and Reynolds number that influence on the gas phase turbulence also considered.

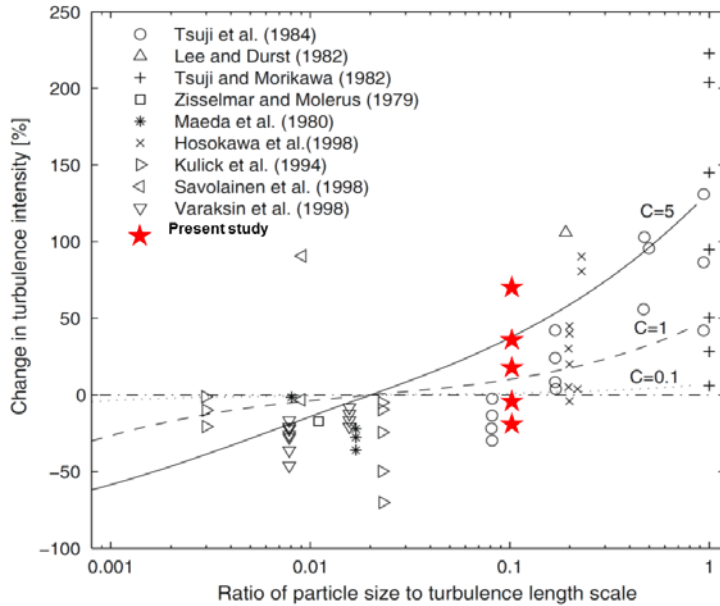
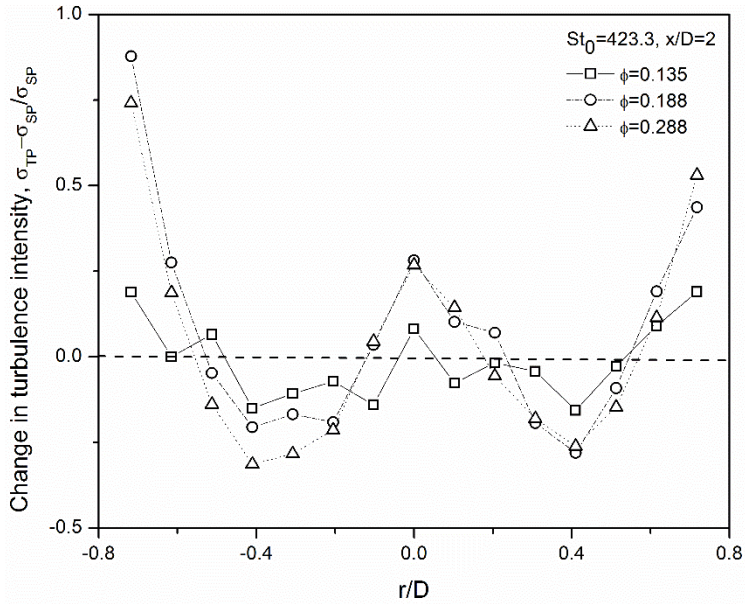


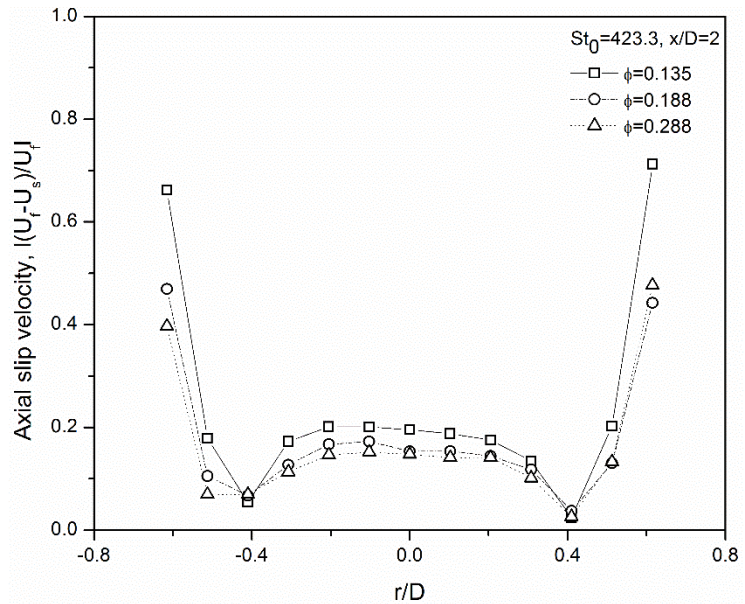
Fig. 4.18 Turbulence modulation with respect to the ratio of particle size to turbulence length scale.

In the present work, the trend in the turbulence modulation as a function of the particle-loading ratio is investigated along the two different distances from the nozzle exit ( $x/D = 2$ ,  $x/D = 16$ ). Furthermore, the particle-laden flow experiment is conducted at  $\Phi = 0.135$ ,  $0.188$ , and  $0.288$  under the high Stokes number condition ( $Stk_0 = 423.3$ ). Figure 4.19 shows that the CTI is enhanced with respect to the single-phase in the center of the jet, than CTI reduced until the region of  $r/D = 0.4$ . At this region ( $r/D=0.4$ ) gas phase turbulence has a lowest for all cases. It seems to be related with the slip velocity, because this region slip velocity between particles and air is almost zero. Therefore, this region turbulence attenuated in the presence of particle. As the particle-loading ratio is raised from  $0.135$  to  $0.288$ , Fig. 4.19(a) shows that the degree of the turbulence enhancement in the center of the jet region increases considerably ( $\approx 30\%$ ), and away from the jet core ( $r/D = 0.4$ ), turbulence attenuation is observed ( $\approx -30\%$ ), whereas the turbulence intensity  $r/D > 0.6$  is turbulence enhanced. From this experimental results indicate that consideration of characteristic length scales alone, is not sufficient in predicting gas phase turbulence

modulation. Therefore, mean slip velocity profile is also considered. Fig. 4.19(b) show the absolute value of mean slip velocity  $\left(\left|\frac{U_f - U_s}{U_f}\right|\right)$ , this profile seems to quite similar with turbulence modulation profile. Because at high Re, it seems to in the presence of high inertial particles is attributed to a modified turbulence production by the interaction between particles and flow due to the high mean slip velocity. The relation of mean slip velocity in initial jet region was obtained (Fig.4.20). As you shown in Fig. 4.20 as mean slip velocity increased, turbulence modulation also increased. Therefore, mean slip will produce the flow turbulence in the initial jet region. In low slip velocity cases  $\left(\left|\frac{U_f - U_s}{U_f}\right| < 0.2\right)$ , the particle inertia causes local attenuation of the gas phase turbulence.

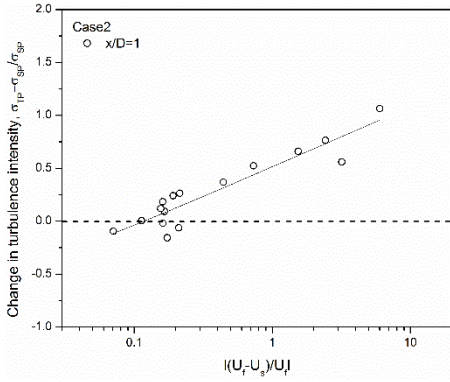


(a) Turbulence modulation

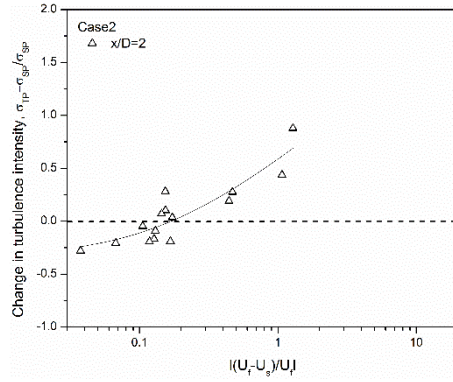


(b) mean slip velocity profile

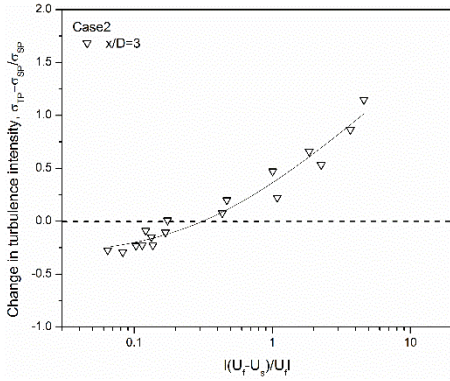
Fig. 4.19 Turbulence modulation (a), mean slip velocity profiles (b) at  $x/D = 2$ .



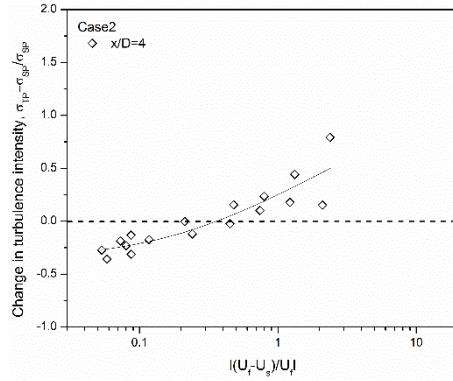
(a)  $x/D=1$



(b)  $x/D=2$



(c)  $x/D=3$



(d)  $x/D=4$

Fig. 4.20 Turbulence modulation at initial jet region as a function of mean slip velocity at different measurement location from the nozzle exit (case 2)

To investigate the effect of particle loading ratio on the gas-phase turbulence modulation, a gas-particle flow experiment conducted at a varying particle loading ratio 0.135, 0.188 and 0.288. Fig. 4.21 show that the effect of particle loading ratio on gas phase turbulence, as shown in the fig. 4.21 the gradient of CTI is increased with particle loading ratio increased. Therefore, particle loading ratio also effect on turbulence modulation. Fig. 4.22 shows effect of Reynolds number on turbulence modulation under similar particle loading ratio condition. As Reynolds number is raised from 20400 to 32900, the degree of the turbulence enhancement in the large mean slip velocity region is gradually magnified. These result was similar to Hadinoto et al. (2005). Fig. 4.24 shows the distributions of the correlation coefficient between the CTI and mean slip velocity for initial jet region for the entire experiment cases. For particle volume loading ( $\phi_v$ ) larger than  $4 \times 10^{-5}$ , the correlation coefficients are large than 0.8, which shows that the CTI is linearly related to the mean slip velocity. For particle volume fraction smaller than  $4 \times 10^{-5}$ , the correlation coefficients decrease, which represents the in small volume loading cases, mean slip velocity doesn't effect on turbulence modulation. This result also shown in fig. 4.23, from that  $x/D$  increases, particle volume fraction decreased, and correlation coefficient also decreased. In the present work  $d_p/l_e$  is approximately 0.106. Hence, according to the criterion of Gore and Crowe (1989), gas turbulence may be increased or decreased in this region. The present experimental data indicated that the consideration of characteristic length scales alone, which are independent of mean slip velocity, is not sufficient in predicting gas-phase turbulence modulation. Mean slip velocity and particle loading ratio are also considered for predict turbulence modulation on gas phase in developing region of the particle-laden jet.

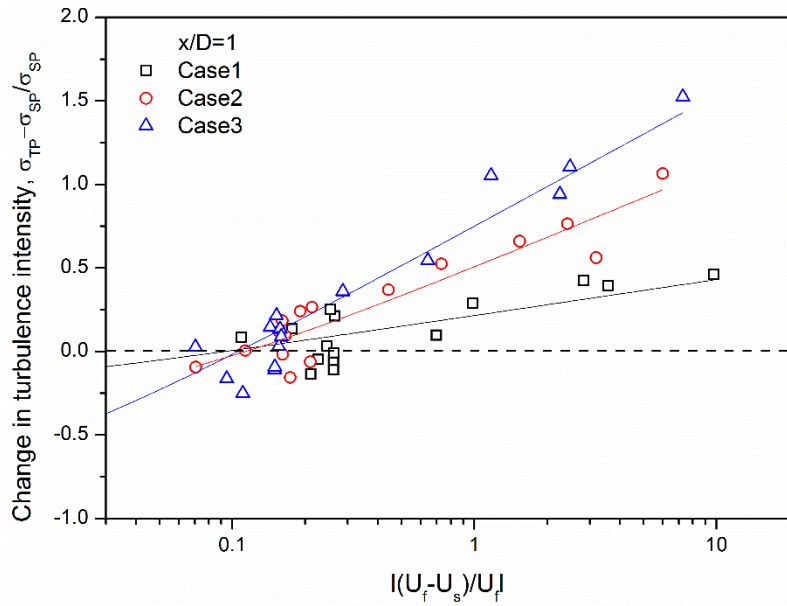


Fig. 4.21 Turbulence modulation at initial jet region as a function of mean slip velocity at different particle loading ratio.

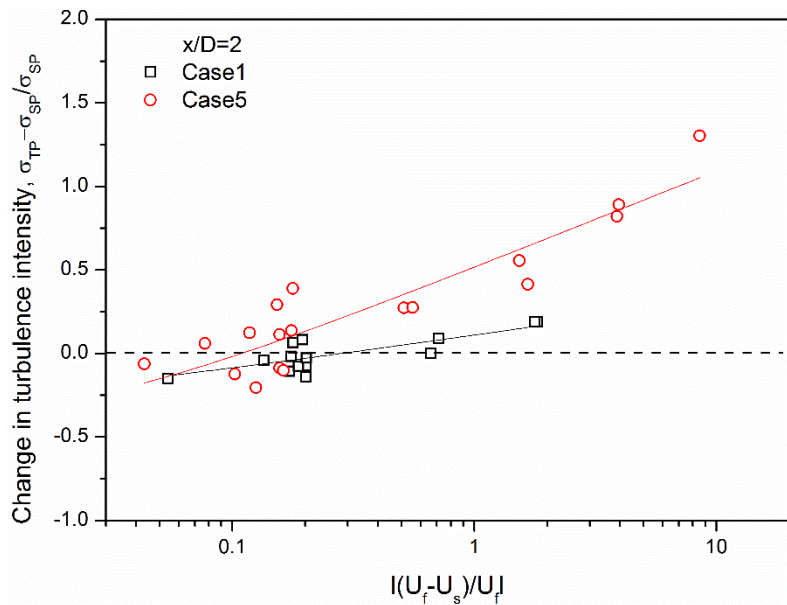


Fig. 4.22 Turbulence modulation at initial jet region as a function of mean slip velocity at different Reynolds number.

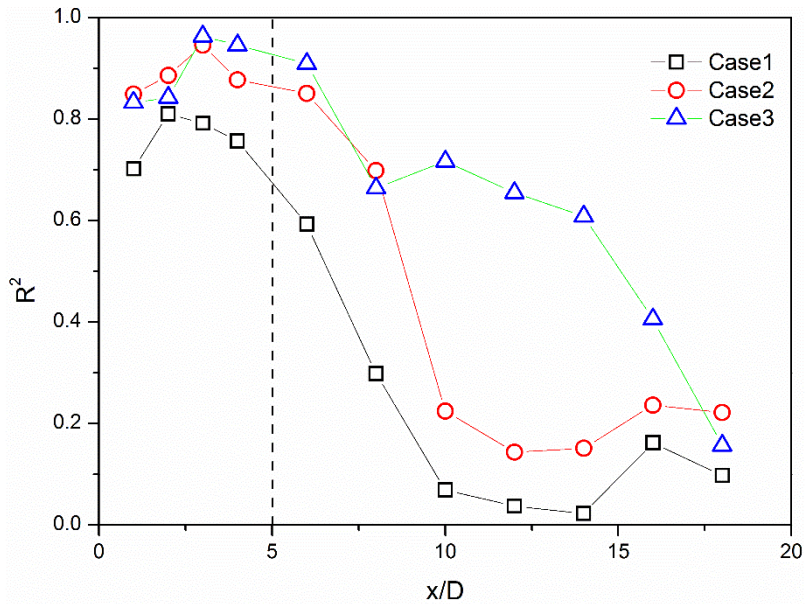


Fig. 4.23 Turbulence modulation at initial jet region as a function of mean slip velocity at different Reynolds number.

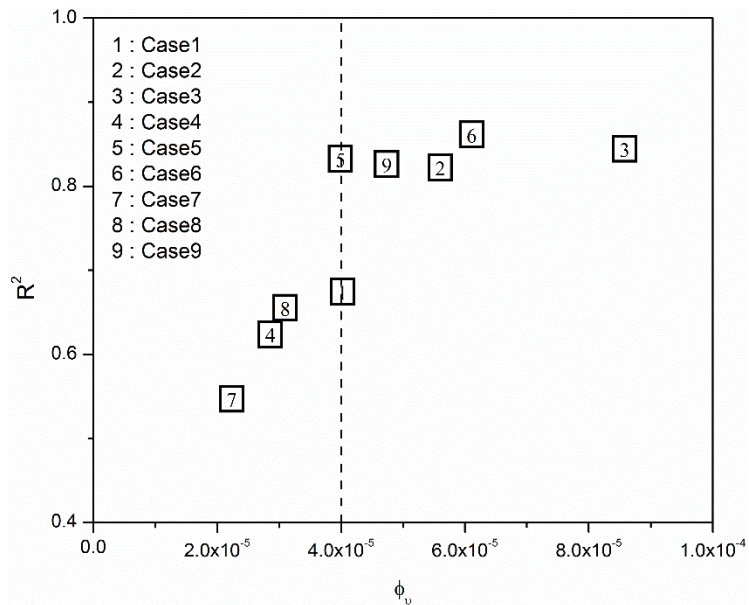


Fig. 4.24 Turbulence modulation at initial jet region as a function of mean slip velocity at different Reynolds number.

## CHAPTER 5

# SPRAY CHARACTERISTICS OF PARTICLE-LADEN COAXIAL JETS

### 5.1 Background and Objectives

Metal particles such as Al or Mg and water have been proposed as propellant both for space (Foote and Litchford, 2005, Goroshin et al., 1999) and for underwater propulsion (Miller and Herr, 2004, Foote et al., 1996), due to its high volumetric heat release associated with combustion. Power generation using metal powder fuel propulsion systems includes many processes: pyrolysis, gas-phase diffusion, mixing and combustion. These metal particles difficult to obtaining complete combustion within the combustor length (Pang et al., 2009). Fuel particle dispersion characteristics strongly influence on local temperature distribution and gas concentration levels (Liu et al., 2012). Thus, mixing of fuel particle and oxidizer should be enhanced. Injector, play a major role in mixing characteristics due to which provides the oxidizer and fuel to the combustion chamber. Also, it is direct influence on the performance and stability of the engines.

Coaxial injectors, consisting of an inner injector surrounded by annular outer injector, show many advantages for high performance and stability with broad ranges of operation due to uniform mixing of propellants. Shear coaxial type injector have been widely used for aluminum powder combustion system, Miller et al., investigated the effect of oxidizer-fuel ratio on specific impulse in linear combustor with magnesium-water and aluminum-water propellants(Miller and Herr, 2004). Foote et al., used preheated particles with propane flame to reduce ignition delay time (Foote et al., 1996).

Many experimental studies have been conducted on particle dispersion characteristics in particle-laden flows. Hardalupas and Horender measured as mean and rms of fluctuations of particle velocities and concentration in a turbulent two-

phase shear layer (Hardalupas and Horender, 2003). Longmire and Eaton experimentally investigated the non-evaporating droplet dispersion in round jet. Their results clearly showed that the particles at the Stokes numbers near unity concentrate largely in the high strain rate and low vorticity regions (Longmire and Eaton, 1992). This non-uniform particle distribution is known as ‘preferential concentration’ (Eaton and Fessler, 1994).

Historically, turbulent particle-laden jets have been the subject of many studies but, until very recently it has been difficult to find in the literature a well-documented experimental study of spray characteristic in particle-laden coaxial jet. Recently a few research has been conducted of particle-laden coaxial jet. Mergheni et al., studied the effect of solid particles on the flow characteristics of axisymmetric turbulent coaxial jets (Mergheni et al., 2009). They suggested gas characteristic length scale is insufficient to predict gas-phase turbulence modulation in gas-particle flows. Liu et al., reported effect of particle size on dispersion angle of the particle (Liu et al., 2012). They found that the as particle size increases dispersion angle decreased. Wicker et al., studied effects of annular swirl flow on particle concentration, they concluded Stokes number significantly effect on particle concentration especially, Stokes number near unity particles were preferentially concentrated in the regions between the vortex rings (Wicker and Eaton, 2001). However, the literature includes few studied on the mixing characteristics in shear or swirl coaxial injectors. Kim et al. investigated effects of recess on mixing efficiency in liquid-liquid swirl coaxial injector. They reported the mixing efficiencies in internal mixing injection were higher than those of external or tip mixing. Therefore, the present study was intended to focus on the viewpoint of mixing efficiencies.

In the present study aluminum oxide with nominal diameter of  $42\mu\text{m}$  was used as a simulant of aluminum fuel, which injected in the central jet of a coaxial injector and coaxial air used as a simulant of steam. To investigate mixing characteristics of fuel particle and oxidizer in particle-gas coaxial injectors, both concentration distributions of the fuel and oxidizer have to be measured. For these measurements,

acetone PLIF (planar laser-induced fluorescence) for coaxial gas concentration and PN (planar nephelometry) for central particle concentration simultaneously conducted. The acetone PLIF technique, which is based on the linearity of the fluorescence signal to the acetone concentration, can be obtain two-dimensional concentration distribution. PN infers the relative particle number density (i.e. concentration) from the intensity of the measured Mie scattering signal (Birzer et al., 2012). In this paper, fuel and oxidizer dispersion characteristics, and mixing characteristics in particle-laden shear and swirl coaxial jets is investigated experimentally under various velocity ratio and recess conditions.

## 5.2 Experimental Conditions

Air is used as the carrier gas, and the airflow rate is measured and controlled by a mass flow controller (C100H-DD-4-OV1-V2-V1-S0-C0; Sierra Instruments, USA). Particles of primary size 35–50  $\mu\text{m}$  are supplied to the pipeline via a particle feeder using an automated feeding screw. To determine the orifice exit velocity, tracer particles with a primary size of 0.5–2  $\mu\text{m}$  are respectively provided to the pipeline by a tracer feeder. The terminal velocity and relaxation time are calculated from respectively (Rhodes, 2008),

$$u_t = \left[ \frac{4g d_p (\rho_p - \rho_f)}{3\rho_f C_{D0}} \right]^{0.5} \quad (5.1)$$

$$\tau_s = \frac{\rho_p d_p^2}{18\mu} \quad (5.2)$$

Table 5.1 Properties of the particles.

	<b>Tracer</b>	<b>Particle</b>
Mean diameter, $d_p$ ( $\mu\text{m}$ )	1	42.5
Standard deviation for the diameter, $\sigma$ ( $\mu\text{m}$ )	0.75	19.9
Density, $\rho$ ( $\text{g}/\text{cm}^3$ )	3.97	3.97
Terminal velocity, $u_t$ (m/s)	0.00012	1.25
Relaxation time $\tau_s$ (ms)	0.012	20.9

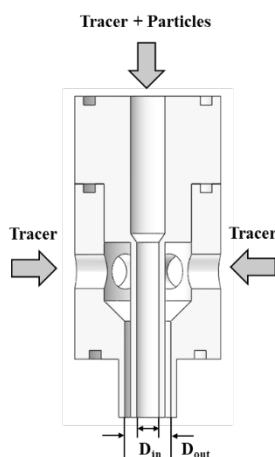


Fig. 5.1 Schematic of Coaxial Injector.

Table 5.1 summarizes the properties of the tracer and particle. The terminal velocity and relaxation time for tracer particle is very small, showing good ability in the air suspension and in following the airflows. As shown in Figure 5.1 the diameter of inner nozzle ( $D_{in}$ ) was 4mm and the diameter of outer nozzle ( $D_{out}$ ) was 8mm. Swirl coaxial injector with four tangential entry of diameter of 4.5mm was also made. The experimental chamber is sealed with transparent polycarbonate covers with the ceiling open, and the chamber has a 1,000 mm  $\times$  1,000 mm  $\times$  1,500 mm. The axial distance from the jet exit to the downstream end of the chamber was 1000 mm, while the distance from the center of the jet to the sidewalls of chamber was 500 mm. The maximum full width of the jet was approximately 25 mm at the end of measurement section that makes the free from wall effects within the working region. A PIV measurement is used to measure the air and particle velocities. The particle laden flow transitions from a horizontal section of pipe through a 90° bend to the vertical nozzle with a length to diameter ratio of 150. This long pipe in order to redistribute the particles after the bend and 150 nozzle diameters are found to be adequate to obtain fully developed flow. The convergent nozzle has a contraction ratio of 5.06 with an exit diameter of 4 mm. A honeycomb straightener is located at the top of the test chamber to allow for the free

entrainment of air from the surroundings by the expanding jet. Fans are placed at the cyclone separator to create a favorable pressure drop at a maximum velocity of 0.2 m/s that drives the particles out of the test rig to a cyclone separator.

The laser system used in the experiment is a dual head PIV Nd-YAG laser (Surelite II-PIV). A pulsed laser sheet beam with a 10 Hz pulse frequency, made by a digital pulse generator (DG535; Stanford Research Systems, Sunnyvale, California, USA) and optical lenses, is passed vertically through the jet center, and particle scattering images are captured by a CCD camera (VH-2MC-M42; Vieworks, Korea) with a  $1,200 \times 1,600$  pixel. . Each case, 300 pairs of CCD images are acquired to obtain the averaged velocity vector fields. Field of view of this experiments is 31.5 mm (width)  $\times$  42 mm (height).

The particle feeder is designed to supply constant particle mass flow rates. A cone structure inside the particle feeder is sealed with a polycarbonate cover and pressurized to the same pressure using a tube where the air passes through to prevent a backward flow of particles. A screw, which is put inside the particle feeder, is rotated by an AC variable speed motor attached to an end of the screw. When the screw spins, the particles loaded between the screw's pitch are transported to an airline. The particles fluidized by the air are then sprayed through the injector orifice.

The particle-loading ratio  $\phi$ , is defined as the ratio of the total solid mass flow rate to the mass flow rate of the air jet at the nozzle exit ( $\frac{\dot{m}_p}{\dot{m}_f}$ ). In the present work, the particle-laden flow experiment is conducted in the two-way coupling region. The Stokes number at the nozzle exit  $St_0$ , which is defined as the ratio of the particle response time to the fluid response time, characterizes the responsiveness of the particles to the fluid-phase turbulent fluctuations (Hardalupas et al., 1989).

$$Stk_0 = \frac{\tau_p}{\tau_f} = \frac{\rho_p d_p^2 U}{18\mu D} \quad (5.3)$$

Particles are usually classified into three regimes:  $St_0 > 1$  ('unresponsive'),  $St_0 \sim 1$  ('partially responsive'), and  $St_0 < 1$  ('responsive'). The  $St_0$  values for the 42- $\mu\text{m}$  aluminum oxide are between 423.3 which indicates that the particles are unresponsive to the fluid motion and these particles are governed by particle–particle collisions. Moreover, the  $Re_p$  of the obtained data is significantly less than 400; therefore, the vortex shedding phenomenon does not affect the turbulence modulation (Hetsroni, 1989).

$$Re_p = \frac{\rho_f |u_f - u_p| d_p}{\mu} \quad (5.4)$$

Where  $u_f$  is the fluid velocity,  $u_p$  is the particle velocity, and the  $\rho_f$  is the fluid density. A summary of the experimental condition is provided in Table 5.2.

Table 5.2 Experimental conditions.

Case	$d_p$ ( $\mu\text{m}$ )	O/F	$U_o/U_i$	$\phi$
Case 1	1, 42.5	3.26	0.28	0.135
Case 2	1, 42.5	3.21	0.57	0.188
Case 3	1, 42.5	3.13	0.88	0.288
Case 4	1, 42.5	3.22	1.23	0.405

### 5.3 Effect of Particle Loading Ratio on Gas Phase Velocity

In this section, measurements of the mean velocities of the gas and particle phase, normalized by the single-phase centerline velocity  $U_0$ , are reported and analyzed. Figure 5.2 shows the normalized mean axial velocity along the axial distance from the nozzle exit to  $x/D = 10$  in single- and two-phase flows for the  $\Phi = 0.135, 0.188, 0.288$ . The radial distribution of the two-phase gas velocity was lower than the single-phase in the initial jet region ( $x/D < 8$ ). However, in the fully developed region, the two-phase gas velocity was slightly greater than the single-phase. In this experiment, the particle-laden jet showed the particle-developing region ( $x/d < 8$ ), which is defined as a zone from the orifice exit to the point where the particle velocity reaches the maximum, as shown in Fig. 5.2. If the Stokes number is much greater than one and acceleration length of the nozzle was short, the particles are unable to reach the fluid phase exit velocity due to their inertia, so the particle-developing region appears. Past the particle-developing region ( $x/D > 8$ ), the particle velocity dwindles, and the region particle velocity is greater than that of the gas phase. This region the centerline decay rate of the particle was observed lower than the fluid phase velocity decay rate.

As shown in Fig. 5.2, the gas-phase velocity in the developing region is lower than the single-phase velocity with increase of particle loading ratio. This is due to the particles entering inside the injector nozzle at a velocity lower than the local gas flow. In order to create a momentum exchange between the particle and local gas flow, particles were accelerated through the injector section and the gas phase was decelerated, resulting in a lower velocity at the injector exit. This velocity was decreased with increases in the particle-loading ratio. Beyond the developing region, due to the momentum exchange from particle to fluid, the gas-phase velocity decay rate is less than the case of a single-phase flow and that decreased with increases in the particle-loading ratio.

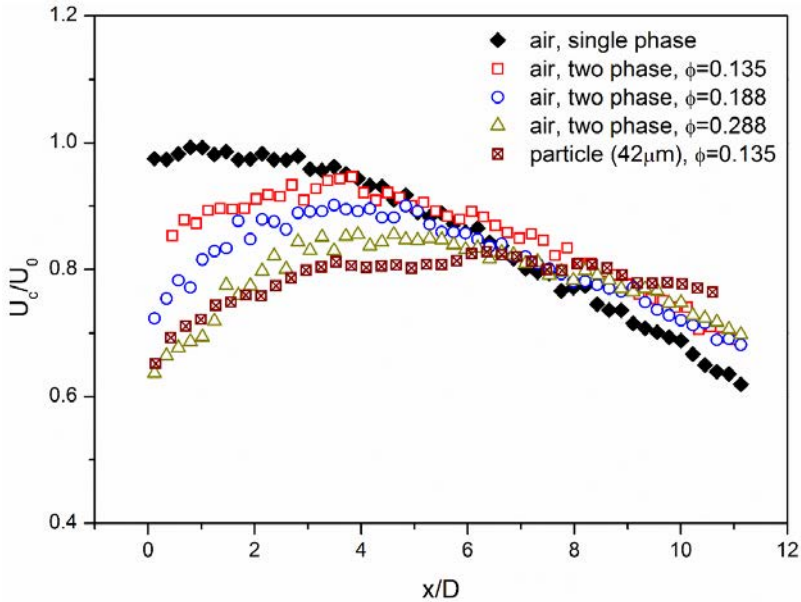
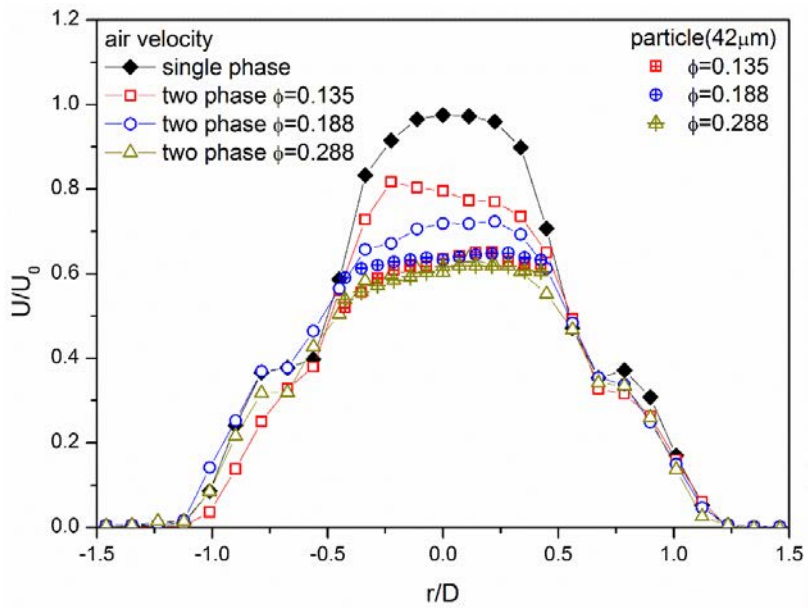
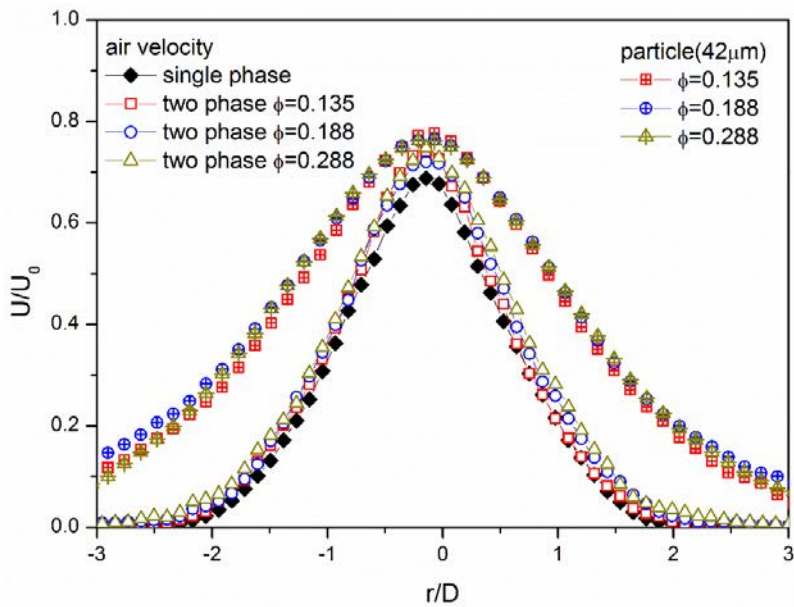


Fig. 5.2 Axial profiles of mean velocities of single phase, two phase, and solid particles.

Figure 5.3 shows the radial velocity profiles before and after the developing region. Figure 5.3(a) show the effect of particle loading ratio on gas phase and particle at  $x/D=0.1$ . In this region gas phase velocity decreases as particle loading ratio increased. As described in the previous section, the single-phase velocity is greater compared to the two-phase velocity with increases in the particle-loading ratio. Further downstream (e.g.,  $x/D > 8$ ) (Fig. 5.3(b)), the velocity of the two-phase jet is larger than that of the single-phase with increases in the particle-loading ratio. Due to the momentum exchange from the particles to the fluid, the velocity of the gas phase in two-phase jet is higher than that of the single-phase jet. Regarding the velocities of the particles in all areas, it can be seen that they are larger than the velocity of the gas phase, due to the mass inertia of the particles.



(a)  $x/D=0.1$

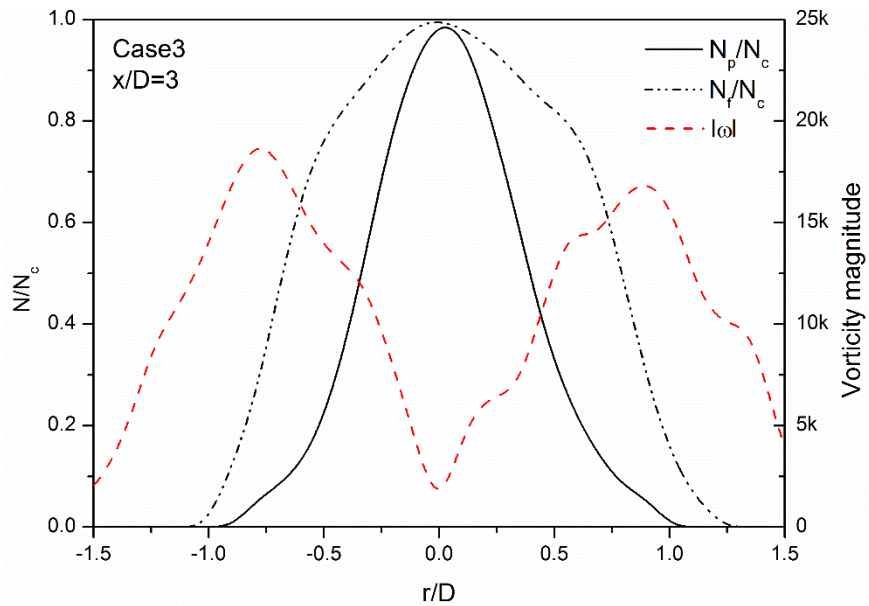


(b)  $x/D=10$

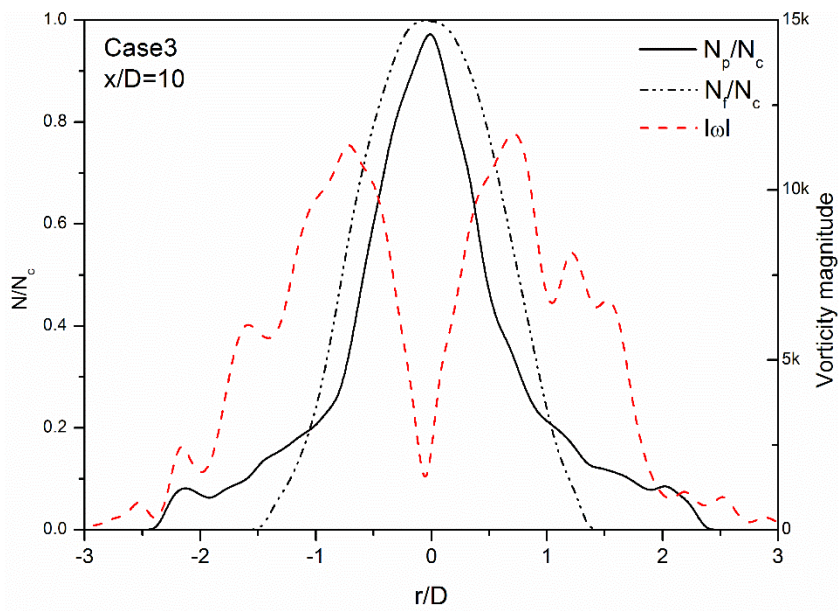
Fig. 5.3 Radial profiles of axial mean velocities.

## 5.4 Particle Distribution Characteristics

Particle mean concentration were counted in each interrogation window (this study: interrogation windows size is 32 x 32 pixel) by which is same interrogation window size of PIV/PTV and the corresponding relations of particle vorticity-concentration fluctuations of the particle flow could be resolved. In Fig. 5.4 measured mean number of particles and tracers per interrogation window at  $x/D=3$  and  $x/D=10$ , and that was normalized by its centerline mean number density. As shown in Fig. 5.4(a) particle mean number density was narrower than tracer due to the inertia of particle. Mean number density of tracers dramatically decreased at the high vorticity region, at this region, number density of large particles slowly decreased. It can be seen that at the shear layer region, large particle seems to be partially responded. If particles unresponsive or responsive about the fluid, particle distribution independent with vorticity of fluid, effect of vorticity maximized when the Stokes number on the time scale of flow is around unity.[ Crowe et al. (1996, 1997)] Therefore, in this region large particles partially reposed ( $St_0 \sim 1$ ) about the vorticity of fluid, so large particles moved span-wise direction. At the  $x/D=10$ , effect of fluid vorticity on large particles more increased than  $x/D=3$ , because gas phase time scale decreases with increased stream-wise distance due to the gas phase velocity decreased. Therefore, in this region, number density of large particles distributed more widely than tracers.



(a)  $x/D=3$



(b)  $x/D=10$

Fig. 5.4 Mean particle distribution of two-phase particle-laden jet.

For particles placed randomly in a field, the number of particles in each interrogation window should be distributed according to a Poisson distribution. Fessler et al. suggested deviation parameter that is the difference between the standard deviation of the measured distribution and the standard deviation of a random particle based on a Poisson distribution for evaluate the preferential concentration of particle (Fessler et al., 1994). This parameter identified as

$$D = \frac{\sigma - \sigma_p}{\lambda} \quad (5.5)$$

where  $\sigma$  and  $\sigma_p$  correspond to the standard deviation for the experimental and Poisson distributions, respectively and  $\lambda$  represent the mean number of particles in each interrogation window. If the particle distributed randomly  $D$  would become zero, however  $D$  becomes higher that means particles distributed non-random and preferential concentration of particle occurred.

Fig. 5.5 shows the spatially resolved distribution of the deviation parameter  $D$  for each interrogation window size. It can be seen that  $D$  maximized at the edge of the shear flow. This means that the preferential concentration is more pronounced at the edge of the shear layer than in the center of the jet. Therefore, we expect large vertical structures can effect on the non-random centration fluctuations of particle. Fig. 5.6, 5.7 shows the influence of vorticity on deviation parameter  $D$  for cross-stream location. This figure shows vortical structure influence on the non-random concentration fluctuations of particle and as particle mass loading increases intensity of vorticity decreased than deviation parameter also decreased.

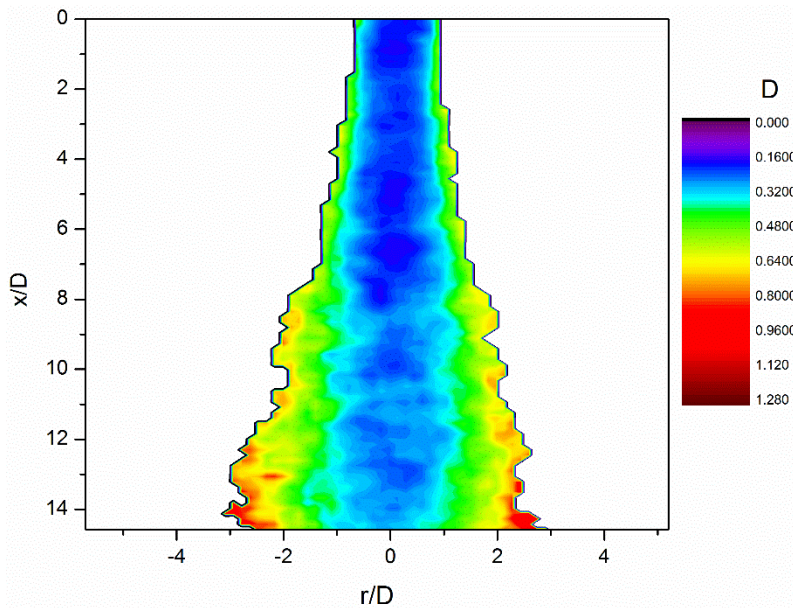


Fig. 5.5 Spatially resolved deviation parameter  $D$  of particle number density fluctuations. ( $U_o/U_i=0.57$ ,  $\Phi=0.48$ ).

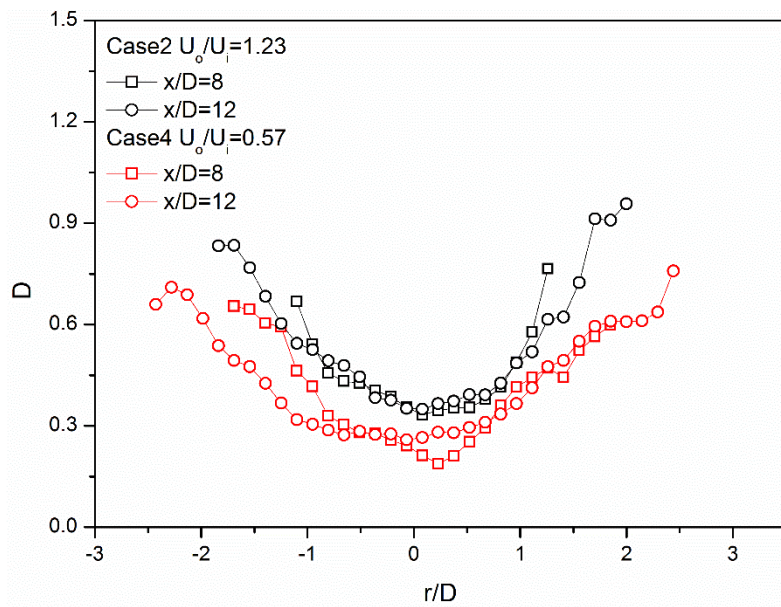
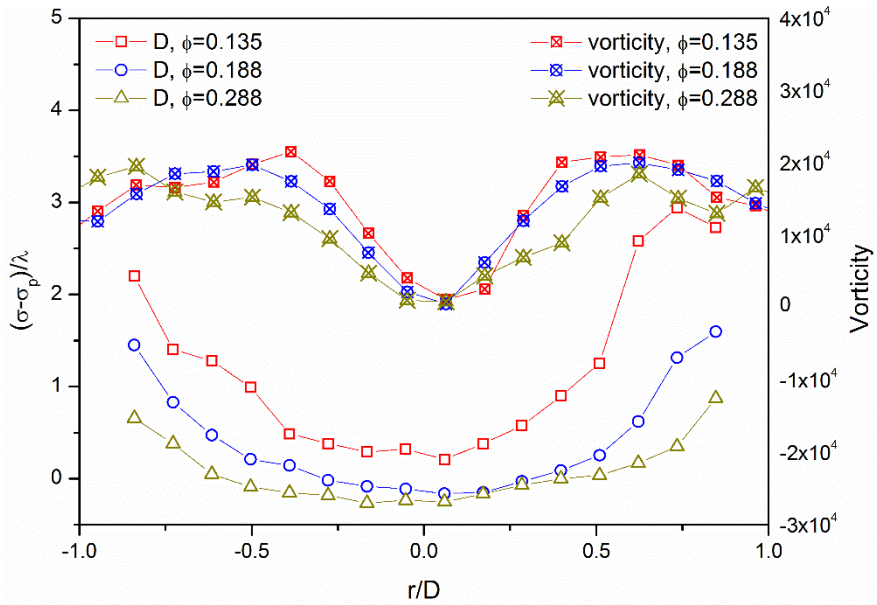
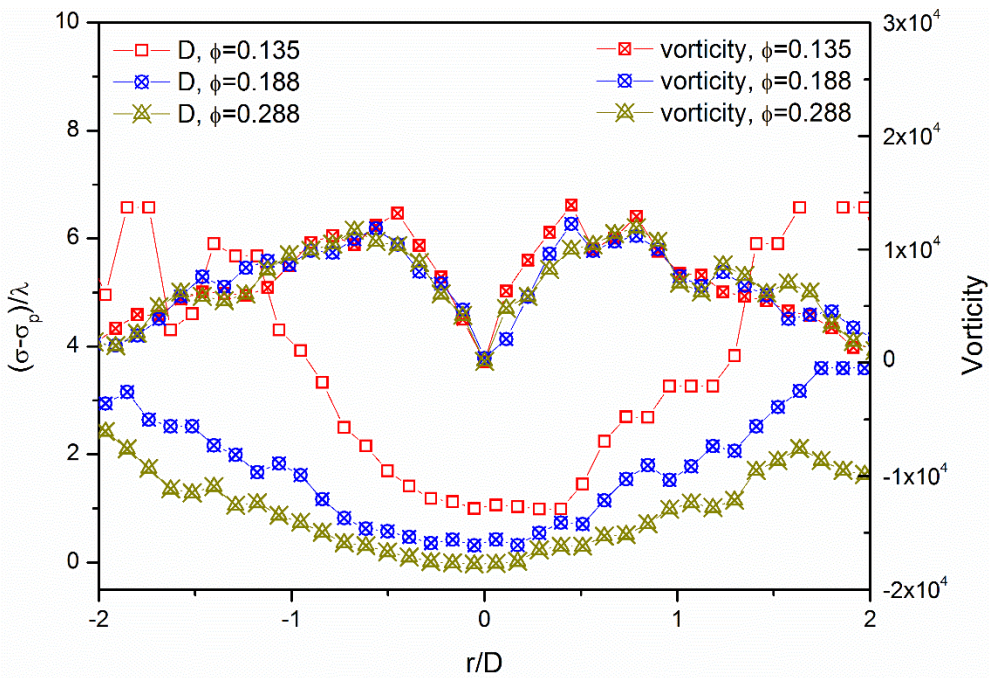


Fig. 5.6 Influence of velocity ratio on deviation parameter at lateral position.



(a)  $x/D=3$



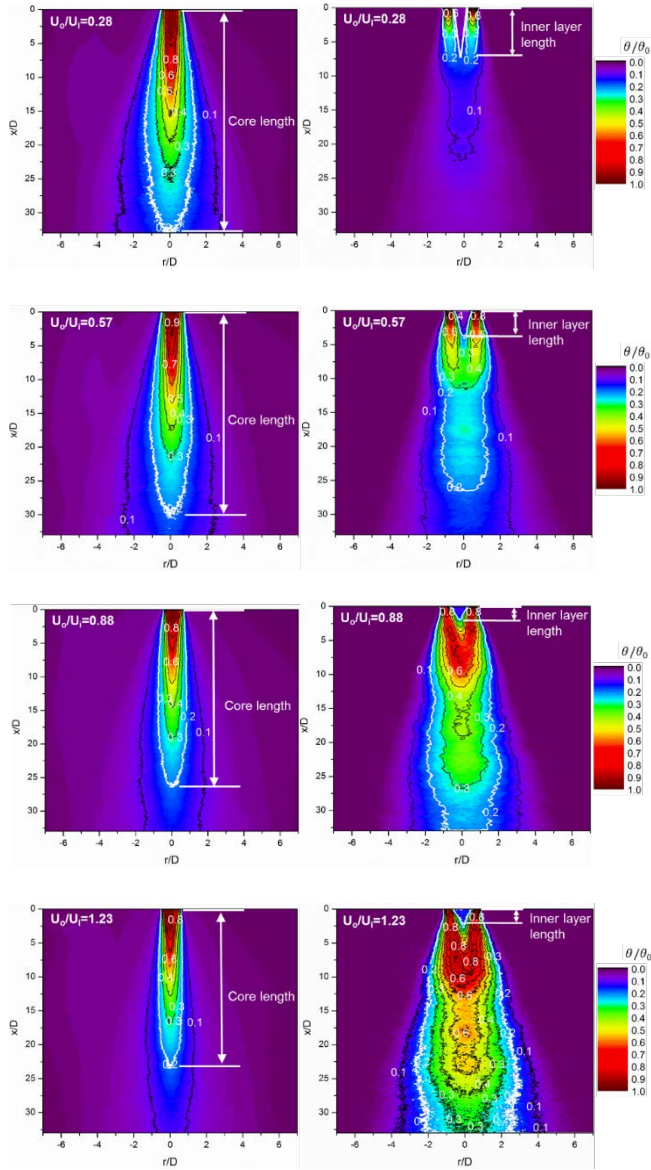
(b)  $x/D=10$

Fig. 5.7 Influence of vorticity on deviation parameter at lateral position.

## 5.5 Mixing Characteristics

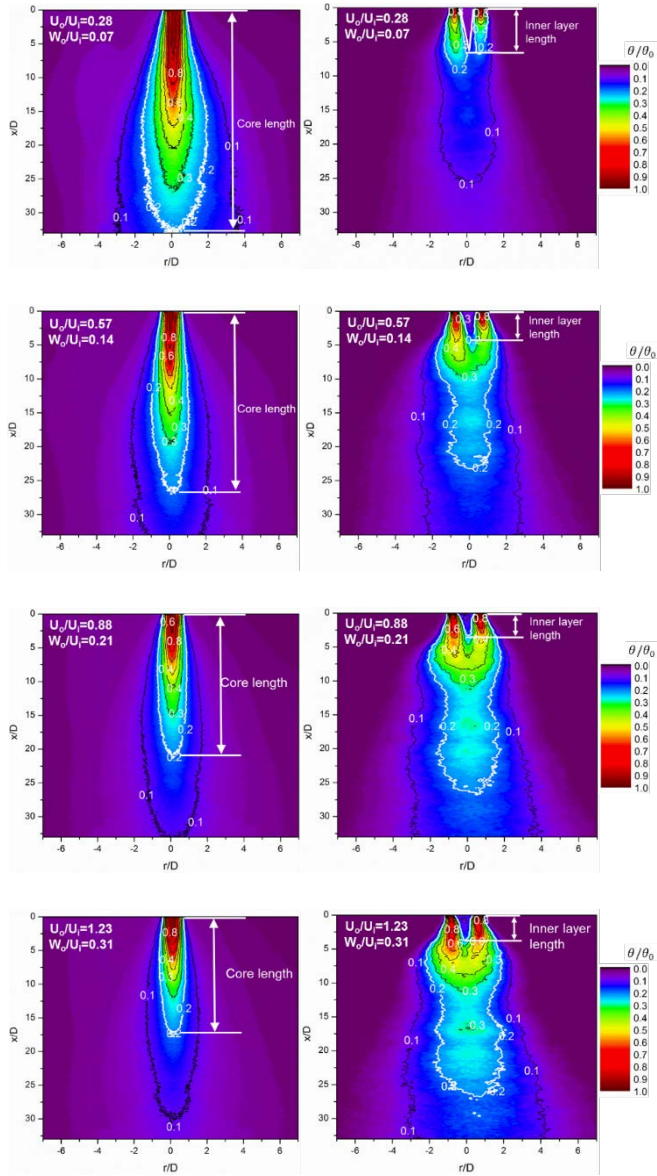
### 5.5.1 Fuel and Oxidizer Distributions

Mean concentration distributions results of fig. 5.8 and 5.9 obtained with a acetone PLIF and PN show the mean concentration of fuel (particle) and oxidizer (acetone doped air),  $\theta$ , entire flow fields normalized by the initial mean concentration,  $\theta_0$ , at the nozzle exit as a function of velocity ratio of the outer jet to inner jet. Figure 5.8 and 5.9 shows the mean concentration of fuel and oxidizer in shear coaxial and swirl coaxial injector, respectively. From these figures, the core length of fuel, which was define length from nozzle exit to the dilution levels  $\frac{\theta}{\theta_f} = 0.2$ , decreases with increase of velocity ratio in both injectors due the unmixed zone (inner layer length) decreased. This result shows entrain of outer gas increases with increase velocity ratio. That means as velocity ratio increases mixing efficiency between fuel and oxidizer increased. Whereas the oxidizer concentration of shear coaxial injector dispersed by axial momentum and shear layer mixing, the oxidizer concentration of swirl coaxial injector dispersed by axial and tangential momentum of the jet. As a result, the tangential momentum of swirl coaxial injector increases spreading angle of oxidizer is higher than that of the shear coaxial injector. However, as velocity ratio increases, the oxidizer concentration of shear coaxial injector is more concentrated at the center of the jet. From these results, the oxidizer concentration distribution of shear coaxial injector is more concentrated than that of swirl coaxial at the jet center for the same axial velocity ratio, resulting in the difference mixing efficiencies.



(a) Fuel concentration (b) Oxidizer concentration

Fig. 5.8 Averaged concentration fields of fuel and oxidizer in shear coaxial injector as a function of velocity ratio. The white contours correspond to the dilution levels  $\frac{\theta}{\theta_0} = 0.2$  (RR=0).



(a) Fuel concentration (b) Oxidizer concentration

Fig. 5.9 Averaged concentration fields of fuel and oxidizer in swirl coaxial injector as a function of velocity ratio. The white contours correspond to the dilution levels  $\frac{\theta}{\theta_0} = 0.2$  (RR=0)

### 5.5.2 Mixing Process

In order to investigate the mixing process of the both injectors (shear coaxial and swirl coaxial), we used following deviation indexes (D.I.):

$$D.I._f [\%] = \frac{\left(\theta_f - \theta_o \frac{\dot{M}_f}{\dot{M}_o}\right)}{\theta_f + \theta_o} \times 100 \quad (r_f > R_f)$$

$$D.I._o [\%] = \frac{\left(\theta_o - \theta_f \frac{\dot{M}_o}{\dot{M}_f}\right)}{\theta_f + \theta_o} \times 100 \quad (r_f \leq R_f) \quad (5.6)$$

The deviation index indicate the deviation of local concentration from the total concentration of fuel and oxidizer in measurement region. Before calculating DI, the local mixture fraction of fuel  $r_f$ , is compared to the total mixture fraction of fuel  $R_f$ . If the calculated  $r_f$  is large than  $R_f$  in a pixel, this pixel is a fuel-rich region, and deviation index of fuel,  $D.I._f$  is calculated. Conversely, if the  $r_f$  is smaller than  $R_f$ , deviation index of oxidizer  $D.I._o$  is calculated. Therefore, deviation index of fuel-rich region and oxidizer-rich region is calculated in a every pixel, and the calculated index is always positive or equal to zero.

Figure 5.10 and 5.11 shows the distributions of the deviation indices for both injectors at the  $x/D_i=0-33$  as a function of velocity ratio. The oxidizer rich, fuel rich regions and zero deviation index were expressed as flood, line contours and white line, respectively. From the figure 5.10, it was found that as velocity ratio increases, fuel rich region of shear coaxial injector with large particle fuel is narrower and shorter. That means as velocity ratio increase, zero deviation index line from the nozzle exit at the center of fluid region decreased. This will be explained by entrainment of outer gas into central jet, in high velocity case, entrainment of outer gas stronger than low velocity ratio case. Therefore, flame length will be shorter with increase velocity ratio. This result agreed with a previous study of the flame length scaling of hydrogen jet with coaxial air (Kim et al., 2011). Figure 5.11 shows the effect of coaxial gas tangential momentum on mixing process. Tangential

velocity  $W$  on the radius  $r$  can be calculated from the free vortex equation as shown in Eq. 5.7

$$W = \frac{W_p R}{r} = \frac{W_p R}{\frac{1}{2}(r_i + 2t_{lip} + r_o)} \quad (5.7)$$

Axial velocity of outer injector  $U_o$  can be expressed as follows.

$$Q = AU_o = \pi \left( r_o^2 - (r_i + t_{lip})^2 \right) U_o \quad (5.8)$$

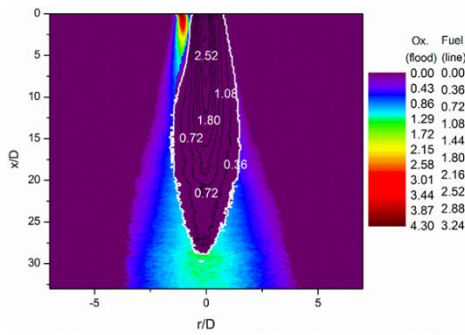
Where,  $Q$  is a volumetric flow rate and  $A$  is a area of outer injector nozzle.

$$Q = nA_p W_p = n\pi r_p^2 W_p \quad (5.9)$$

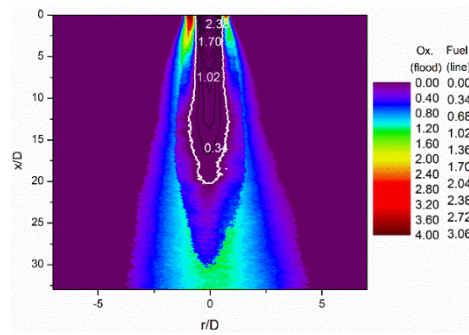
Where,  $n$  is a number of tangential entry.

$$U_o = \frac{n r_p^2 W_p}{\left( r_o^2 - (r_i + t_{lip})^2 \right)} \quad (5.10)$$

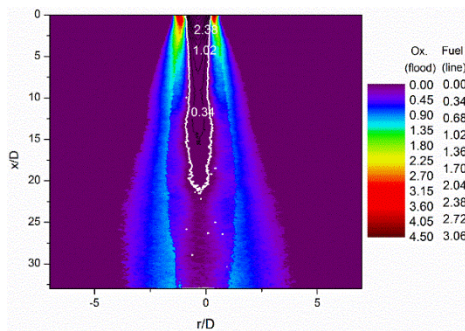
Compared with fig 5.10 and fig 5.11, fuel-rich regions of swirl coaxial injector was large than shear coaxial injector due to the effect of velocity ratio of tangential velocity of outer injector to axial velocity of inner injector ( $W_o/U_i$ ) spread oxidizer distribution widely than that of shear coaxial injector.



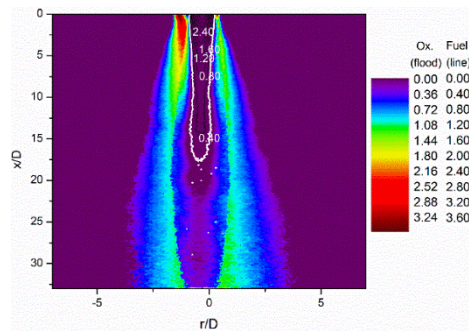
(a)  $U_o/U_i=0.28$



(b)  $U_o/U_i=0.57$

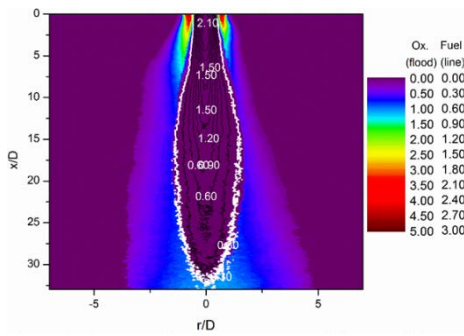


(c)  $U_o/U_i=0.88$

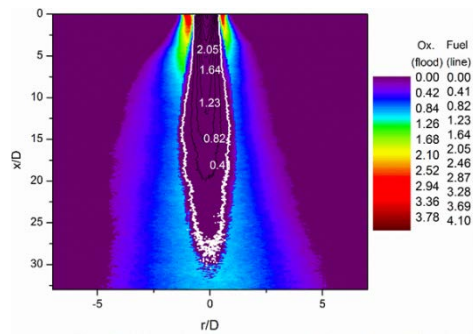


(d)  $U_o/U_i=1.23$

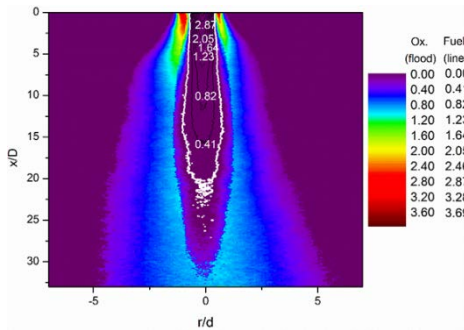
Fig. 5.10 Deviation Index of fuel and oxidizer of shear coaxial injector as a function of the  $U_o/U_i$ ; the line and flood contours indicate the fuel rich and oxidizer rich regions, respectively.



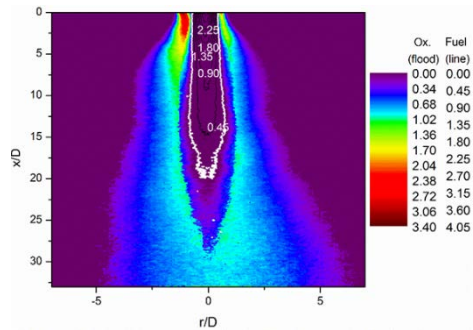
(a)  $U_o/U_i=0.28$



(b)  $U_o/U_i=0.57$



(c)  $U_o/U_i=0.88$



(d)  $U_o/U_i=1.23$

Fig. 5.11 Deviation Index of fuel and oxidizer of swirl coaxial injector as a function of the  $U_o/U_i$ ; the line and flood contours indicate the fuel rich and oxidizer rich regions, respectively.

### 5.5.3 Mixing Efficiency

In order to quantitatively compare the mixing performance between shear coaxial and swirl coaxial with small and large particle, we calculated mixing efficiencies of spray as follows (Rupe, 1956):

$$E_m[\%] = 100 - \left[ \sum_0^n D.I._f + \sum_0^{\bar{n}} D.I._o \right] \quad (5.9)$$

Above equation indicates that the mixing efficiency decreases as the deviation of the concentration ( $D.I._f$  or  $D.I._o$ ) or the area of the fuel or oxidizer-rich zone ( $n$  or  $\bar{n}$ ) increase.

Figure 5.12 shows the mixing efficiency as a function of the measurement location. First of all, it was found that the mixing efficiency of shear coaxial is lower than that of swirl coaxial injector, which results from the fact that the area of fuel or oxidizer rich zone of shear coaxial is wider than that of swirl coaxial as shown in fig. 5.10(c) and fig. 5.11(c) because the penetration of oxidizer into fuel is relatively weak in the case of shear coaxial due to the swirling momentum of swirl coaxial injector. Fig. 5.13 shows concentration half width of central particle and coaxial gas in shear and swirl coaxial injector. As shown in fig. 5.13, swirling momentum increases coaxial gas concentration half with increases, but it does not effect on central particle concentration. Therefore, coaxial gas swirling momentum decrease mixing efficiency of the particle-laden coaxial injector.

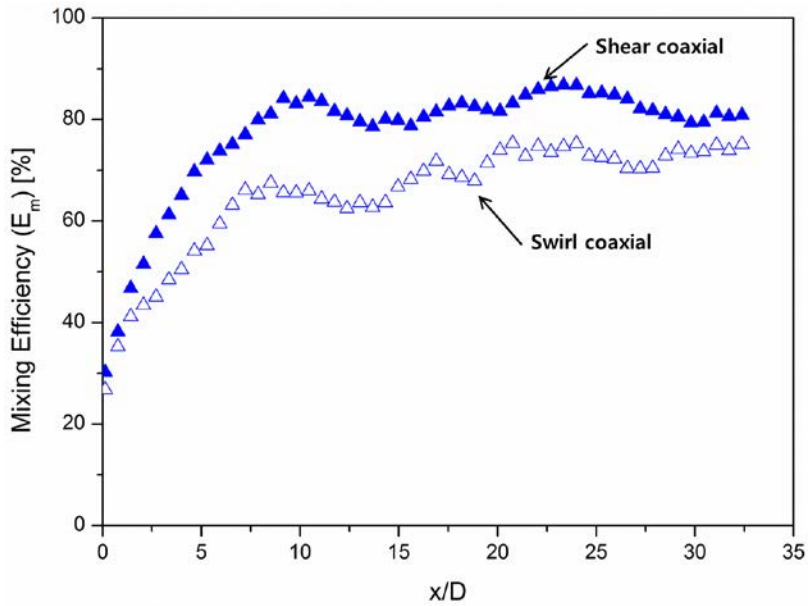


Fig. 5.12 Mixing efficiency of swirl and shear coaxial injectors as a function of measurement location ( $U_0/U_i=0.88$ , particle size ( $42.5 \mu\text{m}$ )).

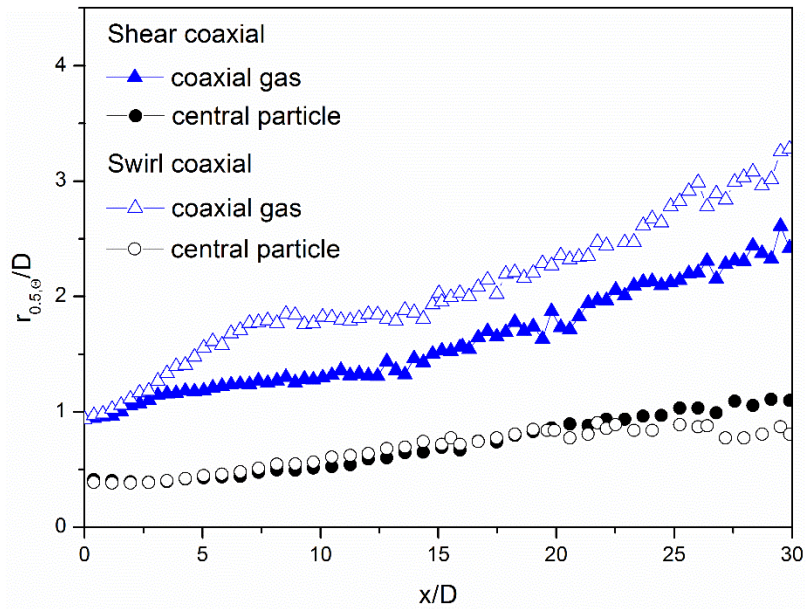
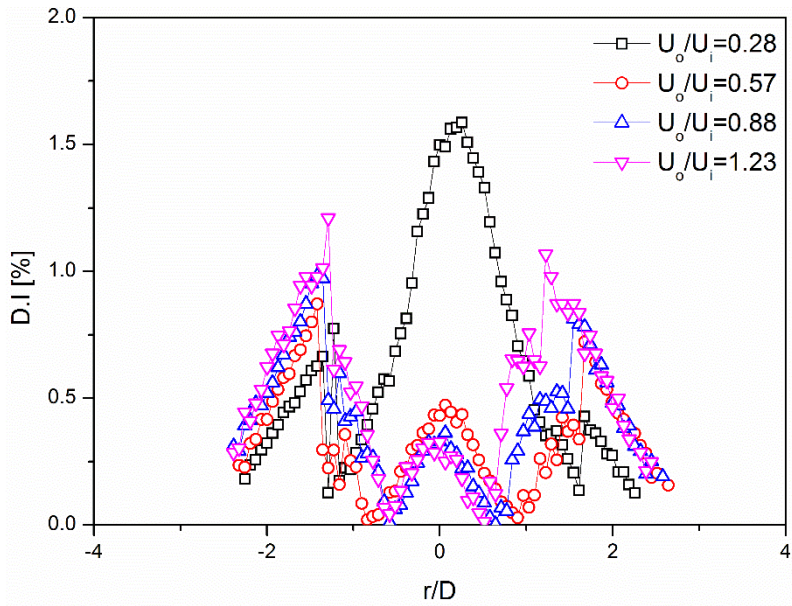


Fig. 5.13 The axial evolution of the concentration half-width ( $U_0/U_i=0.88$ , particle size ( $42.5\mu\text{m}$ )).

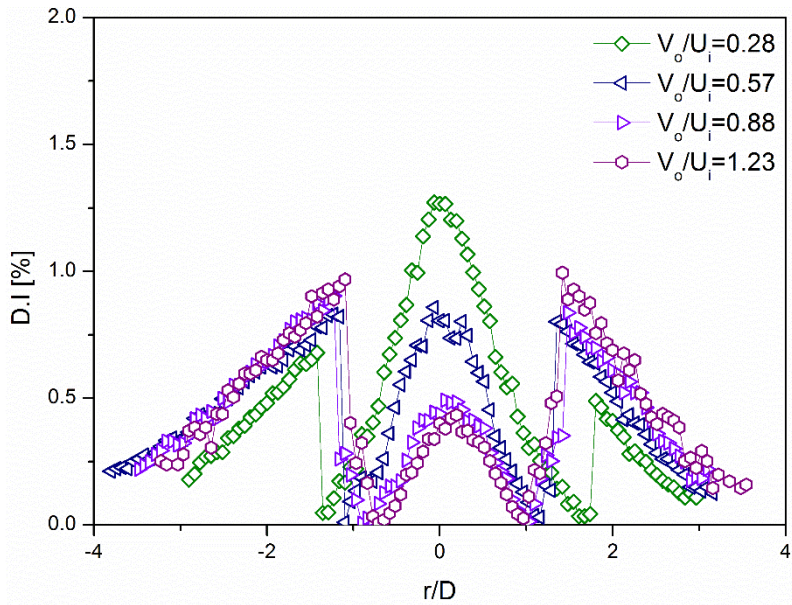
In order to compare the mixing performances of both injectors as a function of momentum ratio of oxidizer to fuel, we measured the spray mass distribution of fuel and oxidizer between  $x/D=0-33$  from the nozzle exit (see fig. 5.10). Figure 5.14 show the distribution of deviation index of oxidizer and fuel.

In the case of the low velocity ratio of 0.28, the fuel jets intensively concentrated at the central jet region as shown in fig. 5.14 and these distribution make the mixing efficiencies of shear coaxial injector decrease as shown in fig. 5.15. As the velocity ratio of oxidizer to fuel increases, the entrainment of oxidizer to fuel-rich region increases so that the central fuel-rich zones converted into oxidizer-rich zones, therefore fuel-rich zone narrower with increase velocity ratio.

From fig. 5.14, it can be estimated that the oxidizer rich-zone increases with increase velocity ratio, so as velocity ratio increases mixing efficiency increase (see fig. 5.15). The most important finding of the result of fig. 5.15 is that the efficiency of swirl coaxial is lower than the shear coaxial due to particle concentration has no affected by the outer gas swirling momentum significantly at no recess case. In both cases, mixing efficiency increases as velocity ratio increase. Because, as velocity ratio increase mixing length of fuel and oxidizer decreased, so as velocity ratio increase fuel and oxidizer homogeneously mixed at the near field from the nozzle exit. Although the mixing efficiency of shear coaxial injector is much higher to the velocity ratio than that of swirl coaxial injector, it is about 18% higher than that of swirl coaxial when the velocity ratio 0.28 because the mixing caused by the coaxial jet shear mixing is more efficient than that by the swirling momentum of coaxial jet.



(a) Shear coaxial



(b) Swirl coaxial

Fig. 5.14 Deviation Index of shear and swirl coaxial injectors as a function of velocity ratio of oxidizer and fuel at  $x/D=15$ .

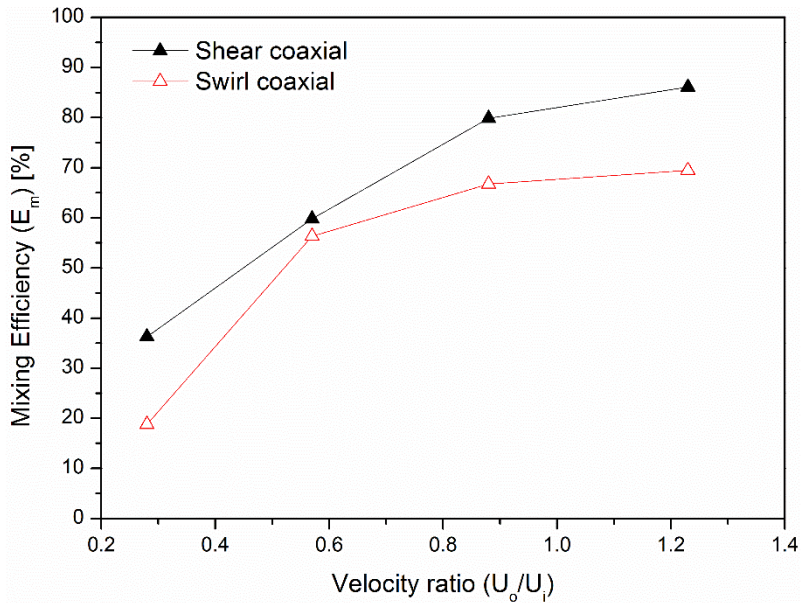


Fig. 5.15 Mixing efficiencies of shear and swirl coaxial injectors as a function of velocity ratio ( $x/D=15$ ).

#### 5.5.4 Recess ratio effects on mixing efficiency

From the result of the velocity ratio, it was found that the strong shear force of oxidizer jets can assist in mixing with fuel, but the swirling momentum of oxidizer doesn't affected on fuel distribution and reduce the mixing efficiency, in the case of injector without recess. Since the recess ratio of injector is also affected on the mixing efficiency, we investigated the effect of the recess ratio on the mixing performance.

Figure 5.16 shows the concentration half width of fuel and oxidizer as varying the recess ratio at the same velocity ratio of 0.57. As for the swirl coaxial injector, the concentration half width of fuel is almost same as shear coaxial injector at the without recess case, but the recess ratio increases, swirling momentum of oxidizer strong enough to wider the fuel concentration half width and recess ratio doesn't affected on oxidizer distribution. Therefore mixing efficiency improved of about 57%

compared with shear coaxial injector without recess at the velocity ratio 0.28 (see fig. 5.19).

Figure 5.17 shows the axial evolution of the concentration half width of fuel and oxidizer as varying the velocity ratio at the same recess ratio of 2.25. As velocity ratio increase, concentration half width of fuel increase due to the swirling momentum of oxidizer. Especially at the velocity ratio 1.23, concentration half width is wider than the oxidizer at the downstream from the nozzle exit (see fig. 5.18). In this region, fuel rich region exist at the outside of the spray and oxidizer rich zone of swirl coaxial becomes very large. Therefore, mixing efficiency decreased as velocity ratio increased at the swirl injector with recess case. But it is less sensitive than injector without recess.

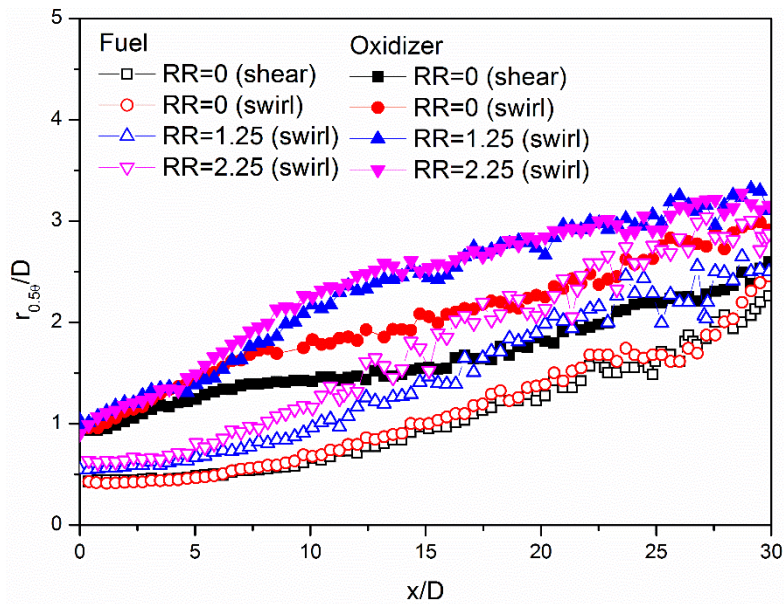


Fig. 5.16 The axial evolution of the concentration half-width as a function of recess ratio ( $U_0/U_i=0.57$ ).

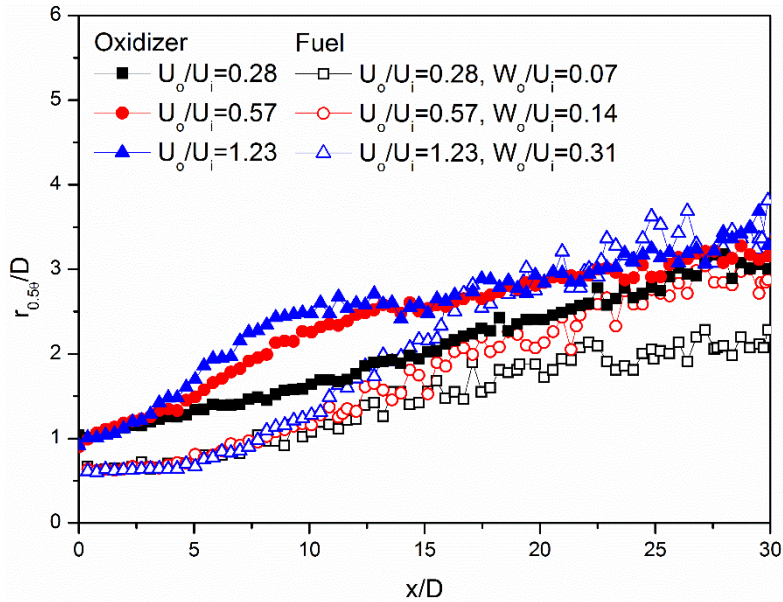


Fig. 5.17 The axial evolution of the concentration half-width as a function of velocity ratio (RR=2.25).

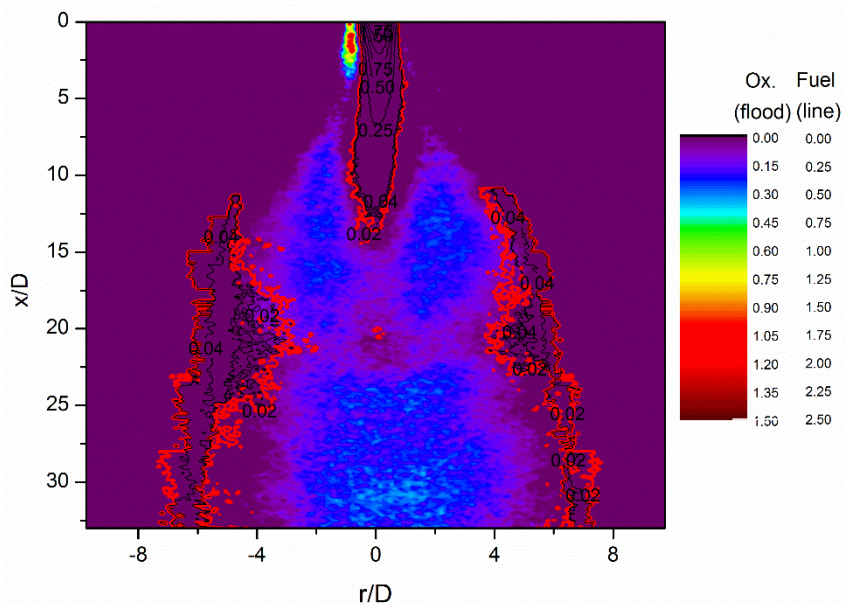


Fig. 5.18 Deviation Index of fuel ( $42.5\mu\text{m}$ ) and oxidizer of swirl coaxial injector at  $U_0/U_i=1.23$  and  $RR=2.25$ ; the line and flood contours indicate the fuel rich and oxidizer rich regions, respectively.

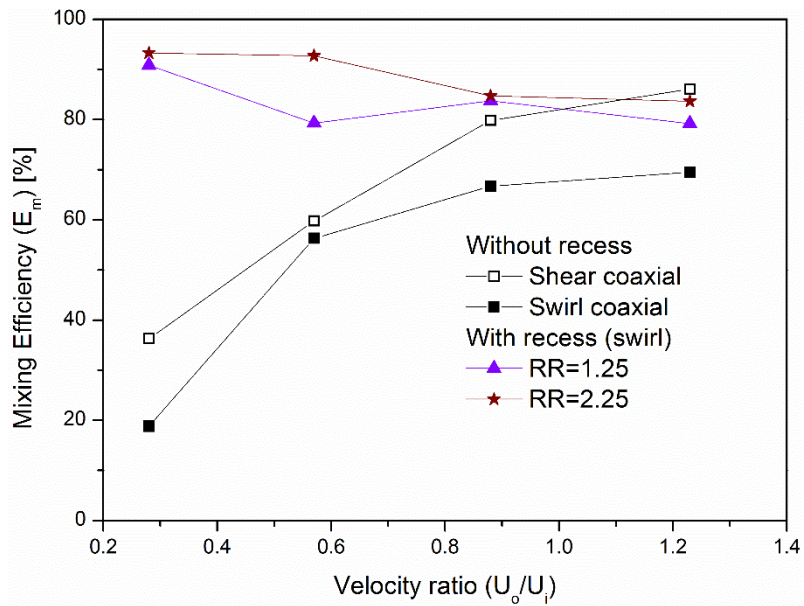


Fig. 5.19 Mixing efficiencies of shear and swirl coaxial injectors as a function of recess ratio ( $x/D=15$ ).

## CHAPTER 6

### CONCLUSION

The effects of gas and liquid Reynolds number on the spray characteristics of the gas-liquid shear coaxial injector with annular liquid were investigated experimentally. Also, the similarity characteristics such as centerline velocity decay, radial velocity profile and particle number density of gas and particle phase in particle-laden simple jet was investigated experimentally. With these basic data, mixing characteristics of particle-laden coaxial injector with coaxial shear and swirl jet was performed. From the experimental results, the following conclusions are obtained.

The self-pulsation characteristics of a gas centered shear coaxial injector were investigated by measuring spray patterns (indirect photography and high speed image), spray oscillation characteristics, and the self-pulsation boundary. When the self-pulsation occurred, strong mass oscillation of spray and severe noise observed and spray angle higher than no pulsation. The reason of spray angle expanded is self-pulsation process based on the liquid bubble rupturing process, when liquid bubble ruptured, gas momentum has as radial direction momentum.

The self-pulsation characteristics frequency was measured according to the liquid and gas Reynolds number and the recess ratio. At low recessed case, self-pulsation frequency increased according to the liquid and gas Reynolds number increases. Furthermore it was decreases with recess ratio increased. However at high recessed case, self-pulsation frequency decreased with liquid Reynolds number increased. Because in high recessed case, self-pulsation occurred with high momentum flux ratio and its characteristic frequency is 0.6~0.8 kHz.

The self-pulsation boundary is obtained according to the liquid, gas momentum flux and recess ratio. The occurrence of self-pulsation phenomenon is determined by taking indirect photography and absorbing laser attenuation signal. At the low recessed case, self-pulsation occurred in low momentum flux ratio ( $J \leq 1.25$ ), the

self-pulsation boundary lines plotted inversely with respect of with or without recess. Because, severe interaction occurred between liquid and gas phase in recessed case. Therefore, the growth of liquid bubble will be limited that is main factor of self-pulsation phenomenon in gas centered shear coaxial injector used in this study. Conversely at the high recessed case, self-pulsation occurred in high momentum flux ratio ( $J \geq 0.5$ ).

An experiment on particle-laden jets was conducted with particle-loading ratio variations at high exit Stokes number condition. The mean velocity and turbulence modulation were measured using the PIV, PTV technique for the gas and particle phases, simultaneously. The experimental results reveal the significant influence of the solid particle loading and exit Stokes number on the flow characteristics. The gas-phase velocity of particle-laden flow in the developing region, which is lower than the single-phase gas velocity and that increases as the loading ratio increases. However in the developed region, two-phase gas velocity is higher than single-phase gas velocity. Similarity hypothesis of velocity applied in gas and particle phase, in gas phase it is agreed with previous results. However, particle phase velocity profile is narrower than gas phase due to the inertia of particles.

The experimental result of this conducted study indicated that in the case of a high Stokes number condition, the turbulence modulation and velocity profiles are affected by the particle-loading ratio with respect to the axial distance from the nozzle exit. Therefore, in the initial jet region, a CGV effect has also been considered; as well, the centerline velocity was expressed as a function of the axial distance ( $x/D$ ), the initial particle-loading ratio ( $\phi_0$ ), and the CGV  $\left(\frac{U_{SP} - U_{TP}}{U_{SP}}\right)$ . Centerline velocity decay coefficient of particles can be expressed by the particle Reynolds number, and virtual origin of centerline velocity decay of particle is relate with the velocity decay coefficient.

In the presents of particles in the fluid, gas phase turbulence has been changed. The turbulence modulation characteristics of a particle laden two-phase focused on gas phase turbulence were investigated by PIV technique. Axial mean slip velocity

and particle volume concentration significantly affected in turbulence modulation. In the case of axial mean slip velocity is almost zero at the  $r/D = 0.4$ , which that region absent of turbulence attenuation effect based on the particle fluctuating drag force (i.e.  $F_{\text{drag}} \propto (U_f - U_s) \times f(v)$ ). Therefore, which region there is no turbulence enhanced nor attenuated. Moreover, the mean velocity difference between the two-phase decreases at the outer jet region, which means fluctuating drag force diminished with increased of particle loading ratio. It is inferred that the CTI was inversely proportional to the particle volume concentration times mean slip velocity. This results expand the criterion of turbulence modulation proposed by Gore and Crowe.

The effect of orifice recess and velocity ratio on the mixing characteristics of particle-gas shear and swirl coaxial injectors were investigated. The mixing characteristics of the shear and swirl coaxial injectors were compared by measuring the concentrations of both fuel and oxidizer using the Mie scattering (for particle distribution) and acetone-PLIF (for gas distribution) technique. The calculation of deviation indices led to the distributions of oxidizer-rich and fuel-rich regions and also to the mixing efficiency at a measurement plane.

In case of shear and swirl coaxial injector without recess, oxidizer-rich regions wider than shear coaxial injector due to the oxidizer width is wider than shear coaxial injector. As for the swirl coaxial injector without recess, swirling momentum does not change significantly the particle distribution due to the inertia of particle. Therefore, the mixing efficiency of shear coaxial was higher than that of swirl coaxial injector at the same conditions.

The effect of recess ratio on mixing efficiencies were obtained. The internal interaction of two propellants led to the increases of the concentration half width of the fuel due to the swirling momentum of oxidizer transported to the fuel, and thus mixing efficiency increased compared to injectors without recess. The mixing efficiency was sensitive to the change of velocity ratio of oxidizer to fuel in both injector without recess. On the other hand, the swirl coaxial injector with recess showed more stable and high mixing efficiency than shear coaxial for the increase

of the velocity ratio. It is thought, therefore, that the swirl coaxial injector with recess is useful for the rocket engine which have wide operating ranges.

## REFERENCES

- AHN, K., KIM, J.-H. & YOON, Y. 2003. Application of PIV to over-expanded supersonic flows: Possibilities and limits. *Journal of visualization*, 6, 353-361.
- AMBROSE, D., SPRAKE, C. & TOWNSEND, R. 1974. Thermodynamic properties of organic oxygen compounds XXXIII. The vapour pressure of acetone. *The Journal of Chemical Thermodynamics*, 6, 693-700.
- BAYVEL, L. 1993. *Liquid atomization*, CRC Press.
- BAZAROV, V. Self-pulsations in coaxial injectors with central swirl liquid stage. AIAA, ASME, SAE, and ASEE, Joint Propulsion Conference and Exhibit, 31 st, San Diego, CA, 1995.
- BAZAROV, V. & LUL'KA, L. 1978. Self-pulsation of liquid flow in coaxial air stream. *Soviet Aeronautics*, 3, 14-18.
- BAZAROV, V. G. & YANG, V. 1998. Liquid-propellant rocket engine injector dynamics. *Journal of Propulsion and Power*, 14, 797-806.
- BIRZER, C. H., KALT, P. A. & NATHAN, G. J. 2012. The influences of particle mass loading on mean and instantaneous particle distributions in precessing jet flows. *International Journal of Multiphase Flow*, 41, 13-22.
- BREVIS, W., NI O, Y. & JIRKA, G. H. 2011. Integrating cross-correlation and relaxation algorithms for particle tracking velocimetry. *Experiments in Fluids*, 50, 135-147.
- CAI, J., DINGER, M., LI, W., CARTER, C., RYAN, M. & TONG, C. 2011. Experimental study of three-scalar mixing in a turbulent coaxial jet. *Journal of Fluid Mechanics*, 685, 495-531.
- CHENG, Y., POTHOS, S. & DIEZ, F. 2010. Phase discrimination method for simultaneous two-phase separation in time-resolved stereo PIV measurements. *Experiments in fluids*, 49, 1375-1391.

- EATON, J. K. & FESSLER, J. R. 1994. Preferential concentration of particles by turbulence. *International journal of multiphase flow*, 3, 1169-1178.
- ELGHOBASHI, S. 1994. On predicting particle-laden turbulent flows. *Applied Scientific Research*, 52, 309-329.
- FARMER, W. 1972. Measurement of particle size, number density, and velocity using a laser interferometer. *Applied Optics*, 11, 2603-2612.
- FESSLER, J. R., KULICK, J. D. & EATON, J. K. 1994. Preferential concentration of heavy particles in a turbulent channel flow. *Physics of Fluids*, 6, 3742-3749.
- FILATYEV, S., THARIYAN, R., LUCHT, R. & GORE, J. Application of Simultaneous Stereo PIV and Double Pulsed Acetone PLIF to Study Turbulent Premixed Flames. 35 th AIAA Aerospace Sciences Meeting & Exhibit, 2007.
- FLECKHAUS, D., HISHIDA, K. & MAEDA, M. 1987. Effect of laden solid particles on the turbulent flow structure of a round free jet. *Experiments in Fluids*, 5, 323-333.
- FOOTE, J. P., LINEBERRY, J. T., THOMPSON, B. R. & WINKELMAN, B. C. Investigation of aluminum particle combustion for underwater propulsion applications. Proceedings of the 32nd AIAA/ASME/SAE/ASEE Joint Propulsion Conference and Exhibit, 1996.
- FOOTE, J. P. & LITCHFORD, R. J. Powdered magnesium-carbon dioxide combustion for mars propulsion. 41st AIAA/ASME/SAE/ASEE Joint Propulsion Conference & Exhibit, 2005. 1-12.
- FOREMAN, R. J. & NATHAN, G. J. 2009. Scaling of the gas phase in particle-laden turbulent axisymmetric jets. *International Journal of Multiphase Flow*, 35, 96-100.
- GHANDHI, J. 2006. Spatial resolution and noise considerations in determining scalar dissipation rate from passive scalar image data. *Experiments in fluids*, 40, 577-588.
- GILLANDT, I., FRITSCHING, U. & BAUCKHAGE, K. 2001. Measurement of

- phase interaction in dispersed gas/particle two-phase flow. *International journal of multiphase flow*, 27, 1313-1332.
- GORE, R. & CROWE, C. 1989. Effect of particle size on modulating turbulent intensity. *International Journal of Multiphase Flow*, 15, 279-285.
- GOROSHIN, S., HIGGINS, A. J. & LEE, J. H. S. 1999. Powdered magnesium-carbon dioxide propulsion concepts for Mars missions. *AIAA Paper 99*, 2408.
- HADINOTO, K. & CURTIS, J. S. 2004. Effect of interstitial fluid on particle-particle interactions in kinetic theory approach of dilute turbulent fluid-particle flow. *Industrial & engineering chemistry research*, 43, 3604-3615.
- HADINOTO, K., JONES, E. N., YURTERI, C. & CURTIS, J. 2005. Reynolds number dependence of gas-phase turbulence in gas-particle flows. *International journal of multiphase flow*, 31, 416-434.
- HARDALUPAS, Y. & HORENDER, S. 2003. Fluctuations of particle concentration in a turbulent two-phase shear layer. *International journal of multiphase flow*, 29, 1645-1667.
- HARDALUPAS, Y., TAYLOR, A. M. K. P. & WHITELAW, J. H. 1989. Velocity and Particle-Flux Characteristics of Turbulent Particle-Laden Jets. *Proceedings of the Royal Society of London. A. Mathematical and Physical Sciences*, 426, 31-78.
- HETSRONI, G. 1989. Particles-turbulence interaction. *International Journal of Multiphase Flow*, 15, 735-746.
- HUSSEIN, H. J., CAPP, S. P. & GEORGE, W. K. 1994. Velocity measurements in a high-Reynolds-number, momentum-conserving, axisymmetric, turbulent jet. *Journal of Fluid Mechanics*, 258, 31-75.
- IM, J.-H., KIM, D., HAN, P., YOON, Y. & BAZAROV, V. 2009. Self-pulsation characteristics of a gas-liquid swirl coaxial injector. *Atomization and Sprays*, 19.
- KENDALL, J. M. 1986. Experiments on annular liquid jet instability and on the formation of liquid shells. *Physics of Fluids (1958-1988)*, 29, 2086-2094.

- KHALITOV, D. A. & LONGMIRE, E. K. 2002. Simultaneous two-phase PIV by two-parameter phase discrimination. *Experiments in fluids*, 32, 252-268.
- KIGER, K. T. & PAN, C. 2000. PIV technique for the simultaneous measurement of dilute two-phase flows. *Journal of fluids engineering*, 122, 811-818.
- KIM, M., OH, J. & YOON, Y. 2011. Flame length scaling in a non-premixed turbulent diluted hydrogen jet with coaxial air. *Fuel*, 90, 2624-2629.
- LAATS, M. 1966. Experimental study of the dynamics of an air-dust jet. *Journal of engineering physics*, 10, 6-8.
- LI, F., QI, H. & YOU, C. 2010. Phase Doppler anemometry measurements and analysis of turbulence modulation in dilute gas–solid two-phase shear flows. *Journal of Fluid Mechanics*, 663, 434-455.
- LI, X. & SHEN, J. 1999. Experimental study of sprays from annular liquid jet breakup. *Journal of propulsion and power*, 15.
- LIU, H., CAO, W., XU, J., LI, W., GUO, X. & SUN, Z. 2012. Characterization of the granular jet in a coaxial gas stream. *Powder Technology*, 225, 206-213.
- LONGMIRE, E. K. & EATON, J. K. 1992. Structure of a particle-laden round jet. *Journal of Fluid Mechanics*, 236, 217-257.
- LOZANO, A. 1992. *Laser-excited luminescent tracers for planar concentration measurements in gaseous jets*. Ph. D. dissertation, Stanford University,.
- LOZANO, A., BARRERAS, F., SIEGLER, C. & L W, D. 2005. The effects of sheet thickness on the oscillation of an air-blasted liquid sheet. *Experiments in fluids*, 39, 127-139.
- LOZANO, A., YIP, B. & HANSON, R. 1992. Acetone: a tracer for concentration measurements in gaseous flows by planar laser-induced fluorescence. *Experiments in Fluids*, 13, 369-376.
- MALMSTR M, T. G., KIRKPATRICK, A. T., CHRISTENSEN, B. & KNAPPMILLER, K. D. 1997. Centreline velocity decay measurements in low-velocity axisymmetric jets. *Journal of Fluid Mechanics*, 346, 363-377.
- MAND , M., LIGHTSTONE, M., ROSENDAHL, L., YIN, C. & S RENSEN, H. 2009. Turbulence modulation in dilute particle-laden flow. *International*

- Journal of Heat and Fluid Flow*, 30, 331-338.
- MELVILLE, W. & BRAY, K. 1979. The two-phase turbulent jet. *International Journal of Heat and Mass Transfer*, 22, 279-287.
- MERGHENI, M. A., SAUTET, J. C., GODARD, G., BEN TICHA, H. & BEN NASRALLAH, S. 2009. Experimental investigation of turbulence modulation in particle-laden coaxial jets by Phase Doppler Anemometry. *Experimental Thermal and Fluid Science*, 33, 517-526.
- MILLER, T. F. & HERR, J. D. Green rocket propulsion by reaction of Al and Mg powders and water. 40th AIAA/ASME/SAE/ASEE Joint Propulsion Conference and Exhibit, 2004. 2004.
- MODARRESS, D., ELGHOBASHI, S. & TAN, H. 1984. Two-component LDA measurement in a two-phase turbulent jet. *AIAA journal*, 22, 624-630.
- PAIK, K.-Y., YOON, J., HWANG, J., CHUNG, J. M., BOUVET, N. & YOON, Y. 2011. Effect of Particle Loading Ratio and Orifice Exit Velocity on a Particle-Laden Jet. *International Journal of Aeronautical and Space Sciences*, 12, 296-304.
- PANCHAPAKESAN, N. R. & LUMLEY, J. L. 1993. Turbulence measurements in axisymmetric jets of air and helium. Part 1. Air jet. *Journal of Fluid Mechanics*, 246, 197-223.
- PANG, B., YU, K. & YOUNG, G. Characterization of Nano-and Micron-Sized Aluminum Particles Burning in Dump Combustor. 47th AIAA Aerospace Sciences Meeting Including the New Horizons Forum and Aerospace Exposition, 2009.
- REHAB, H., VILLERMAUX, E. & HOPFINGER, E. 1997. Flow regimes of large-velocity-ratio coaxial jets. *Journal of Fluid Mechanics*, 345, 357-381.
- RHODES, M. 2008. *Introduction to particle technology*, John Wiley & Sons.
- RITCHIE, B. D. 2006. *Quantitative acetone PLIF measurements of jet mixing with synthetic jet actuators*.
- RUPE, J. H. 1956. A correlation between the dynamic properties of a pair of impinging streams and the uniformity of mixture ratio distribution in the

- resulting spray. *JPL Prog. Rep*, 20-195.
- SHELAR, V. M., HEGDE, G. M., UMESH, G., JAGADEESH, G. & REDDY, K. 2013. Visualization of coherent structures in turbulent subsonic jet using planar laser induced fluorescence of acetone. *Eur. Phys. J. Appl. Phys*, 62, 31102.
- SHEN, J. & LI, X. 1996a. Breakup of annular viscous liquid jets in two gas streams. *Journal of propulsion and power*, 12, 752-759.
- SHEN, J. & LI, X. 1996b. Instability of an annular viscous liquid jet. *Acta Mechanica*, 114, 167-183.
- THURBER, M. C., GRISCH, F., KIRBY, B. J., VOTSMEIER, M. & HANSON, R. K. 1998. Measurements and modeling of acetone laser-induced fluorescence with implications for temperature-imaging diagnostics. *Applied optics*, 37, 4963-4978.
- WAHONO, S., HONNERY, D., SORIA, J. & GHOJEL, J. 2008. High-speed visualisation of primary break-up of an annular liquid sheet. *Experiments in fluids*, 44, 451-459.
- WICKER, R. B. & EATON, J. K. 2001. Structure of a swirling, recirculating coaxial free jet and its effect on particle motion. *International journal of multiphase flow*, 27, 949-970.
- YASUDA, Y. & SOHN, H. 1995. Experimental and theoretical study of particle dispersion phenomena in a turbulent gas jet of the flash-smelting process by the image analysis technique. *Metallurgical and Materials Transactions B*, 26, 637-646.
- ZHANG, W., WANG, Y. & LEE, S. J. 2008. Simultaneous PIV and PTV measurements of wind and sand particle velocities. *Experiments in Fluids*, 45, 241-256.
- ZHOU, J., HU, X., HUANG, Y. & WANG, Z. 1996. Flowrate and Acoustics characteristics of coaxial swirling injector of hydrogen/oxygen rocket engine. *AIAA Paper*, 96-3135.



## 초 록

금속 분말(알루미늄, 마그네슘)을 연료로 사용하는 분사기의 분무 특성에 대한 실험적 연구를 수행하였다. 산화제로 사용될 수 있는 해수가 액체상태로 분사된 경우를 가정하여 기체 중심 기체-액체 전단 동축 분사기에서 분사조건 변화에 따른 분무특성의 변화를 연구하였다. 또 입자 부상제트에서 입자와 이송가스의 상사성에 대한 연구를 수행하였고, 동축 전단 분사기 및 동축 스윙 분사기에서 분말과 동축 가스의 혼합에 대한 연구를 수행하였다.

기체 중심 기체-액체 전단 동축 분사기의 분무특성 및 액막의 분열 과정을 연구하기 위하여 유량 측정, 직접 사진촬영을 이용하였다. 이 분사기에서 self-pulsation 현상이 발생하였으며 이는 분무 진동과 강한 소음을 동반한다. 이러한 self-pulsation 현상은 액체와 기체의 분사 압력과 유동 진동을 발생시킨다. 이러한 진동으로 인해 연소 불안정 현상이 증폭될 수 있으므로 self-pulsation 현상은 제어할 수 있어야 한다. 이러한 self-pulsation 분무의 액막 주파수를 측정하였고 이를 통해 리세스와 액체 및 기체 레이놀즈 수가 self-pulsation에 미치는 영향을 알아 보았다. 그 결과 리세스 수에 따라 self-pulsation 현상이 서로 다르게 나타나는 것을 확인하였다. 낮은 리세스 수에서는 액체의 표면장력에 의한 액체 버블의 붕괴 과정에 의해 섭동이 발생하였고, 높은 리세스 수에서는 분사기 내에서 공기와 액막의 충돌에 의해 섭동이 발생하는 것으로 판단된다.

입자 부상 제트에서 입자에 의한 이송가스 특성의 변화와 입자의 분무특성을 동시 계측하기 위하여  $1\mu\text{m}$ 의 작은 입자(유동특성)와  $42.5\mu\text{m}$ 의 큰 입자(연료)를 동시분사 하였다. 이송가스의 경우 입자 로딩비에 따라 이송가스의 속도 및 난류강도가 달라짐을 확인하였고, 이송가스속도 및 입자속도 모두 상사성을 만족함을 확인하였다. 이송가스의 축 방향 속도

감쇠의 경우 젯의 발달영역과 완전발달 영역에서 입자로딩비의 영향이 서로 다르게 나타남을 확인하였다. 따라서 젯의 발달영역과 완전발달 영역에서 축 방향 속도감쇠에 대한 서로 다른 상사식을 도출하였으며 이를 기존의 결과에도 적용하였다. 입자의 축 방향 속도 감쇠의 경우 입자에 가해지는 항력이 입자 레이놀즈수에 따라 결정되므로 축 방향 속도 감쇠를 입자 레이놀즈수를 통해 스케일링하였다. 이송가스의 난류강도의 경우 기존에는 입자의 크기와 난류길이 척도로 입자에 의한 이송가스의 난류강도 변화를 판단하였으나, 본 실험의 결과는 그에 적용되지 않으므로 입자와 이송가스의 상대속도의 비를 통해 이 상대속도가 증가할수록 난류강도가 증가함을 확인하였고 이를 통해 기존의 척도뿐만 아니라 이송가스와 입자의 상대속도 또한 고려해야 함을 알 수 있었다.

또한, 입자와 동축 가스의 혼합에 대해 연구하기 위하여 Mie 산란기법과 Acetone PLIF 기법을 입자와 동축가스에 각각 적용하였다. 전단 동축 분사기는 리세스가 없는 조건에서 스웰 동축 분사기에 비해 혼합효율이 우수하지만 연료와 산화제의 분사속도 비에 민감하다는 것을 확인하였다. 하지만 스웰 동축형 분사기는 리세스가 있을 경우에 혼합성능이 전단 동축 분사기에 비해 높게 나타나고 속도비에 크게 민감하지 않으므로, 작동범위가 넓은 추진기관에 유리하다는 결론을 얻을 수 있었다.

**중심어:** 리세스, 분무특성, 혼합 특성, 입자부상 제트, PIV/Acetone PLIF,

상사식

**학 번:** 2011-30204